UNIVERSITY OF CALIFORNIA, SAN DIEGO

New Insights into Small-Scale Vertical Distributions of Phytoplankton

A dissertation submitted in partial satisfaction of the
requirements for the degree Doctor of Philosophy

in

Oceanography

by

Jennifer Chan Prairie

Committee in Charge:

Peter J. S. Franks, Chair
Jules S. Jaffe
Michael R. Landry
Andrew Scull
Clinton D. Winant

2011

The Dissertation of Jennifer Chan Prairie is approved, and it is acceptable in quality and form for publication on microfilm and electronically:

_____

_____

_____

_____

_____
Chair

University of California, San Diego

2011

TABLE OF CONTENTS

Signature Page..... iii

Table of Contents..... iv

List of Figures..... vi

List of Tables..... xi

Acknowledgments..... xiii

Vita..... xvii

Abstract of the Dissertation..... xviii

Chapter I. Introduction..... 1
Thesis Overview..... 6
References..... 8

Chapter II. Cryptic peaks: invisible vertical structure in fluorescent particles revealed using a planar laser imaging fluorometer..... 13
Abstract..... 13
Introduction..... 13
Methods..... 14
Results..... 19
Discussion..... 21
Acknowledgements..... 26
References…..... 27

Chapter III. Unexplained variability in the distribution and size spectra of particles in the ocean..... 29
Abstract..... 29
Introduction..... 30
Methods..... 33
Results..... 38
Discussion..... 42
Acknowledgements..... 51
Tables..... 52
Figures..... 56
References…..... 82

Chapter IV. Physical and biological controls of vertical gradients in phytoplankton..... 86

Abstract..... 86
Introduction..... 87
Methods..... 89
The Phytoplankton Gradient Model..... 96
Results..... 98
Discussion..... 101
Acknowledgements..... 110
Table..... 111
Figures..... 112
References..... 123

Chapter V. The transition from individual to continuous scales in ecology:
what is a phytoplankton patch? 128
Abstract..... 128
Introduction..... 129
Methods..... 130
Results and Discussion..... 135
Acknowledgements..... 143
Tables..... 144
Figures..... 150
References..... 157

Chapter VI. Conclusions..... 160
References..... 164

LIST OF FIGURES

Figure 2.1 (A) Picture of the FIDO-Φ on deck of the R/V Wecoma. (B) Schematic of the FIDO-Φ system showing the camera and laser housings and the region where the laser sheet is imaged. The placement of the attached WETStar fluorometer and SCAMP are also shown..... 15

Figure 2.2 (A) Geographical location of the study site in the Santa Barbara Channel. (B) Inset of the study site shown in A with the sampling region indicated by a black dot..... 15

Figure 2.3 (A) Vertical profile of fluorescence from the WETStar fluorometer attached to the FIDO-Φ. (B) Profile of fluorescence obtained by integrating the fluorescence over individual FIDO-Φ images. (C) Fluorescence from the FIDO-Φ vs. fluorescence from the WETStar fluorometer for all 11 drops..... 17

Figure 2.4 (A) An example of an image from the FIDO-Φ showing the distribution of fluorescent particles after the fluorescence threshold was applied. (B) A 600 pixel x 600 pixel inset of the same image. The bottom surface depicts the raw fluorescence. The distribution of particles is shown in the overlayed image.... 17

Figure 2.5 (A) Profiles of particle concentration versus depth calculated using three different fluorescence thresholds from the FIDO-Φ for Drop7-2. (B) Profiles of relative particle concentration shown as a fraction of the maximum particle concentration for the same fluorescence thresholds used in A..... 18

Figure 2.6 Example of ship-deployed SBE 911plus CTD and WETStar fluorometer profile, taken prior to Deployment 3. (A) Profile of density from the ship-deployed SBE 911plus CTD. (B) Profile of fluorescence from the ship-deployed WETStar fluorometer calibrated to chlorophyll samples..... 19

Figure 2.7 Comparison of vertical profiles for Drop 3-1 (top row), Drop 4-1 (middle row), and Drop 7-2 (bottom row). (A) Profiles of bulk fluorescence. (B) Profiles of fluorescent particle concentration. (C) Profiles of water density. (D) Profiles of buoyancy frequency..... 22

Figure 2.8 Comparison of profiles of the ratio of fp1-5:fp>5 with profiles of bulk fluorescence and total fluorescent particle concentration for Drop 4-2 (top row) and Drop 6-1 (bottom row). (A) Ratio of fp1-5:fp>5. (B) Total bulk fluorescence. (C) Total fluorescent particle concentration..... 23

Figure 2.9 (A) Fluorescent particle concentration profiles for Drop 4-1 (left) and Drop 4-2 (right). (B) Fluorescent particle concentration profiles for Drop 7-1 (left) and Drop 7-2 (right). (C) Density profiles for Drop 4-1 and Drop 4-2 (D) Density profiles for Drop 7-1 and Drop 7-2..... 24

Figure 2.10 Schematic of four proposed mechanisms for the offset in depth observed for peaks of high particle concentration found in Drops 4-1 and 4-2..... 24

Figure 3.1 Drop 3-1. Fluorescent (A) and scattering (C) particle size distributions. Size spectral parameters for fluorescent (B) and scattering (D) particles. Density and buoyancy frequency profiles (E). Particle concentration vs. slope and intercept for fluorescent particles (F, G) and scattering particles (H, I)..... 56

Figure 3.2 Drop 3-2. Fluorescent (A) and scattering (C) particle size distributions. Size spectral parameters for fluorescent (B) and scattering (D) particles. Density and buoyancy frequency profiles (E). Particle concentration vs. slope and intercept for fluorescent particles (F, G) and scattering particles (H, I)..... 58

Figure 3.3 Drop 4-1. Fluorescent (A) and scattering (C) particle size distributions. Size spectral parameters for fluorescent (B) and scattering (D) particles. Density and buoyancy frequency profiles (E). Particle concentration vs. slope and intercept for fluorescent particles (F, G) and scattering particles (H, I)..... 60

Figure 3.4 Drop 4-2. Fluorescent (A) and scattering (C) particle size distributions. Size spectral parameters for fluorescent (B) and scattering (D) particles. Density and buoyancy frequency profiles (E). Particle concentration vs. slope and intercept for fluorescent particles (F, G) and scattering particles (H, I)..... 62

Figure 3.5 Drop 5-1. Fluorescent (A) and scattering (C) particle size distributions. Size spectral parameters for fluorescent (B) and scattering (D) particles. Density and buoyancy frequency profiles (E). Particle concentration vs. slope and intercept for fluorescent particles (F, G) and scattering particles (H, I)..... 64

Figure 3.6 Drop 6-1. Fluorescent (A) and scattering (C) particle size distributions. Size spectral parameters for fluorescent (B) and scattering (D) particles. Density and buoyancy frequency profiles (E). Particle concentration vs. slope and intercept for fluorescent particles (F, G) and scattering particles (H, I)..... 66

Figure 3.7 Drop 7-1. Fluorescent (A) and scattering (C) particle size distributions. Size spectral parameters for fluorescent (B) and scattering (D) particles. Density and buoyancy frequency profiles (E). Particle concentration vs. slope and intercept for fluorescent particles (F, G) and scattering particles (H, I)..... 68

Figure 3.8 Drop 7-2. Fluorescent (A) and scattering (C) particle size distributions. Size spectral parameters for fluorescent (B) and scattering (D) particles. Density and buoyancy frequency profiles (E). Particle concentration vs. slope and intercept for fluorescent particles (F, G) and scattering particles (H, I)..... 70

Figure 3.9 Drop 8-2. Fluorescent (A) and scattering (C) particle size distributions. Size spectral parameters for fluorescent (B) and scattering (D) particles. Density and buoyancy frequency profiles (E). Particle concentration vs. slope and intercept for fluorescent particles (F, G) and scattering particles (H, I)..... 72

Figure 3.10 Drop 9-2. Fluorescent (A) and scattering (C) particle size distributions. Size spectral parameters for fluorescent (B) and scattering (D) particles. Density and buoyancy frequency profiles (E). Particle concentration vs. slope and intercept for fluorescent particles (F, G) and scattering particles (H, I)..... 74

Figure 3.11 Drop 9-3. Fluorescent (A) and scattering (C) particle size distributions. Size spectral parameters for fluorescent (B) and scattering (D) particles. Density and buoyancy frequency profiles (E). Particle concentration vs. slope and intercept for fluorescent particles (F, G) and scattering particles (H, I) 76

Figure 3.12 Plot of fluorescent particle concentration anomaly vs. scattering particle concentration anomaly for all drops..... 78

Figure 3.13 Plots of size spectra properties vs. fluorescence and scattering particle concentration for all drops. Fluorescent particle concentration vs. fluorescent particle size spectral slope (A) and intercept (B) Scattering particle concentration vs. scattering particle size spectral slope (C) and intercept (D)..... 79

Figure 3.14 Plots of size spectra properties vs. total bulk fluorescence for all drops of the FIDO-Φ. (A) Log-log plot of total bulk fluorescence vs. slope of the size spectra for scattering particles. (B) Log-log plot of total bulk fluorescence vs. intercept of the size spectra for fluorescent particles..... 80

Figure 3.15 Plot of fluorescent particle spectral slope vs. scattering particle spectral slope for all drops..... 81

Figure 4.1 (A) The FIDO-Φ on deck of the R/V Wecoma. (B) Schematic of the FIDO-Φ system showing the camera and laser housings and the region where the laser sheet is imaged. The placement of the attached WETStar fluorometer and SCAMP are also shown..... 112

Figure 4.2 A photograph of the TurboMAP-L, deployed on the 2006 cruise concurrently with the FIDO-Φ. Data from the TurboMAP-L was used to estimate dissipation rates of turbulent kinetic energy..... 113

Figure 4.3 (A) An example of an image from the FIDO-Φ showing the distribution of fluorescent particles after the fluorescence threshold was applied. (B) A 600 pixel x 600 pixel inset of the same image. The bottom surface depicts the raw fluorescence. The distribution of particles is shown in the overlayed image... 114

Figure 4.4 Steady-state solution of the phytoplankton layer model for three different sets of parameters. The idealized underlying distribution $P^*(z')$ in the absence of mixing is shown in red. The blue, green, and black curves show the steady-state phytoplankton concentration profile, $P(z')$ for various parameter sets..... 115

Figure 4.5 An example of the maximum phytoplankton gradient, SPG_{max}, derived empirically from the model at steady state, plotted vs. η, for d=1.2 m (black line). The red line indicates the line $SPG_{max} = \eta$, and the horizontal dashed black line indicates the line $SPG_{max} = d^{-1}$..... 117

Figure 4.6 Vertical profiles of properties from Drop 7-2. (A) Fluorescent particle concentration. (B) Scaled particle concentration gradient, SP_CG. (C) Buoyancy frequency, N. (D) Diffusivity, K_ρ..... 118

Figure 4.7 (A) Probability density function of all observed scaled particle concentration gradients (SP_CG) from 7 drops of the September 2006 cruise. (B) Probability density function of all observed scaled fluorescence gradients (SFG) from the same data. 119

Figure 4.8 (A) Scaled particle concentration gradient (SP_CG) plotted vs. $K_\rho^{-1/2}$ for all 7 drops of the 2006 cruise. A family of envelopes containing 99% of the data points can be constructed by varying the slope and gradient ceiling. (B) Scaled fluorescence gradient (SFG) plotted vs. $K_\rho^{-1/2}$ for the same data..... 120

Figure 4.9 (A) Probability density function of the individual realized γ values for each value of SP_CG. (B) Probability density function of the individual realized γ values for each value of SP_CG as a fraction of the estimated γ_{max}..... 121

Figure 4.10 From the model solution at steady state, the ratio of the realized layer thickness to d, the idealized layer thickness in the absence of mixing, for given values of $\eta=(\gamma/ K_\rho)^{1/2}$..... 122

Figure 5.1 A schematic showing two different scenarios for the composition of a microscale fluorescence peak: the sample volume may be composed of a higher concentration of the small phytoplankton (B1) or the sample volume may contain a large eukaryotic phytoplankton or aggregate (B2)..... 150

Figure 5.2 (A) The FIDO-Φ on deck of the R/V Wecoma. (B) An example of an image from the FIDO-Φ. The color bar represents chlorophyll *a* fluorescence. The black boxes represent the binning schematic used to create the microscale vertical profiles of chlorophyll *a* fluorescence..... 151

Figure 5.3 Comparison of corresponding profiles of chlorophyll *a* fluorescence from the FIDO-Φ (red line) and the TurboMAP-L (blue line). (A) TurboMAP-L and

FIDO-Φ profiles of fluorescence smoothed to 20 cm. (B) Unsmoothed TurboMAP-L and FIDO-Φ profiles of fluorescence..... 152

Figure 5.4 (A) An example of a microscale profile of fluorescence with peaks numbered. (B) The corresponding image to the microscale fluorescence profile with regions that correspond to peaks boxed in black. (C) Insets of the image shown in B corresponding to three of the microscale peaks..... 153

Figure 5.5 (A) Fraction of microscale fluorescence peaks of a given intensity which contain at least one particle. (B) Average number of particles within peaks of a given intensity. (C) Average area of particles within peaks of a given intensity. (D) Average length of particles within peaks of a given intensity..... 154

Figure 5.6 (A) Average number of particles within microscale fluorescence peaks of a given width. (B) Average area of particles within peaks of a given width. (C) Average length of particles within peaks of a given width..... 155

Figure 5.7 Relationship of sample volume size to the fractional change in fluorescence caused by one large particle. Blue line shows the mean fractional change, red line shows the median fractional change, and the cyan line shows the 95th percentile fractional change at each sample volume respectively……..... 156

LIST OF TABLES

Table 2.1 Description of the times, locations, and number of drops and images for each deployment of the FIDO-Φ on the 2006 cruise..... 16

Table 2.2 Description of the times and locations of each ship-deployed SBE 911plus CTD with attached WETStar fluorometer profile with water samples on the 2006 cruise..... 16

Table 2.3 List of all fluorescent particle concentration peaks identified in each drop. Depth, thickness (defined as the full-width half-peak), density, and buoyancy frequency are described for each peak. Cryptic peaks are indicated by asterisks..... 20

Table 2.4 List of all bulk fluorescence peaks identified in each drop. Depth, thickness (defined as the full-width half-peak), density, and buoyancy frequency are described for each peak. Bulk fluorescence-only peaks are indicated by asterisks..... 21

Table 3.1 Correlation coefficients (r^2) for the least square fit for each drop for both the fluorescent and scattering size spectra. The value given is the mean for each drop with standard deviation in parentheses..... 52

Table 3.2 List of all fluorescent particle concentration peaks identified in each drop. Depth, thickness (defined as the full-width half-peak), density, buoyancy frequency and the mean slope and intercept of the size spectra are described for each peak..... 53

Table 3.3 List of all scattering particle concentration peaks identified in each drop. Depth, thickness (defined as the full-width half-peak), density, buoyancy frequency, and the mean slope and intercept of the size spectra are described for each peak..... 54

Table 3.4 Linear least squares fit line for fluorescent particle concentration vs. scattering particle concentration and corresponding correlation coefficient (r^2) for each drop. Asterisks indicate drops with a significant correlation between fluorescent particle concentration and scattering particle concentration ($p<0.05$)..... 55

Table 4.1 Description of the times, locations, and number of drops and images for each deployment of the FIDO-Φ on the 2006 cruise..... 111

Table 5.1 Description of the microscale fluorescence profiles created from each drop of the FIDO-Φ on the 2006 cruise..... 144

Table 5.2 Average and median number of particles found within all sample bins and within microscale peaks of from each drop of the FIDO-Φ..... 145

Table 5.3 Average and median major axis lengths of particles from each drop of the FIDO-Φ. Lengths are given in pixels, where 1 pixel ~ 90 μm..... 146

Table 5.4 Average and median area of particles from each drop of the FIDO-Φ. Areas are given in pixels^2, where 1 pixel^2 ~8100 μm^2..... 147

Table 5.5 Number of microscale fluorescence peaks and their particle composition categorized by peak intensity among all drops of the FIDO-Φ..... 148

Table 5.6 Number of microscale fluorescence peaks and their particle composition categorized by peak width among all drops of the FIDO-Φ..... 149

ACKNOWLEDGMENTS

I would like to first and foremost thank my advisor Peter Franks. I was so fortunate to have what I can only imagine is the most supportive mentor at Scripps Institution of Oceanography. Peter's scientific and career advice helped me throughout my graduate career, and I am not sure I would have made it through graduate school without his encouragement and guidance.

I want to also thank committee member, coauthor, and cruise companion Jules Jaffe. Jules provided amazing scientific guidance that has greatly improved my thesis and my scientific capacity. He always took the time to brainstorm with me and provide feedback on my work. I also always enjoyed my many off-topic conversations with Jules, especially during our late night shifts in Dabob Bay.

My thesis could also not have been completed without the help of the rest of my wonderful committee – Mike Landry, Clint Winant, and Andy Scull. My committee was always ready with useful feedback. I very much appreciate their responsiveness and scientific insight, in addition to their genuine concern about my future.

To all the members of Peter Frank's lab past and present that I got a chance to know during my time at Scripps, I want to thank you for your support and friendship. I always looked forward to our weekly lab meetings, and it was great to interact with you each about both scientific and non-scientific matters. Additionally, I want to thank Erdem Karaköylü and Drew Lucas for their help before and during my cruise with the auxiliary instrumentation.

I also wanted to thank the many members of Jules' lab without whom my thesis would not have been possible. I particularly want to acknowledge Paul Roberts and Fernando Simonet for their help in designing, building, and deploying the FIDO-Φ, in addition to constantly helping me troubleshoot my data.

I would also like to thank other people who helped during my cruise, notably Emy Daniels and Christian Anderson for the shipboard conductivity-temperature-depth (CTD) deployments and processing chlorophyll samples, Heather McClendon for analyzing samples for species composition, and the crew of the R/V Wecoma.

I would like to thank Hide Yamazaki and Mark Doubell, who were coauthors on two of my dissertation chapters. Hide was very generous in supporting me financially and scientifically during a 2 week research stay in his lab at the Tokyo University of Marine Science and Technology. During my time in Tokyo, I worked very closely with Mark Doubell, who made every effort to collaborate with me, resulting in an amazing scientific partnership. Both Hide and Mark provided excellent feedback as coauthors that substantially improved the two thesis chapters that we collaborated on. I would also like to thank the members of Hide's lab who helped deploy the TurboMAP-L during my cruise in 2006, and whose help in processing the TurboMAP-L data made this collaboration possible.

I would like to deeply thank all my friends at Scripps Institution of Oceanography who helped me along the way – Alison Cawood, Ally Pasulka, Darcy Taniguchi, Jesse Powell, Mike Stukel, Moira Decima, and the countless others who kept me company, proofread my work, and just generally maintained my sanity. Thanks to Geoff Cook for

being the greatest officemate in the world, even when I distracted you from your work. And a special thanks to Fozzy and his extreme fluffiness.

I also would like to mention my friends and family who supported me outside of graduate school life. Thanks to my mom, dad, and two brothers and thanks to my friends from home and college who visited me in San Diego and traveled with me to remote parts of the world for much needed breaks – Jessica Hou, Melissa Sabga, Tienmu Ma, Ingrid Stromberg, and the crew from Dartmouth. A special thanks to my boyfriend Ryan who has been very supportive throughout this whole process, even from across the country.

I would like to acknowledge the many people and organizations during my time at Scripps that had the faith in me to support me financially. I thank the National Science Foundation who supported me for three years as a graduate fellow. I thank the ARCS foundation and everyone who works with this great program to support young scientists. I would also like to thank the Scripps Graduate Office and everyone who works as part of it for both their financial support and immense help in making administrative processes run smoothly. My work was also made possible by the support of several grants that funded both my work and my research: the U.S. Office of Naval Research grant N00014-06-1-0304 and the National Science Foundation grant OCE 08-25154.

Chapter 2, in full, is a reprint of previously published material as it appears in Limnology and Oceanography, 2010, Prairie, J. C., Franks, P. J. S., and Jaffe, J. S. The dissertation author was the primary investigator and author of this paper.

Chapter 3, in part, is currently being prepared for submission for publication of the material. Prairie, J. C., Franks, P. J. S., and Jaffe, J. S. The dissertation author was the primary investigator and author of this paper.

Chapter 4, in full, has been submitted for publication of the material as it may appear in Limnology and Oceanography: Fluids and Environments, 2011, Prairie, J. C., Franks, P. J. S., Jaffe, J. S., Doubell, M. J., and Yamazaki, H. The dissertation author was the primary investigator and author of this paper.

Chapter 5, in part, is currently being prepared for submission for publication of the material. Prairie, J. C., Franks, P. J. S., Jaffe, J. S., Doubell, M. J., and Yamazaki, H. The dissertation author was the primary investigator and author of this paper.

VITA

2004	Bachelor of Arts, Dartmouth College
2005-2008	National Science Foundation Graduate Fellow
2007	Master of Science, University of California, San Diego
2007	Adjunct Lecturer, University of San Diego
2010	Teaching Assistant, University of California, San Diego
2011	Doctor of Philosophy, University of California, San Diego

PUBLICATIONS

Prairie, J. C., P. J. S. Franks, and J. S. Jaffe. 2010. Cryptic peaks: invisible vertical structure in fluorescent particles revealed using a planar laser imaging fluorometer. Limnology and Oceanography 55: 1943-1958.

Prairie, J. C., P. J. S. Franks, J. S. Jaffe, M. J. Doubell, and H. Yamazaki. *in press*. Physical and biological controls of vertical gradients in phytoplankton (*Limnology and Oceanography: Fluids and Environments*)

Prairie, J. C., P. J. S. Franks, J. S. Jaffe, M. J. Doubell, and H. Yamazaki. *in prep*. The transition from individual to continuous scales in ecology: what is a phytoplankton patch? (for *Science*)

Prairie, J. C., P. J. S. Franks, and J. S. Jaffe. *in prep*. Comparing the vertical distribution and size spectra of fluorescent particles to all particles. (for *Journal of Plankton Research*)

ABSTRACT OF THE DISSERTATION

New Insights into Small-Scale Vertical Distributions of Phytoplankton

by

Jennifer Chan Prairie

Doctor of Philosophy in Oceanography

University of California, San Diego, 2011

Professor Peter J. S. Franks, Chair

Phytoplankton are the building blocks of marine pelagic food webs, fixing carbon through photosynthesis and providing food to higher trophic levels. Thus, how phytoplankton are distributed spatially can significantly affect important ecological processes such as carbon cycling and trophic dynamics. In this dissertation, I present analyses of vertical phytoplankton distributions on scales of a meter and less using data from a novel free-falling planar laser imaging fluorometer, the FIDO-Φ. I frequently observed peaks in fluorescent particle concentration with no coincident peaks in bulk fluorescence. These cryptic peaks may be regions of local importance for zooplankton foraging and aggregate formation, and are undetectable using methods that only measure

bulk fluorescence. Small-scale variability was also observed in particle size spectra and the distribution of total particles throughout the water column. However, changes in these variables did not explain much of the observed structure in fluorescent particle concentration. This result suggests that small-scale phytoplankton distributions are likely controlled by complex interactions between different factors, and cannot be predicted accurately from simple correlations. To resolve these interactions, I developed a model that describes the control of gradients in phytoplankton abundance by biological and physical dynamics. The model predicted that the maximum strength of phytoplankton gradients is determined by a balance between turbulent mixing and the rate of phytoplankton layer formation. Comparing these results with phytoplankton gradient data and simultaneous physical measurements allowed estimation of the rate of layer formation and the minimum possible phytoplankton layer thickness. This understanding of the mechanisms underlying phytoplankton layer formation will allow better prediction of small-scale phytoplankton distributions. Analyzing images from the FIDO-Φ also allowed the investigation of the spatial distributions of phytoplankton on centimeter scales. The data revealed that individual large phytoplankton or fluorescent aggregates can cause microscale peaks in chlorophyll *a* fluorescence. The investigation of small-scale vertical phytoplankton distributions presented in this dissertation provides knowledge of local phytoplankton variability – the backdrop upon which fundamental ecological processes take place.

CHAPTER I.

INTRODUCTION

The study of the ocean on scales of a meter and less is intrinsically important to understanding plankton ecology, since these are the scales at which individual organisms live, move, and perceive their environment. Our knowledge of phytoplankton on these scales has long been hindered by limitations in instrumentation. However, classical work on phytoplankton distributions in the ocean has laid the groundwork for recent research on small-scale plankton dynamics. The early paradigm that the ocean is biologically uniform has been replaced with the understanding that the biological community can exhibit significant spatial structure on very small scales (Denman and Gargett, 1995). Early literature concluded that plankton is most commonly over-dispersed in the ocean, that is, it shows a tendency toward clumping and aggregations (Cassie, 1963). Vertical patchiness of plankton populations in the water column has long been recognized. This spatial structure has been observed on a broad range of scales and in many forms, including layers and gradients (Derenbach et al., 1979; Mitchell and Fuhrman 1989; Owen 1989).

With recent advances in technology, we are beginning to achieve accurate measurements of both fine-scale (meter) and micro-scale (centimeter) distributions of phytoplankton (Holliday et al., 2003). Frequent observations of intense thin layers of chlorophyll *a* or optical properties have shown that phytoplankton distributions can often demonstrate persistent vertical heterogeneity on the scale of meters (e.g., Cowles et al. 1998; Dekshenieks et al. 2001; McManus et al. 2003; Ryan et al. 2008; Sullivan et al.

2010). These layers can be formed by many different biological and physical mechanisms (Derenbach et al. 1979; Franks et al. 1995; Cheriton et al. 2009; Durham et al. 2009; Ryan et al. 2010) and their composition may often differ markedly from that of the water column as a whole (Rines et al. 2002; Prairie et al. 2010). Understanding the nature of these fine-scale features is fundamental to plankton ecology, since many ecological processes such as zooplankton foraging and aggregate formation may take place at disproportionately high rates in these regions (Alldredge et al. 2002; McManus et al. 2003; Prairie et al. 2010).

Recent work has tried to elucidate implications of small-scale phytoplankton structure on trophic dynamics and carbon flux by comparing the vertical distribution of phytoplankton to that of other ecologically important types of particles, such as zooplankton or aggregates. Using a combination of traditional sampling, acoustics, and optical imaging, higher zooplankton biomass has often been observed associated with regions of increased concentrations of phytoplankton or chlorophyll *a* (Holliday et al. 2003; McManus et al. 2003; Menden-Deuer 2008; Benoit-Bird et al. 2009). In addition, zooplankton grazing rates have been shown to be enhanced within phytoplankton layers (Menden-Deuer and Fredrickson 2010). These observations support laboratory findings demonstrating that certain zooplankton can seek out and remain in regions of high prey concentration (Tiselius 1992; Menden-Deuer and Grünbaum 2006). In addition, recent advances in in-situ video imaging have allowed the observation of heterogeneous vertical distributions of marine snow aggregates (Jackson et al. 1997; Gorsky et al. 2000; Checkley et al. 2008; Picheral et al. 2010). Since increased phytoplankton concentrations

may lead to increased rates of aggregate formation (Jackson 1990; Kiørboe 1997), it is essential to link these vertical distributions of aggregates to phytoplankton layers.

Others have attempted to learn more about phytoplankton thin layers by analyzing the composition of the phytoplankton assemblage in relation to changes in its vertical distribution. For example, Rines et al. (2002) observed that phytoplankton layers often have very different taxonomic compositions than the water column as a whole. However, one of the most instructive approaches to investigate changes in the phytoplankton community is by exploring variations in its size structure (Sheldon 1972), since phytoplankton size distributions can affect phytoplankton population dynamics and particle sinking rates (Shanks and Trent 1980; Zhou and Huntley 1997; McDonnell and Buesseler 2010). Exploring phytoplankton size structure may be especially important since it has been shown to vary significantly spatially (Barnes et al. 2011), even vertically over small-scales (Ruiz et al. 1996; Franks and Jaffe 2008).

Understanding the basic dynamics of vertical phytoplankton distributions requires knowledge of the mechanisms that act to control them. Many studies have proposed plausible mechanisms for phytoplankton layer formation (Derenbach et al., 1979; Franks, 1995; Young et al., 2001; Durham et al. 2009), but in the field it has been difficult to definitively characterize the operating mechanisms for specific phytoplankton layers (Sullivan et al. 2005; Ryan et al. 2008; Cheriton et al. 2009; Steinbuck et al. 2009). Recent insight into the biological and physical dynamics influencing small-scale phytoplankton distributions has been provided by the development of models of phytoplankton layer formation and maintenance (Stacey et al. 2007; Birch et al. 2008; Birch et al. 2009). From further theoretical work coupled with multidisciplinary field

studies, we may be able to elucidate what factors control phytoplankton layer formation, allowing us to better predict the occurrence of these ecologically important features. Models may also reveal information on the temporal and spatial scales of phytoplankton patches, providing an improved understanding of their importance for ecological processes such as trophic dynamics and carbon cycling.

Important technological developments have led to a recent surge of investigations on the micro-scale distribution of phytoplankton. Many studies have deployed high-resolution fluorometers, discovering layers and gradients as thin as a centimeter or less (Desiderio et al., 1993; Doubell et al., 2006; Yamazaki et al. 2006; Doubell et al. 2009). Others have used syringe-sampling devices and have found structure and clustering on centimeter scales (Mitchell and Fuhrman, 1989; Bjornsen and Nielsen, 1991; Waters et al., 2003). The inhomogeneities found in these studies seem to contradict some of the most recent work on phytoplankton distributions using imaging technology. Malkiel et al., (2006) used holography to view the 3D distributions of particles, and found no significant differences in the nearest-neighbor distances of dinoflagellates and randomly distributed particles. Franks and Jaffe (2001) presented the initial analysis of images from a planar laser imaging fluorometer, suggesting that fluorescent particles were distributed randomly on centimeter scales. These discrepancies in recent findings may result from the different methods in which these studies have explored microscale phytoplankton distributions. While studies which used imaging devices have analyzed the spatial distribution of individual particles, the studies which used fluorometers or water samples analyzed structure in chlorophyll *a* or fluorescence, bulk measurements which are proxies for phytoplankton biomass. At scales less than a centimeter, large individual

phytoplankton or fluorescent aggregates may obstruct the interpretation of bulk chlorophyll *a* or fluorescence data. Thus, it is not clear whether observed peaks in chlorophyll *a* or fluorescence are due to changes in phytoplankton concentration or variations in the size of phytoplankton cells in a small sample volume (Desiderio et al., 1993). Unraveling these methodological issues is essential to resolving phytoplankton distributions at these scales.

Knowledge of small-scale vertical phytoplankton distributions and the dynamics that control them is fundamental to many aspects of plankton ecology, since local changes in phytoplankton concentrations can affect small-scale plankton dynamics, with implications for large-scale ecosystem processes. Regions of increased phytoplankton concentration can result in increased zooplankton abundances and grazing rates, as shown theoretically, in laboratory experiments, and in the field (Davis et al. 1991; Tiselius 1992; Leising and Franks 2000; Menden-Deuer and Grünbaum 2006; Menden-Deuer and Fredrickson 2010). In addition, rates of aggregate formation and consequently carbon flux will be enhanced in phytoplankton layers (Jackson 1990; Kiørboe 1997). Recent studies have also shown that bacteria may be able to chemotactically locate and settle large phytoplankton and marine snow aggregates; thus microscale changes in phytoplankton biomass may affect local nutrient cycling (Mitchell et al. 1985; Azam and Long 2001; Kiørboe and Jackson 2001). All of these studies have demonstrated that previous estimates of ecological processes, which are averaged over the depth of the water column, may be missing important small-scale variability that occurs at the scale of the individual. Despite the importance of these small-scale variations, we are only beginning to understand small-scale phytoplankton distributions in the ocean. In this

dissertation, I use novel field data and theory to explore small-scale vertical phytoplankton dynamics, and their implications for large-scale phenomena.

Thesis Overview

To determine the vertical distribution of phytoplankton over a range of small-scales, I have used data from a planar laser imaging fluorometer, the FIDO-Φ, which was deployed in the Santa Barbara Channel in 2006. Using the FIDO-Φ to study phytoplankton distributions has an important advantage over other methods – the ability to obtain simultaneous vertical profiles of both bulk fluorescence and fluorescent particle concentration. By comparing these profiles, I observed cryptic peaks in fluorescent particle concentration with no concurrent peaks in bulk fluorescence (Chapter 2). These peaks represent small-scale structure in specific groups of phytoplankton that may have important implications for ecological processes. However, these peaks would be invisible using other sampling methods.

The version of the FIDO-Φ used during the 2006 cruise also allowed the comparison of the vertical distribution of fluorescent particles to that of particles as a whole in the water column (Chapter 3). Through this analysis, I observed that small-scale structure in phytoplankton distributions often was reflected in the distribution of other particles; however, at times the distribution of these two types of particles varied independently. I also identified dramatic fluctuations in the size structure of both fluorescent and total particles. These variations indicate that not only total phytoplankton abundance, but also phytoplankton community composition can change vertically over small scales.

Combining a mathematical model with phytoplankton concentration data from the FIDO-Φ, I presented an explanation for how biological and physical factors control vertical phytoplankton distributions (Chapter 4). My model predicts that gradients in phytoplankton abundance should be controlled by a balance of mixing and the rate of phytoplankton layer formation. A comparison of the model results to phytoplankton gradient data showed a strong fit, and allowed estimation of the rate of layer formation and the minimum phytoplankton layer thickness, quantities that would be difficult or impossible to measure in situ.

Finally, I analyzed phytoplankton distributions within individual FIDO-Φ images to investigate the role of individual phytoplankton in affecting perceived patterns of phytoplankton patchiness (Chapter 5). Results showed that large individual fluorescent particles can artificially cause peaks in microscale profiles of bulk fluorescence. The composition of these microscale peaks has important implications for phytoplankton interactions with bacteria, predators, and each other. By demonstrating how the scale of observation affects the interpretation of phytoplankton distribution patterns, I provided a framework for future advances in understanding microscale plankton dynamics in situ.

References

Alldredge, A. L., T. J. Cowles, S. MacIntyre, J. E. B. Rines, P. L. Donaghay, C. F. Greenlaw, D. V. Holliday, M. M. Dekshenieks, J. M. Sullivan, J. R. V. Zaneveld. 2002. Occurrence and mechanisms of formation of a dramatic thin layer of marine snow in a shallow Pacific fjord. Marine Ecology Progress Series **233**: 1-12.

Azam, F., and R. A. Long. 2001. Oceanography-Sea snow microcosms. Nature **414**: 495-498.

Barnes, C., X. Irigoien, J. A. A. De Oliveira, D. Maxwell, and S. Jennings. 2010. Predicting marine phytoplankton community size structure from empirical relationships with remotely sensed variables. Journal of Plankton Research **33**: 13-24.

Benoit-Bird, K. J., T. J. Cowles, and C. E. Wingard. 2009. Edge gradients provide evidence of ecological interactions in planktonic thin layers. Limnology and Oceanography **54**: 1382-1392.

Birch, D. A., W. R. Young, and P. J. S. Franks. 2008. Thin layers of plankton: Formation by shear and death by diffusion. Deep-Sea Research Part I **55**: 277-295.

Birch, D. A., W. R. Young, and P. J. S. Franks. 2009. Plankton layer profiles as determined by shearing, sinking and swimming. Limnology and Oceanography **54:** 397-399.

Bjornsen, P. K., and T. G. Nielsen. 1991. Decimeter scale heterogeneity in the plankton during a pycnocline bloom of *Gyrodinium aureolum*. Marine Ecology Progress Series **73**: 263-267.

Cassie, R.M. 1963. Microdistribution of plankton. Oceanogr. Mar. Biol. Ann. Rev. **1**: 223-252.

Checkley, D. M., R. E. Davis, A. W. Herman, G. A. Jackson, B. Beanlands, and L. A. Regier. 2008. Assessing plankton and other particles in situ with the SOLOPC. Limnology and Oceanography **53**: 2123-2136.

Cheriton, O. M., M. A. McManus, M. T. Stacey, and J. V. Steinbuck. 2009. Physical and biological controls on the maintenance and dissipation of a thin phytoplankton layer. Marine Ecology Progress Series **378**: 55-69.

Cowles, T. J., R. A. Desiderio, and M. Carr. 1998. Small-scale planktonic structure: persistence and trophic consequences. Oceanography **11**:4-9.

Davis, C. S., G. R. Flierl, P. H. Wiebe, and P. J. S. Franks. 1991. Micropatchiness, turbulence, and recruitment in plankton. Journal of Marine Research **49**: 109-151.

Dekshenieks, M. M., P. L. Donaghay, J. M. Sullivan, J. E. B. Rines, T. R. Osborn, and M. S. Twardowski. 2001. Temporal and spatial occurrence of thin phytoplankton layers in relation to physical processes. Marine Ecology Progress Series **223**: 61-71.

Denman, K.L. and A.E. Gargett. 1995. Biological-physical interactions in the upper ocean: the role of vertical and small scale transport processes. Annu. Rev. Fluid Mech. **27**: 225-255.

Derenbach, J. B., H. Astheimer, H. P. Hansen, and H. Leach. 1979. Vertical microscale distribution of phytoplankton in relation to the thermocline. Marine Ecology Progress Series **1**: 187-193.

Desiderio, R. A., T. J. Cowles, and J. N. Moum. 1993. Microstructure profiles of laser-induced chlorophyll fluorescence spectra: evaluation of backscatter and forward-scatter fiber-optic sensors. Journal of Atmospheric and Oceanic Technology **10**: 209-224.

Doubell, M. J., L. Seuront, J. R. Seymour, N. L Patten, and J. G. Mitchell. 2006. High-resolution fluorometer for mapping microscale phytoplankton distributions. Applied and Environmental Microbiology **72**: 4475-4478.

Doubell, M. J., H. Yamazaki, H. Li, and Y. Kokubu. 2009. An advanced laser-based fluorescence microstructure profiler (TurboMAP-L) for measuring bio-physical coupling in aquatic systems. Journal of Plankton Research, doi: 10.1093/plankt/fbp092

Durham, W. M., J. O. Kessler, and R. Stocker. 2009. Disruption of vertical motility by shear triggers formation of thin phytoplankton layers. Science **323**: 1067-1070.

Franks, P. J. S. 1995. Thin layers of phytoplankton: a model of formation by near-inertial wave shear. Deep-Sea Research I **42**: 75-91.

Franks, P. J. S. and J. S. Jaffe. 2001. Microscale distributions of phytoplankton: initial results from a two-dimensional imaging fluorometer, OSST. Marine Ecology Progress Series **220**: 59-72.

Franks, P. J. S., and J. S. Jaffe. 2008. Microscale variability in the distributions of large fluorescent particles observed *in situ* with a planar laser imaging fluorometer. Journal of Marine Systems **69**: 254-270, doi:10.1016/j.jmarsys.2006.03.027.

Gorsky, G., M. Picheral, and L. Stemmann. 2000. Use of the underwater video profiler for the study of aggregate dynamics in the North Mediterranean. Estuarine, Coastal and Shelf Science **50**: 121-128.

Holliday, D. V., P. L. Donaghay, C. F. Greenlaw, D. E. McGehee, M. A. McManus, J. M. Sullivan, and J. L. Miksis. 2003. Advances in defining fine- and micro-scale pattern in marine plankton. Aquatic Living Resources **16**: 131-136.

Jackson, G. A. 1990. A model of the formation of marine algal flocs by physical coagulation processes. Deep-Sea Research **37**: 1197-1211.

Jackson, G. A., R. Maffione, D. K. Costello, A. L. Alldredge, B. E. Logan, and H. G. Dam. 1997. Particle size spectra between 1 μm and 1 cm at Monterey Bay determined using multiple instruments. Deep-Sea Research I **44**: 1739-1767.

Kiørboe, T. 1997. Small-scale turbulence, marine snow formation, and planktivorous feeding. Scientia Marina **61**: 141-158.

Kiørboe, T., and G. A. Jackson. 2001. Marine snow, organic solute plumes, and optimal sensory behavior of bacteria. Limnology and Oceanography **46**: 1309-1318.

Leising, A. W., and P. J. S. Franks. 2000. Copepod vertical distribution within a spatially variable food source: a simple foraging-strategy model. Journal of Plankton Research **22**: 999-1024.

Malkiel, E., J. N. Abras, E. A. Widder, and J. Katz. 2006. On the spatial distribution and nearest neighbor distance between particles in the water column determined from in situ holographic measurements. Journal of Plankton Research 28: 149-170.

McDonnell, A. M. P., and K. O. Buesseler. 2010. Variability in the average sinking velocity of marine particles. Limnology and Oceanography **55**: 2085-2096.

McManus, M. A., A. L. Alldredge, A. H. Barnard, E. Boss, J. F. Case, T. J. Cowles, P. L. Donaghay, L. B. Eisner, D. J. Gifford, C. F. Greenlaw, C. M. Herren, D. V. Holliday, D. Johnson, S. MacIntyre, D. M. McGehee, T. R. Osborn, M. J. Perry, R. E. Pieper, J. E. B. Rines, D. C. Smith, J. M. Sullivan, M. K. Talbot, M. S. Twardowski, A. Weidemann, and J. R. Zaneveld. 2003. Characteristics, distribution and persistence of thin layers over a 48 hour period. Marine Ecology Progress Series **261**: 1-19.

Menden-Deuer, S. 2008. Spatial and temporal characteristics of plankton-rich layers in a shallow, temperate fjord. Marine Ecology Progress Series **355**: 21-30.

Menden-Deuer, S. and D. Grünbaum. 2006. Individual foraging behaviors and population distributions of a planktonic predator aggregating to planktonic thin layers. Limnology and Oceanography **51**: 109-116.

Menden-Deuer, S. and K. Fredrickson. 2010. Structure-dependent, protistan grazing and its implication for the formation, maintenance and decline of phytoplankton patches. Marine Ecology Progress Series **420**: 57-71.

Mitchell, J. G., A. Okubo, and J. A. Fuhrman. 1985. Microzones surrounding phytoplankton form the basis for a stratified marine microbial ecosystem. Nature 316: 58-59.

Mitchell, J. G. and J. A. Fuhrman. 1989. Centimeter scale vertical heterogeneity in bacteria and chlorophyll *a*. Marine Ecology Progress Series **54** : 141-148.

Owen, R.W. 1989. Microscale and finescale variations of small plankton in coastal and pelagic environments. Journal of Marine Research **47**: 197-240.

Picheral, M., L. Guidi, L. Stemmann, D. M. Karl, G. Iddaoud, and G. Gorsky. 2010. The Underwater Vision Profiler 5: an advanced instrument for high spatial resolution studies of particle size spectra and zooplankton. Limnology and Oceanography: Methods **8**: 462-473.

Rines, J. E. B., P. L. Donaghay, M. M. Dekshenieks, J. M. Sullivan, and M. S. Twardowski. 2002. Thin layers and camouflage: hidden *Pseudo-nitzschia* spp. (Bacillariophyceae) populations in a fjord in the San Juan Islands, Washington, USA. Marine Ecology Progress Series **225**: 123-137.

Ruiz, J., C. M. García, and J. Rodríguez. 1996. Vertical patterns of phytoplankton size distribution in the Cantabric and Balearic Seas. Journal of Marine Systems **9**: 269-282.

Ryan, J. P., M. A. McManus, J. D. Paduan, and F. P. Chavez. 2008. Phytoplankton thin layers caused by shear in frontal zones of a coastal upwelling system. Marine Ecology Progress Series **354**: 21-34.

Ryan, J. P., M. A. McManus, and J. M. Sullivan. 2010. Interacting physical, chemical and biological forcing of phytoplankton thin-layer variability in Monterey Bay, California. Continental Shelf Research **30**: 7-16.

Shanks, A. L., and J. D. Trent. 1980. Marine snow: sinking rates and potential role in vertical flux. Deep-Sea Research **27A**: 137-143.

Sheldon, R. W., A. Prakash, and W. H. Sutcliffe, Jr. 1972. The size distribution of particles in the ocean. Limnology and Oceanography **17**: 327-340.

Stacey, M. T., M. A. McManus, and J. V. Steinbuck. 2007. Convergences and divergences and thin layer formation and maintenance. Limnology and Oceanography **52**: 1523-1532.

Sullivan, J. M., P. L. Donaghay, and J. E. B. Rines. 2010. Coastal thin layer dynamics: consequences to biology and optics. Continental Shelf Research **30**: 50-65.

Tiselius, P. 1992. Behavior of *Acartia tonsa* in patchy food environments. Limnology and Oceanography **37**: 1640-1651.

Waters, R. L., J. G. Mitchell, and J. Seymour. 2003. Geostatistical characterisation of centimetre-scale spatial structure of *in vivo* fluorescence. Marine Ecology Progress Series **251**: 49-58.

Yamazaki, H., J. G. Mitchell, L. Seuront, F. Wolk, and H. Li. 2006. Phytoplankton microstructure in fully developed oceanic turbulence. Geophysical Research Letters **33**: L01603, doi:10.1029/2005GL024103.

Young, W. R., A. J. Roberts, and G. Stuhne. 2001. Reproductive pair correlations and the clustering of organisms. Nature **412**: 328-331.

Zhou, M., and M. E. Huntley. 1997. Population dynamics theory of plankton based on biomass spectra. Marine Ecology Progress Series **159**: 61-73.

Limnol. Oceanogr., 55(5), 2010, 1943–1958

doi:10.4319/lo.2010.55.5.1943

Cryptic peaks: Invisible vertical structure in fluorescent particles revealed using a planar laser imaging fluorometer

Jennifer C. Prairie,* Peter J. S. Franks, and Jules S. Jaffe

Scripps Institution of Oceanography, University of California San Diego, La Jolla, California

Abstract

Small-scale vertical structure in the distribution of phytoplankton could be fundamentally important for zooplankton foraging, trophic coupling, and carbon cycling in planktonic ecosystems. Here, we identify regions of structure in phytoplankton communities that would be undetected by fluorometers by comparing the vertical distribution of chlorophyll fluorescence to the concentration of fluorescent particles over submeter scales. Images acquired with a free-falling planar laser fluorescence imaging system were used to calculate vertical profiles of the concentrations and spatial distributions of fluorescent particles (e.g., eukaryotic phytoplankton, aggregates) and bulk fluorescence. We frequently observed peaks in the concentration of fluorescent particles with no coincident peak in bulk fluorescence: we define these features as *cryptic peaks*. These cryptic peaks can occur because the integrated fluorescence of the particles that are resolved by the imaging system is a small fraction of the total fluorescence; thus, a dramatic local change in the abundance of fluorescent particles can occur without significantly changing the bulk fluorescence. We also observed *bulk fluorescence–only peaks*: peaks in bulk fluorescence with no coincident peak in fluorescent particle concentration. These features suggest that peaks in bulk fluorescence or chlorophyll *a* do not necessarily indicate increases in the concentration of the fluorescent particles resolved by our system, again emphasizing the difference between these two measures of phytoplankton structure. Comparing the relative abundances of two size classes of the fluorescent particles in the images revealed that the size composition of the fluorescent particles also varied over small scales. Phytoplankton less than ~ 500 μm in length numerically dominated the composition of most (65%) of the cryptic peaks we observed. By comparing vertical profiles of fluorescent particle concentration from two drops separated by less than an hour, we hypothesize that the peaks formed through vertical shearing of existing patches. Cryptic peaks contained almost 20% of the total number of fluorescent particles counted in all drops during our study and thus could represent disproportionately intense regions for important ecological processes relative to the rest of the water column.

Small-scale vertical structure in the distribution of phytoplankton has the potential to have profound implications for zooplankton foraging, trophic coupling, and carbon cycling in planktonic ecosystems. The distribution of phytoplankton has been studied with both measures of fluorescence or chlorophyll *a* (Chl *a*) and measures of phytoplankton concentration (e.g., cell counts). However, whether these measures of bulk fluorescence and phytoplankton concentration co-vary in the ocean remains an important question in plankton ecology. For example, regions of high phytoplankton concentration but no change in bulk fluorescence could represent sites of enhanced zooplankton grazing undetectable by fluorometers.

Numerous studies have explored heterogeneity in the distributions of fluorescence and Chl *a* in the field. Several studies with high-resolution fluorometers revealed small-scale layers and gradients in bulk Chl *a* fluorescence (Desiderio et al. 1993; Doubell et al. 2006; Yamazaki et al. 2006). Thin layers of enhanced chlorophyll concentration have recently been observed with the use of optical measures of absorption and have indicated the prevalence and importance of these features in coastal waters (Cowles et al. 1998; McManus et al. 2003, 2008). Advances in optical sensors have allowed the estimation of characteristics of phytoplankton within these layers (Holliday et al. 2003). Sullivan et al. (2005) observed substantial fine-scale variability in the scattering properties of particles in Monterey Bay, California, inferring vertical structure in planktonic community composition. Others have used syringe-sampling devices to quantify structure in extracted chlorophyll on centimeter scales (Mitchell and Fuhrman 1989; Waters et al. 2003). All of these studies have used high-resolution optical sensors or syringe-sampling devices to measure Chl *a* fluorescence or extracted chlorophyll to describe structure in the phytoplankton community.

Other studies have analyzed the distribution of phytoplankton by measuring in situ cell concentrations rather than Chl *a* fluorescence or extracted Chl *a*. The video plankton recorder (VPR) has been used to determine the distributions of groups of plankton over scales from microns to hundreds of meters (Davis et al. 1992, 1996). Katz et al. (1999) developed a submersible holographic camera that was used to measure the distributions and characteristics of particles as small as 10 μm in a sample volume of 500–2000 mL. This holographic imaging system was deployed by Malkiel et al. (2006) to measure the local concentrations of several particle types in 500-mL volumes throughout the euphotic zone. Their analyses showed that the smallest particles were randomly distributed within the sample volumes, although larger particles (e.g., detritus) often had clustered distributions.

Several studies have investigated the distribution of bulk fluorescence or extracted chlorophyll and phytoplankton concentration simultaneously. Bjornsen and Nielsen (1991)

* Corresponding author: jprairie@ucsd.edu

observed sharp gradients in Chl *a* using a multisampler with 15-cm resolution. Microscopy revealed that the phytoplankton patches were dominated by the dinoflagellate *Gyrodinium aureolum*. Norrbin et al. (1996) made transects with the VPR over Georges Bank, North America. Chl *a* fluorescence and other environmental variables were measured simultaneously, allowing comparison of the distribution of large diatoms and Chl *a* fluorescence. In one tow, large colonies of *Chaetoceros socialis* were found to coincide with the region of high Chl *a* fluorescence; however, the opposite was observed in another tow, implying that smaller phytoplankton could have dominated in this second region. Rines et al. (2002) studied thin layers of *Pseudo-nitzschia* in a fjord in the San Juan Islands, Washington. The locations of the thin layers were identified using absorption and attenuation meters (WET Labs), and samples were characterized via microscopy to determine the taxonomic composition of the layers. The study provided a qualitative comparison of fluorescence with the concentration of specific phytoplankton groups. The present study complements the results of these studies by comparing the vertical distribution of chlorophyll fluorescence and phytoplankton concentrations over submeter scales, and identifying regions in which they do not co-vary.

Here, we used a fluorescence imaging system, the free-fall imaging device for observing phytoplankton (FIDO-Φ; Jaffe et al. 1998; Franks and Jaffe 2008), to quantify fluorescent particle concentrations and spatial distributions through the euphotic zone. Because the system provides two-dimensional (2D) images of fluorescent particles, we are able to calculate the concentrations and spatial distributions of fluorescent particles (eukaryotic phytoplankton, aggregates, etc.) while also simultaneously measuring bulk fluorescence with the FIDO-Φ. Our analysis of data gathered off the coast of Southern California compares profiles of bulk Chl *a* fluorescence with profiles of the concentration of fluorescent particles. Peaks of increased concentration of fluorescent particles with no concomitant change in the bulk fluorescence were frequently observed and defined as *cryptic peaks*. In addition, we observed *bulk fluorescence–only peaks*—that is, peaks in bulk fluorescence with no coincident peak in fluorescent particle concentration. By dividing the fluorescent particles into two size categories, we inferred how the relative abundances of these two size classes changed with depth. We found that phytoplankton less than ~ 500 μm in length numerically dominated the composition of most (59%) of the cryptic peaks we observed. Finally, by comparing the fluorescent particle concentrations from two vertical profiles separated by less than an hour, we propose several possible mechanisms for the formation of fluorescent particle concentration peaks in these drops.

Methods

Description of the instrument package—The FIDO-Φ is a planar laser imaging fluorometer system that images individual fluorescent particles (Fig. 1A; Jaffe et al. 1998; Franks and Jaffe 2001, 2008). The version of the instrument described here takes high-resolution images of the spatial distribution of fluorescent particles. This FIDO-Φ model had similar specifications to the version of the instrument described in Franks and Jaffe (2008), and much of the description of the current model is taken from this source. The major components of the system included an aluminum frame, a main computer controller, a laser and camera each encased in pressure housings, two pistons for active ballasting, a wireless access point with antenna, and a set of batteries. Tank tests have shown that the descent of the FIDO-Φ through the water column does not disturb the region imaged by the camera at the decent velocities used in these studies.

The laser and camera were mounted on opposite sides of the frame and were angled downward at 45°. The 3-W, 532-nm diode-pumped solid-state laser (CVI Melles Griot) emitted a sheet of light 6.5 mm thick that fanned out at an angle of 15°. A sensitive charge-coupled device (CCD) camera (Cooke Sensicam) imaged the laser sheet at a 90° angle, with the center of the image plane 60 cm below the bottom of the frame (Fig. 1B). The dimensions of this imaged region were ~ 9.8 cm × 13 cm × 0.65 cm. The camera was equipped with a 50-mm Nikor lens with the aperture set to f/1.4. The distance from the lens to the image plane was approximately 100 cm. Interposed between the lens and the camera was a filter, which transmitted light at a wavelength range of 670–690 nm (Chl *a* fluorescence). Images of fluorescent particles were taken at a rate of 2 Hz. Exposure time was 20 ms.

The images from the FIDO-Φ had a field of view of ~ 9.8 cm × 13 cm with a resolution slightly less than 100 μm pixel^{-1}. Laboratory tests with the marine dinoflagellate *Lingulodinium polyedrum* have shown that the camera system was capable of detecting the fluorescence of individual, healthy *L. polyedrum* cells in addition to other phytoplankton as small as 20 μm (Zawada 2002). Moreover, these laboratory experiments demonstrated that the sensitivity of the system was governed by the in vivo chlorophyll fluorescence efficiency of individual phytoplankton cells, and not by a minimum bulk concentration of chlorophyll.

Description of the 2006 cruise—The FIDO-Φ was deployed during a cruise on the R/V *Wecoma* from 31 August 2006 to 07 September 2006 in the Santa Barbara Channel (SBC) off the coast of Southern California (Fig. 2). All deployments were done at night to avoid the confounding signal of solar-stimulated fluorescence during daylight. The FIDO-Φ was configured with a WETStar fluorometer (WET Labs), sampling at 0.5 Hz and mounted 8 cm below the pressure sensor of the FIDO-Φ. Additionally, a self-contained autonomous microstructure profiler (SCAMP, Precision Measurement Engineering) was mounted with the probes 48 cm below the depth sensor of the FIDO-Φ. The SCAMP measured temperature, conductivity, and pressure at 100 Hz. The data of the different instruments and the FIDO-Φ were merged together on the basis of depth, after the depth offsets were applied.

Seven deployments of the FIDO-Φ resulted in the successful acquisition of fluorescent images (Table 1). Each

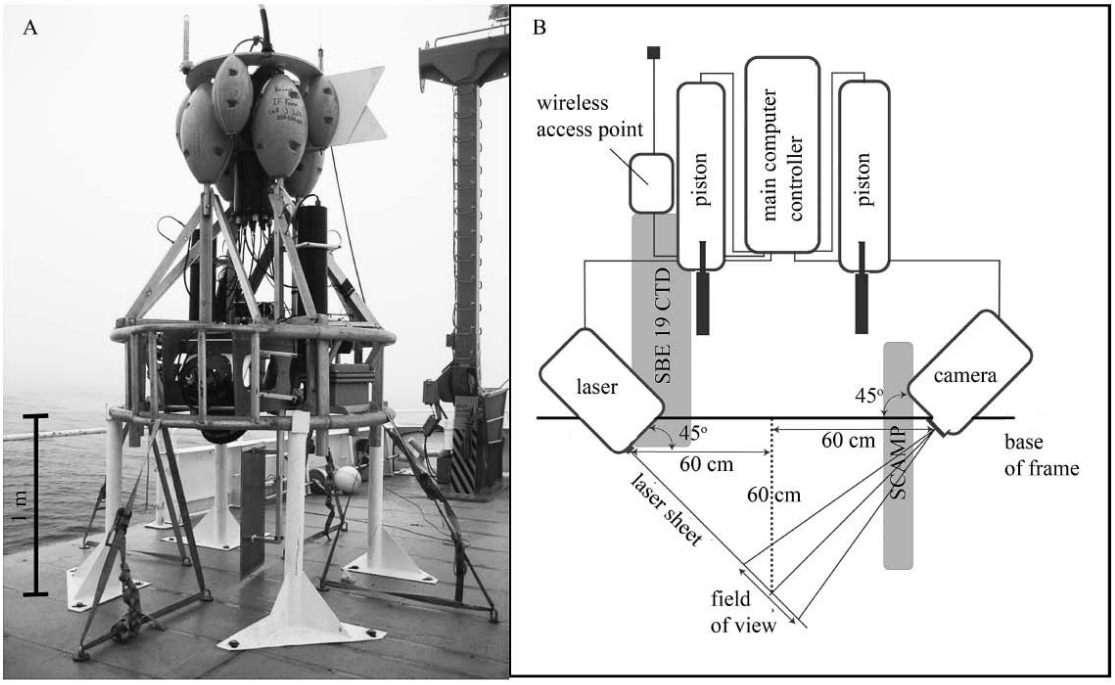

Fig. 1. (A) Picture of the FIDO-Φ on deck of the R/V *Wecoma*. (B) Schematic of the FIDO-Φ system showing the camera and laser housings and the region where the laser sheet is imaged. The placement of the attached WETStar fluorometer and SCAMP are also shown.

deployment consisted of one or two drops, and images were acquired during the vehicle's descent. Concurrent WETStar and SCAMP data were collected for each drop. The descent rate of the instrument package varied among drops but, in general, ranged between 3 and 12 cm s^{-1} and was relatively constant within a drop. This resulted in as much as an 80% vertical overlap of the images in the slowest drops, and a separation of a few centimeters between images in the fastest drops.

Profiles were also made with the ship-deployed Sea-Bird Electronics (SBE) 911plus conductivity-temperature-depth

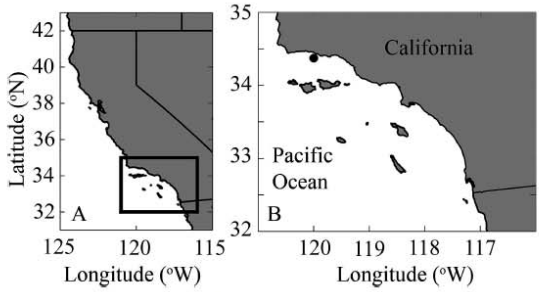

Fig. 2. (A) Geographical location of the study site in the Santa Barbara Channel. (B) Inset of the study site shown in A with the sampling region indicated by a black dot.

(CTD) system (equipped with a rosette with 10-L Niskin bottles and a WET Labs WETStar fluorometer) before or after each of the FIDO-Φ deployments to acquire Chl *a* samples to calibrate the fluorescence profiles of the FIDO-Φ and the WETStar fluorometer attached to the FIDO-Φ (Table 2). Bottles were triggered during the ascent of the CTD in roughly regularly spaced intervals in the top 50 m, with particular emphasis in the top 15 m and within fluorescent features. Analysis of the water samples included measuring size-fractionated Chl *a* concentrations by filtering 250 mL of seawater onto GF/F, 5 μm, 10 μm, and 20 μm filters. Filters were extracted in acetone for 24 h and analyzed with a Turner Designs fluorometer (model 10-AU-005-CE). Samples for species composition analysis were acquired by filtering 1 L of water through a 20-μm mesh and backwashing the sample into vials with buffered formalin. Samples were later settled in Utermöhl chambers, and species composition was quantified by microscopy. We quantified species composition by number, counting entire diatom chains as single individuals to be consistent with how they would be categorized in FIDO-Φ images.

Description of the study site—Our study site in the SBC was bounded by the California coast to the north and by the Channel Islands to the south (Fig. 2). The channel has a generally east–west orientation and is ~ 100 km long and ~ 40 km wide, with a maximum depth of about 500 m (Harms

Table 1. Description of the times, locations, and number of drops and images for each deployment of the FIDO-Φ on the 2006 cruise. The time of drop is listed in Pacific Daylight Time (PDT) as the time of acquisition of the first image.

Deployment	Date of deployment	Location of deployment	Drops and number of images	Time of drop (h PDT)	Duration of drop (min)
3	01 Sep 06	34°24.163 N, 120°1.780 W	Drop 3_1: 2349 images	20:09	15
			Drop 3_2: 1844 images	20:38	14
4	01 Sep 06	34°23.077 N, 120°3.175 W	Drop 4_1: 2521 images	23:05	19
			Drop 4_2: 10808 images	23:39	53
5	02 Sep 06	34°20.995 N, 120°0.001 W	Drop 5_1: 2024 images	19:08	6
6	02 Sep 06	34°20.316 N, 119°56.422 W	Drop 6_1: 1604 images	23:13	15
7	03 Sep 06	34°22.976 N, 120°0.007 W	Drop 7_1: 2786 images	19:06	20
			Drop 7_2: 9250 images	19:53	42
8	04 Sep 06	34°23.013 N, 120°0.011 W	Drop 8_2: 2068 images	00:40	15
9	04 Sep 06	34°23.140 N, 120°0.039 W	Drop 9_2: 1685 images	06:45	15
			Drop 9_3: 2892 images	07:07	21

and Winant 1998). The winds in this channel are generally weak and highly variable (Winant and Dorman 1997; Harms and Winant 1998).

Meteorological data were recorded from the National Data Buoy Center at Station 46053, located at 34°15′N and 119°50′W. During the study period, the mean wind speed was 7.0 m s^{-1} in the direction WSW. Current velocity was measured in 20-m bins with the 150-kHz narrowband acoustic Doppler current profiler (Teledyne RD Instruments) on board the R/V *Wecoma*. The average current velocity in the upper 60 m throughout our study period was calculated to be 0.12 m s^{-1} WNW. The average shear value in the top 50 m was 0.0034 s^{-1} and at times exceeded 0.01 s^{-1}.

Internal waves are common in the SBC and dominated by those of diurnal period. Diurnal-period internal wave amplitudes have been shown to be strongly correlated with stratification and are generally greatest during the summer, when vertical temperature differences can exceed 8°C over a distance of 11 m (Cudaback and McPhee-Shaw 2009).

Image processing and beam correction—The raw 1040 × 1376-pixel images from the FIDO-Φ were processed with MATLAB. The spreading of the laser sheet produces a drop in intensity toward the edges, creating systematic variations of fluorescence signal strength in the images that were corrected before analysis (Zawada 2002). This bias was quantified by averaging all of the fluorescent images from each drop to create a reference, then median filtering this reference to create the beam pattern correction image. All images were then divided by this beam pattern correction image to remove the bias (Franks and Jaffe 2001, 2008). The resultant images show relative fluorescence, necessarily independent of the incident illumination.

For each drop, profiles of bulk fluorescence were obtained concurrently by two independent methods: from the WETStar fluorometer attached to the FIDO-Φ and by integrating the total fluorescence signal for each FIDO-Φ image. The fluorescence profiles from both the WETStar fluorometer and the FIDO-Φ were binned over 30 cm and smoothed with the use of a LOWESS (locally weighted smoothing scatter) method over 1.5 m to remove ephemeral small-scale variability. This smoothing did not remove peaks less than 1.5 m but rather attenuated the fluorescence signal of one- or two-point peaks. Both fluorescence profiles were then calibrated to the Chl *a* samples taken before or after the FIDO-Φ deployment using a linear correction that minimized the root mean square error between the Chl *a* samples and the fluorescence profile data from the same depths. Only drops that had a strong agreement (defined as a root mean square error less than 15% of the maximum fluorescence value) between the WETStar fluorometer and the calibrated FIDO-Φ fluorescence profiles were used in these analyses (Fig. 3). This resulted in a total of 11 drops being used for this study (Table 1). For comparison with the profiles of fluorescent

Table 2. Description of the times and locations of each ship-deployed SBE 911plus CTD with attached WETStar fluorometer profile with water samples on the 2006 cruise.

CTD profile	Time of profile (h PDT)	Location of profile
Before deployment 3	01 Sep 06 18:30	34°24.026 N, 120°3 W
After deployment 3	01 Sep 06 22:08	34°24.308 N, 120°3.202 W
After deployment 4	02 Sep 06 01:10	34°21.602 N, 120°4.754 W
Before deployment 5	02 Sep 06 18:09	34°20.94 N, 120°0 W
Before deployment 6	02 Sep 06 22:00	34°23.009 N, 120°0.051 W
Before deployment 7	03 Sep 06 18:00	34°22.936 N, 119°59.986 W
Before deployment 8	03 Sep 06 23:03	34°23.016 N, 120°0.048 W
Before deployment 9	04 Sep 06 05:03	34°22.934 N, 120°0.023 W
After deployment 9	04 Sep 06 08:15	34°23.018 N, 120°0.030 W

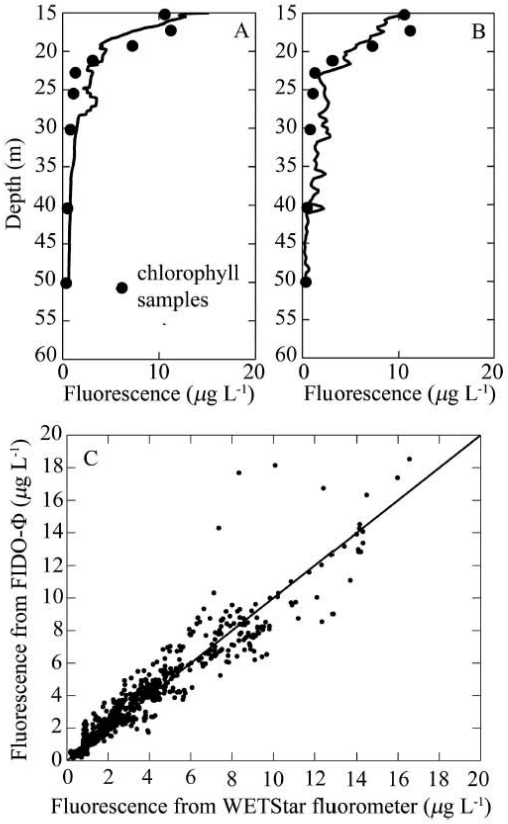

Fig. 3. (A) Vertical profile of fluorescence from the WET-Star fluorometer attached to the FIDO-Φ during drop 3-1. The fluorescence profile was standardized to chlorophyll samples taken ~ 1 h before the FIDO-Φ deployment (chlorophyll samples shown as dots). (B) Profile of fluorescence obtained by integrating the fluorescence over individual FIDO-Φ images from drop 3-1, then binning and smoothing the profile. The profile was standardized to chlorophyll samples as in A. (C) Fluorescence from the FIDO-Φ vs. fluorescence from the WETStar fluorometer for all 11 drops used in the analyses. Solid line shows the 1 : 1 relationship. Linear regression analysis gives the least squares fit line $y = 1.003x + 0.072$ ($r^2 = 0.976$).

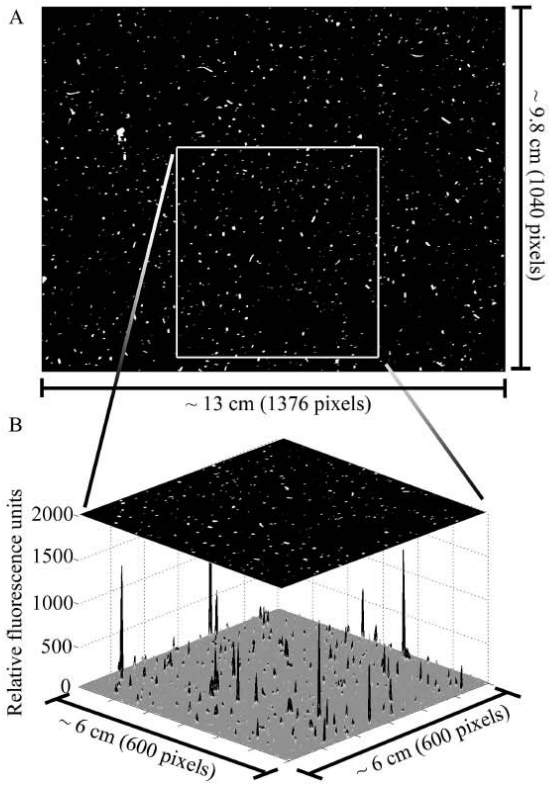

Fig. 4. (A) An example of an image from the FIDO-Φ showing the distribution of fluorescent particles after the fluorescence threshold was applied. (B) A 600 × 600 pixel inset of the same image. The bottom surface depicts the fluorescence values for the image inset. Any peaks that exceeded the fluorescence threshold (the threshold was 85 relative fluorescence units for this drop) are colored black and are defined as particles. The resulting distribution of particles can be seen in the overlaid image inset.

particle concentration, the profiles of bulk fluorescence were also obtained from the FIDO-Φ. For the remainder of the manuscript, unless specifically stated, "bulk fluorescence" refers to fluorescence derived from the FIDO-Φ by integrating the fluorescence over an image. Bulk fluorescence profiles were formed from these images as described previously.

"Fluorescent particles" were defined as pixels or groups of pixels with a fluorescence intensity above a threshold in an image (Fig. 4). This fluorescence threshold was used operationally to separate the fluorescent particles from the background fluorescence. The background fluorescence is caused by other fluorescent objects (e.g., picophytoplankton) much smaller than the camera's resolution. The fluorescence intensity of the fluorescent particles was typically many times higher than the background fluorescence (Fig. 4). Fluorescent particles were labeled by the MATLAB function *bwlabel* with 8-pixel connectivity, and their properties were assessed by the function *regionprops*.

Implementation of the fluorescence threshold resulted in exclusion of the smaller, less intensely fluorescent particles from our particle counts. Thus, only the largest, most fluorescent particles (large eukaryotic phytoplankton, chains, and fluorescent aggregates) were included in our profiles of particle concentration (e.g., Fig. 4). Although it is possible to estimate the size of particles greater than 1 pixel in length, it is not possible to determine the size of particles that only occupy 1 pixel in our images because we know from laboratory tests that fluorescent particles much smaller than the image resolution (~ 100 μm) can be detected by the camera. Thus, we cannot definitively determine the minimum size of the particles we count in

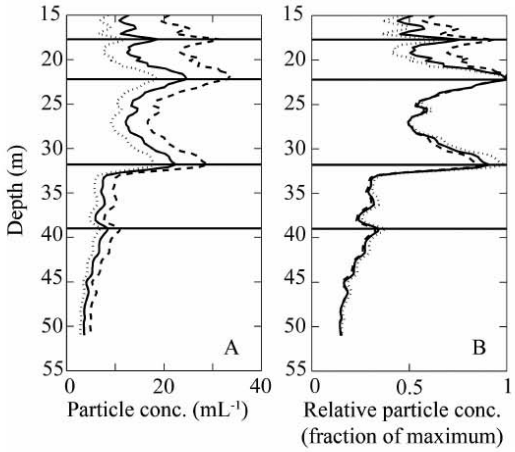

Fig. 5. (A) Profiles of particle concentration vs. depth calculated with the use of three different fluorescence thresholds from the FIDO-Φ for drop 7-2. The solid black line represents the actual threshold used for this drop (~ 3 standard deviations above the mean fluorescence value). The dashed line represents the actual threshold decreased by 10% (~ 2 standard deviations above the mean fluorescence value). The dotted line represents the actual threshold increased by 10% (~ 4 standard deviations above the mean fluorescence value). The solid horizontal lines indicate the locations of peaks in particle concentration as identified with the actual threshold used. (B) Profiles of relative particle concentration shown as a fraction of the maximum particle concentration for the same drop and same fluorescence thresholds used in part A.

our images. However, from instrument specifications and laboratory experiments (Zawada 2002), we can constrain this value between about 20 and 100 μm. Hereafter, this minimum detectable size of particles in our images will be referred to as 1 pixel.

The fluorescence threshold, determined empirically for each drop, was set at least 2 standard deviations above the mean fluorescence value in an image. Although the threshold varied from drop to drop, it was kept constant within a drop to ensure accurate relative particle abundances throughout the water column. Sensitivity tests conducted by varying the threshold between 2 and 4 standard deviations above the mean fluorescence value demonstrated that the shape of the particle concentration profiles did not change (although the magnitude did), as long as the threshold was set above the minimum noise level of ~ 2 standard deviations above the mean fluorescence value (Fig. 5).

The fluorescent particles counted in our images include individual phytoplankters and chains, as well as aggregates including phytoplankton. For the sake of brevity, we will refer to all of the fluorescent objects as "particles." The fluorescence of the particles counted in our images—that is, those particles above the fluorescence threshold—accounted for 4.4–18.4% (average 10.4%) of the bulk fluorescence signal in our images averaged through entire drops.

Profiles of particle concentration vs. depth were constructed from the number of particles per image divided by the volume of the imaged region. These profiles were binned to 30 cm and then smoothed by the locally weighted scatterplot smoothing (LOWESS) method over 1.5 m, in the same manner as the profiles of bulk fluorescence. As with the fluorescence profiles, this smoothing method did not remove peaks thinner than 1.5 m but, rather, attenuated the particle concentration signal of one- or two-point peaks. The binning and smoothing of our profiles makes our identification and quantification of peak magnitudes in the fluorescence and particle concentration profiles conservative.

Definition of particle size classes—We examined the characteristics of the particles counted in the images and, on the basis of the length of their major axes, we divided the particles into two size classes: fluorescent particles between 1 pixel and 5 pixels in length (fp1-5) and fluorescent particles > 5 pixels in length (fp>5). The fp1-5 particles range in length from ~ 20–100 μm to 500 μm. Likewise, the fp>5 particles correspond to particles with lengths greater than ~ 500 μm. These two size classes categorize only the fluorescent particles counted in our images; thus, small fluorescent particles excluded during the thresholding process of our image analyses are not included in these size classes. Although the composition of these size categories cannot be exactly determined by length alone, this method can provide a coarse separation into functional groups. From microscopic examination, particles in the fp1-5 size class consisted largely of large eukaryotic phytoplankton, with a dominance of long diatom chains. Particles in the fp>5 size class included large fluorescent aggregates.

Vertical profiles of the concentration of fp1-5 and fp>5 particles were created and binned and smoothed in the same way as the profiles of total particle concentration. Finally, profiles of both the fp1-5 : fp>5 and the fp>5 : fp1-5 ratios were calculated from these particle size-class profiles. Other methods of categorizing particles, including by particle area and particle shape, were also analyzed and yielded similar results.

Identification of peaks—Peaks were identified in the vertical profiles of both FIDO-Φ bulk fluorescence and particle concentration using the operational definition of local maxima with at least a 50% increase over the local background signal, measured as the nearest minima above and below the peak. This criterion identified significant peaks over the background while eliminating ephemeral features. No minimum or maximum thicknesses were used as criteria in this definition. Other variations of this algorithm to identify peaks gave similar results. This definition of peaks differs from the definition of thin layers used in many studies, in that thin layers must persist over time and space, and layer vertical thickness must be below some maximum (Dekshenieks et al. 2001; Ryan et al. 2008; Cheriton et al. 2009). Because we cannot verify the horizontal and temporal extent of the peaks in this study except in two deployments (*see* Discussion), we refrain from referring to peaks as "layers" throughout this manuscript.

A peak in particle concentration without a coincident peak in bulk fluorescence was defined as a *cryptic peak*. Similarly, a peak in bulk fluorescence without a coincident peak in particle concentration was defined as a *bulk fluorescence–only peak*.

Peaks were also defined for profiles of fp1-5, fp>5, fp1-5 : fp>5, and fp>5 : fp1-5 in the same manner as local maxima with at least a 50% increase over the local background signal, measured as the nearest minima above and below the peak.

Peak properties—The depth of a peak was defined as the location of the maximum in peak intensity. The thickness of the peak was defined as the full-width half-maximum (FWHM) as described in Sullivan et al. (2010). The FWHM is the width of the peak measured as the sum of the distances from the depth of the peak maximum to the depths above and below the peak at which the intensity was half the peak intensity above the background. The background was defined as the average of the minima surrounding the peak.

We used density profiles obtained from the SCAMP attached to the FIDO-Φ. The density profiles from the SCAMP were binned to 1 cm and smoothed over 30 cm. The density profile near the surface was extremely noisy because of the semi-Lagrangian nature of the FIDO-Φ, so the top 10 to 20 m of the profiles (varying among drops) were not used in the analyses. By removing these top portions of the FIDO-Φ fluorescence and particle concentration profiles, we were unable to count peaks in this region of the water column; thus, our analyses likely underestimate the number of peaks in the euphotic zone. The water density at a peak was defined as the density at the peak maximum. The buoyancy frequency, N, is defined as

$$N = \sqrt{-\frac{g}{\rho}\frac{d\rho}{dz}} \tag{1}$$

where g is the acceleration due to gravity, ρ is density, and z is depth. N was calculated from the smoothed SCAMP density data by calculating the change in depth necessary to yield density intervals of $\Delta\rho = 0.005$ kg m^{-3}, as outlined in Duda and Rehmann (2002). This method is numerically stable because it avoids N values of 0 s^{-1}. Buoyancy frequency profiles were then linearly interpolated to obtain the buoyancy frequency of the peaks defined at the peak maximum.

Comparison of particle concentration profiles for subsequent drops—For deployments with multiple drops in succession (deployments 4 and 7), profiles of particle concentration from each drop were plotted vs. both depth and density and compared with cross-correlation for lags from 0.3 m (the minimum resolution of the particle concentration profiles) to 7.5 m in both directions for depth, and from 0.01 kg m^{-3} (the minimum resolution of the density profiles) to 0.10 kg m^{-3} for density. Cross-correlations were performed with the *xcorr* function in MATLAB. This function calculates the cross-correlation C of two profiles x and y as

$$C(x,y) = \sum_{n=0}^{N_{xy}-m-1} x_{n-m}y_n \tag{2}$$

where N_{xy} is the length of x and y (the longer of the two profiles was first shortened to make them the same length), and m is the index of the lag for the given cross-correlation. Cross-correlation values were then normalized such that the auto-correlations at zero lag had a value of 1.0. The intent of the lagged correlations was to reveal whether peaks in one profile were found at different depths or densities in subsequent profiles.

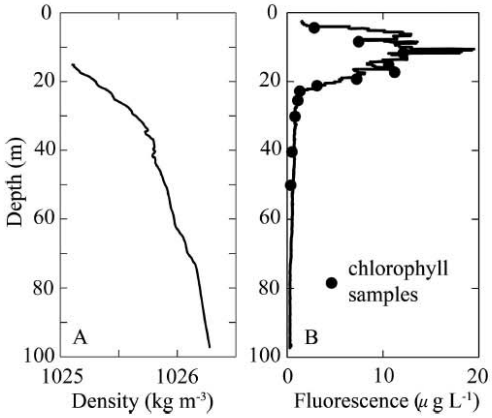

Fig. 6. Example of ship-deployed SBE 911plus CTD and WETStar fluorometer profile, taken before deployment 3. (A) Profile of density from the ship-deployed SBE 911plus CTD. (B) Profile of fluorescence from the ship-deployed WETStar fluorometer calibrated to chlorophyll samples, shown as black dots.

Results

For the duration of the study, density profiles from the ship-deployed SBE 911plus CTD revealed no well-defined pycnocline, but rather a more gradual, often step-like, increase in density through the top 20–80 m of the water column. The ship-deployed WETStar fluorometer profiles and water samples showed that subsurface maxima in both fluorescence and extracted Chl *a* concentration were present at the study site (e.g., Fig. 6). The subsurface Chl *a* maximum was located on average at 8.9 m (ranging from 2.1 m to 17.6 m among the drops). The subsurface fluorescence maximum was located on average at 12.8 m (ranging from 4.9 m to 22.2 m among the drops).

In total, 23 plankton samples collected from bottles on the ship-deployed SBE 911plus CTD during profiles were analyzed for species presence or absence and relative abundance. These samples span all SBE 911plus CTD profiles and depths ranging from 1.4 m to 50 m. This analysis revealed that ~ 95% of phytoplankton > 20 μm were diatom chains, with the remaining ~ 5% comprising dinoflagellates. The most dominant chain-forming diatoms

Table 3. List of all fluorescent particle concentration peaks identified in each drop. Depth, thickness (defined as the full-width half-peak), density, and buoyancy frequency are given for each peak. Cryptic peaks (i.e., fluorescent particle concentration peaks with no coincident peaks in bulk fluorescence) are indicated by asterisks.

Fluorescent particle concentration peaks	Depth (m)	Thickness (m)	Density (kg m^{-3})	Buoyancy frequency (s^{-1})
Drop 3-1				
A*	18.9	3.49	1025.152	0.0137
B	30.0	1.60	1025.318	0.0285
Drop 3-2				
A*	15.6	4.54	1025.120	0.0179
Drop 4-1				
A*	22.2	1.60	1025.370	0.0200
B*	27.6	4.75	1025.492	0.0149
Drop 4-2				
A*	27.3	1.79	1025.499	0.0161
B*	45.3	2.46	1025.727	0.0113
C*	52.8	2.22	1025.856	0.0130
Drop5-1				
A*	29.1	2.36	1025.199	0.0076
Drop 6-1				
A*	19.5	4.99	1025.118	0.0055
B*	33.3	4.26	1025.274	0.0172
Drop 7-1				
A*	17.7	0.71	1025.092	0.0389
B*	22.2	2.47	1025.125	0.0068
C*	31.8	3.01	1025.257	0.0206
D*	39.0	2.26	1025.441	0.0110
Drop 7-2				
A	21	1.45	1025.107	0.0109
B*	38.4	1.47	1025.483	0.0268
Drop 8-2				
No peaks				
Drop 9-2				
No peaks				
Drop 9-3				
A*	20.1	2.99	1025.482	0.0094
B*	34.5	4.71	1025.598	0.0051

were from the genera *Pseudo-nitzschia*, *Chaetoceros*, *Thalassiosira*, and *Nitzschia*; these taxa differed in relative abundances among drops. Dinoflagellates, when present, were most often from the genus *Protoperidinium*.

Fluorescent particle concentration and bulk fluorescence peaks—In total, we identified 19 peaks in fluorescent particle concentration and 18 peaks in bulk fluorescence. Peaks in particle concentration were located on average at depths of 28.8 m, and had an average thickness of 2.80 m. The majority of peaks in particle concentration (74%) were located in regions of buoyancy frequency $> 0.01\ s^{-1}$, even though these regions represented only about half (55%) of the water column. A Monte Carlo test ($n = 19$) showed that the percentage of particle concentration peaks in these high-buoyancy frequency regions was significantly higher than the water column as a whole ($p = 0.069$), with $p < 0.10$ determining significance. Regions with a buoyancy frequency $> 0.01\ s^{-1}$ correspond to stable parts of the water column when the vertical shear values are $< 0.02\ s^{-1}$, giving a Richardson number > 0.25. This is in agreement with other studies that have shown an association between phytoplankton layers and density gradients (Dekshenieks et al. 2001; McManus et al. 2003). Properties of all particle concentration peaks are shown in Table 3. Peaks in bulk fluorescence were located on average at depths of 37.6 m, and had an average thickness of 1.58 m. Only 61% of peaks in bulk fluorescence were located in regions of buoyancy frequency $> 0.01\ s^{-1}$, not significantly higher than the occurrence of these regions in the water column as a whole. Properties of all bulk fluorescence peaks are shown in Table 4.

Cryptic peaks and bulk fluorescence–only peaks—We observed only two occurrences of coincident peaks in fluorescent particle concentration and bulk fluorescence. Thus, 17 of the 19 peaks in particle concentration (89.5%) were not accompanied by a concurrent peak in bulk fluorescence and were defined as cryptic peaks. Likewise, 16 of the 18 peaks in bulk fluorescence (88.9%) were bulk fluorescence–only peaks—that is, they had no concurrent peak in fluorescent particle concentration. These cryptic peaks and bulk fluorescence–only peaks can be easily recognized by comparing the disparities in bulk fluorescence and fluorescent particle concentration profiles (Fig. 7). At least one cryptic peak was found in 9 of the 11 drops analyzed (Table 3). On the contrary, fluorescence-only peaks were only found in 5 of the 11 drops analyzed, with the majority of fluorescence-only peaks in the first two drops (Table 4). Particles within cryptic peaks (i.e., within the thickness of the peak as defined earlier) accounted for 19.8% of all particles counted in all drops. In contrast, the integrated fluorescence of bulk fluorescence–only peaks represented only 7.1% of the total bulk fluorescence in all drops combined. Although 71% of cryptic peaks were located in regions of buoyancy frequency $> 0.01\ s^{-1}$, only 56% of bulk fluorescence–only peaks were located in these stable regions of the water column.

Particle characteristics—Peaks on meter scales were common in both the ratio of fp1-5 : fp>5 and fp>5 : 1-5. Peaks in fp1-5 : fp>5 indicate an increase in the relative concentration of particles with lengths between 1 and 5 pixels. Conversely, peaks in fp>5 : fp1-5 indicate an increase in the relative concentration of particles with lengths > 5 pixels. Peaks in fp1-5 : fp>5 often coincided with cryptic peaks: 10 of the 17 observed cryptic peaks (59%) had coincident peaks in fp1-5 : fp>5 (Fig. 8). This implies that the high fluorescent particle concentrations of cryptic peaks were due to disproportionately high concentrations of the smaller sized particles with lengths between 1 and 5 pixels. No cryptic peaks coincided with peaks in fp>5 : fp1-5. This suggests that the increase in fluorescent particle concentration within cryptic peaks was caused largely by an increase in phytoplankton (large eukaryotes,

Table 4. List of all bulk fluorescence peaks identified in each drop. Depth, thickness (defined as the full-width half-peak), density, and buoyancy frequency are given for each peak. Bulk fluorescence–only peaks (i.e., bulk fluorescence peaks with no coincident peaks in fluorescent particle concentration) are indicated by asterisks.

Bulk fluorescence peaks	Depth (m)	Thickness (m)	Density (kg m^{-3})	Buoyancy frequency (s^{-1})
Drop 3-1				
A*	26.7	3.32	1025.261	0.0104
B	31.2	2.83	1025.344	0.0144
C*	36.0	0.83	1025.478	0.0348
D*	38.1	0.88	1025.548	0.0080
E*	40.5	0.76	1025.572	0.0170
F*	48.3	0.84	1025.658	0.0060
Drop 3-2				
A*	26.7	0.76	1025.339	0.0164
B*	29.7	0.88	1025.394	0.0316
C*	34.8	0.79	1025.550	0.0084
D*	40.5	0.86	1025.597	0.0403
E*	45.3	0.76	1025.663	0.0071
Drop 4-1				
No peaks				
Drop 4-2				
A*	40.2	1.26	1025.680	0.0075
B*	49.2	2.69	1025.782	0.0088
C*	57.9	0.93	1025.934	0.0075
Drop 5-1				
No peaks				
Drop 6-1				
A*	24.0	3.04	1025.161	0.0105
B*	40.5	0.94	1025.376	0.0277
C*	45.3	1.39	1025.472	0.0155
Drop 7-1				
No peaks				
Drop 7-2				
A	21.3	4.61	1025.112	0.0183
Drop 8-2				
No peaks				
Drop 9-2				
No peaks				
Drop 9-3				
No peaks				

chains, etc.) rather than an increase in the larger fluorescent aggregates.

Comparison of particle concentration profiles for subsequent drops—Several deployments consisted of multiple drops in succession. The images in these consecutive drops were acquired < 1 h apart, and were separated horizontally by ~ 1 km, depending on the drift of the FIDO-Φ between drops. Although we have information on the time of each drop and the general current conditions, we cannot make more precise estimates of the distance between profiles because of the logistics and time involved in the deployment and recovery of the FIDO-Φ and because the FIDO-Φ cannot be tracked while it is below the surface. For these deployments, profiles of particle concentration vs. depth were cross-correlated to identify whether the profiles were offset in depth. Cross-correlation of the particle concentration profiles of drops 4-1 and 4-2 (deployment-drop) revealed that the highest correlation was achieved when drop 4-1 was lagged 3.9 m downward in depth (i.e., peaks in 4-1 were shallower than in 4-2), with a normalized cross-correlation value of 0.9810 (Fig. 9A). Cross-correlation of the particle concentration profiles of drops 7-1 and 7-2 indicated the highest correlation was achieved when drop 7-1 was lagged 1.2 m upward (peaks in 7-1 were deeper than in 7-2), with a normalized cross-correlation value of 0.9702 (Fig. 9B). Analysis of the hydrographic properties of the peaks in deployments 4 and 7 (indicated by arrows in Fig. 9) showed that these features were also offset in density between subsequent drops, as described in Table 5. In deployment 4, the peaks were found both deeper and on denser isopycnals in the second drop. In deployment 7, all three peaks were found shallower in the second drop; however, although the top peak was on a less dense isopycnal in the second drop, the deeper two peaks were found on denser isopycnals in the second drop.

Discussion

Profiles of in situ fluorescence are often used as a proxy for the distribution of phytoplankton in the water column. The observation of cryptic peaks in almost every drop of our study demonstrates that profiles of the concentration of specific groups of phytoplankton often vary independently from profiles of the bulk fluorescence signal. In addition, profiles of two particle size classes and their relative abundances also showed structure on the scale of meters. These observations demonstrate that components of the phytoplankton community can have significant small-scale vertical structure that is not detected by monitoring Chl *a* or bulk fluorescence.

Cryptic peaks—A cryptic peak is created by an increase in the number of fluorescent particles 1 pixel or larger (greater than ~ 20–100 μm), with little to no change in the bulk fluorescence. This could only occur if the fluorescence of the particles creating the peak constituted a small fraction of the bulk fluorescence; otherwise, the large variations in fluorescent particle concentration would also cause variations in the bulk fluorescence. During our study, the fluorescent particles counted in our images (above the fluorescence threshold) accounted for only 10.4% of the bulk fluorescence averaged over all the FIDO-Φ images in all drops. Thus, because the fluorescence due to the particles was a small fraction of the total fluorescence, even a dramatic local change in the abundance of the large fluorescent particles resolved by the FIDO-Φ did not contribute much to changes in the bulk fluorescence signal. Furthermore, our analyses confirm that the cryptic peaks are not a consequence of the data manipulations because the particle peaks were robust to changes in the fluorescence threshold and the binning or smoothing used.

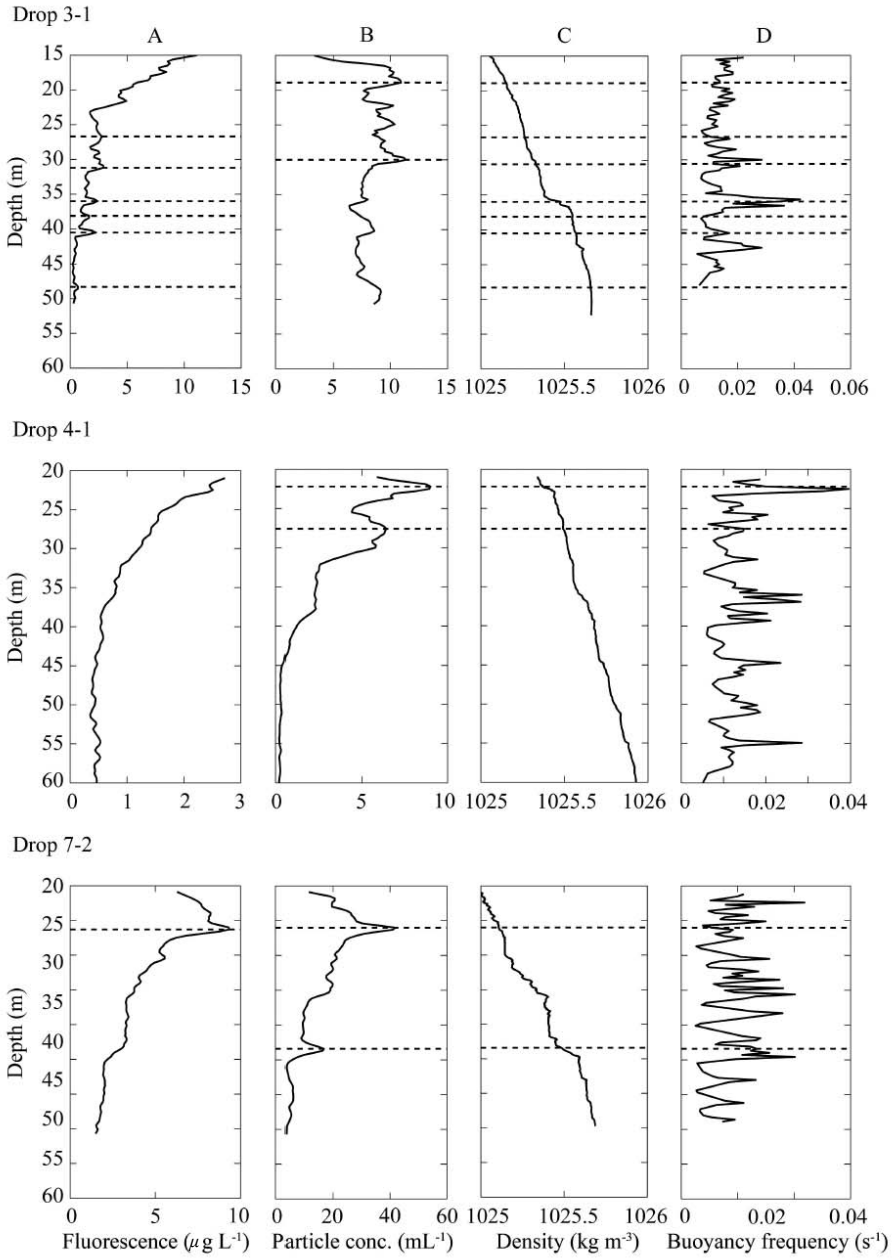

Fig. 7. Comparison of vertical profiles for drop 3-1 (top row), drop 4-1 (middle row), and drop 7-2 (bottom row). (A) Profiles of bulk fluorescence derived from the FIDO-Φ images. Horizontal dotted lines indicate bulk fluorescence peaks. (B) Profiles of fluorescent particle concentration derived from the FIDO-Φ images. Horizontal dotted lines indicate fluorescent particle concentration peaks. (C) Profiles of water density from the SCAMP. Horizontal dotted lines indicated locations of peaks in both bulk fluorescence and fluorescent particle concentration. (D) Profiles of buoyancy frequency calculated from the SCAMP. Horizontal dotted lines indicate locations of peaks in both bulk fluorescence and fluorescent particle concentration.

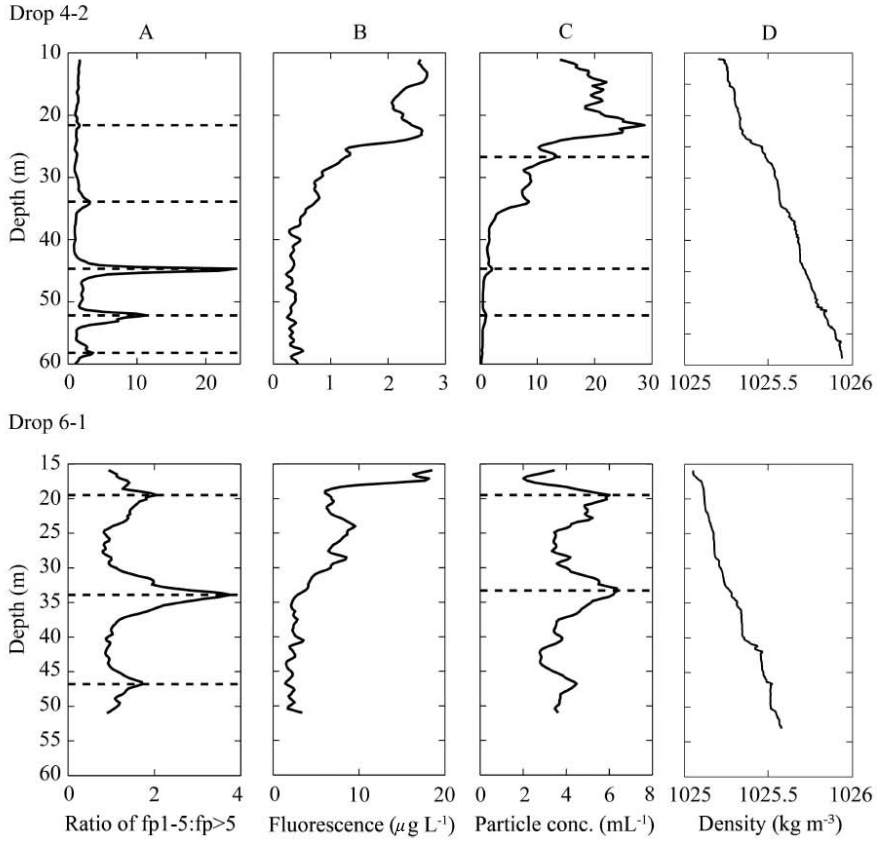

Fig. 8. Comparison of profiles of fp1-5 : fp>5 with profiles of bulk fluorescence derived from the FIDO-Φ images and total fluorescent particle concentration derived from the FIDO-Φ images for drop 4-2 (top row) and drop 6-1 (bottom row). (A) Profile of fp1-5 : fp>5, with peaks in ratio indicated by dotted lines. (B) Profile of total bulk fluorescence derived from the FIDO-Φ images. (C) Profile of total fluorescent particle concentration derived from the FIDO-Φ images with location of cryptic peaks indicated by dotted lines.

Bulk fluorescence–only peaks—We frequently observed bulk fluorescence–only peaks—that is, peaks in bulk fluorescence with no coincident peak in particle concentration. The presence of bulk fluorescence–only peaks demonstrates a significant increase in the bulk fluorescence, with little to no change in the concentration of fluorescent particles 1 pixel or larger. The bulk fluorescence is composed mainly (89.6% on average) of the smallest fluorescent particles (the background fluorescence below the fluorescence threshold). These bulk fluorescence–only peaks therefore represent increases in the concentrations of picoplankton, independent of changes in the large fluorescent particles resolved by the FIDO-Φ. Bulk fluorescence–only peaks show that peaks in bulk fluorescence or Chl *a* do not always represent increases in the concentration of the larger phytoplankton, again emphasizing the difference between these two measures of phytoplankton structure.

Peaks in fp1-5 : fp>5 and fp>5 : fp1-5—In addition to the differences we observed between the bulk fluorescence and particle concentration data, we also observed significant changes in the composition of particles within the fluorescent particle concentration profiles. We frequently saw peaks meters thick in both fp1-5 : fp>5 and fp>5 : fp1-5. Moreover, peaks in fp1-5 : fp>5 frequently coincided with the presence of cryptic peaks, whereas peaks in fp>5 : fp1-5 never coincided with the presence of cryptic peaks. This indicates that cryptic peaks were primarily composed of the smaller size class of particles (phytoplankton between 1 and 5 pixels in length), rather than the larger particles (mostly fluorescent aggregates). Cryptic peaks thus represent regions with phytoplankton compositions different from other parts of the water column.

Do cryptic peaks represent layers?—The primary difference between the identification of peaks in our study and the definition of layers in the literature is that layers must be coherent in time and space (Dekshenieks et al. 2001; Ryan et al. 2008; Cheriton et al. 2009). For most of the cryptic peaks we observed, our sampling did not permit us

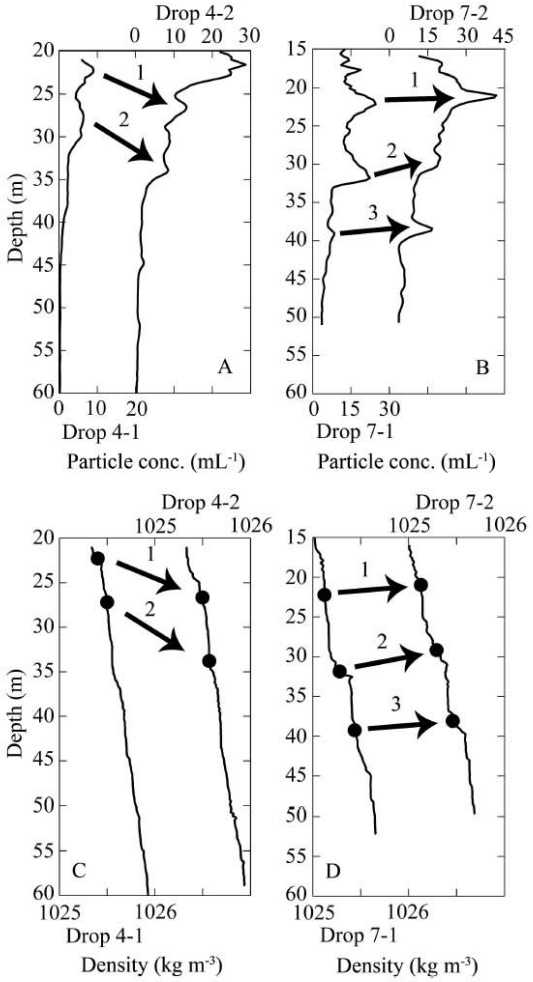

Fig. 9. (A) Fluorescent particle concentration profiles for drop 4-1 (left) and drop 4-2 (right). Cross-correlation reveals the highest correlation (0.9810) when drop 4-1 is lagged 3.9 m downward. Arrows and numbers indicate peaks that are likely the same in each profile. (B) Fluorescent particle concentration profiles for drop 7-1 (left) and drop 7-2 (right). Cross-correlation indicates the highest correlation (0.9702) when drop 7-1 is lagged 1.2 m upward. Arrows and numbers indicate peaks that are likely the same in each profile. (C) Density profiles for drop 4-1 and drop 4-2 as calculated from the SCAMP. Arrows and numbers indicate the same peaks in A. Black dots indicate the location of the peaks on the respective density profiles. (D) Density profiles for drop 7-1 and drop 7-2 as calculated from the SCAMP. Arrows and numbers indicate the same peaks as in part B. Black dots indicate the location of the peaks on the respective density profiles.

to verify the horizontal extent of the features. However, two deployments of the FIDO-Φ consisted of two drops in succession, allowing us to compare subsequent profiles of particle concentration and bulk fluorescence.

Table 5. Density offsets of peaks in deployments 4 and 7 (peaks defined in Fig. 7).

Deployment-peak	Density offset	Drop where peak is denser
4-1	0.1154 kg m^{-3}	4-2 (second drop)
4-2	0.0530 kg m^{-3}	4-2 (second drop)
7-1	0.018 kg m^{-3}	7-1 (first drop)
7-2	0.0444 kg m^{-3}	7-2 (second drop)
7-3	0.0422 kg m^{-3}	7-2 (second drop)

Pairs of drops from deployments 4 and 7 were separated in time by less than an hour and were separated horizontally by a distance on the order of a kilometer. These pairs of drops revealed several highly correlated peaks of fluorescent particle concentration (Fig. 9). Cross-correlation indicated that corresponding peaks in particle concentration profiles of drops 4-1 and 4-2 were found deeper in the second drop, drop 4-2. By contrast, corresponding peaks in particle concentration profiles of drops 7-1 and 7-2 were found deeper in the first of the two drops, drop 7-1. This strong correlation between the peaks in these subsequent drops indicates that these particle concentration peaks could be parts of horizontal layers with extents greater than the separation between the drops.

Mechanisms of layer formation—No single biological or physical mechanism accounts for the formation of thin layers in all environments. Many biological and physical mechanisms of layer formation have been proposed (Derenbach et al. 1979; Franks 1995; Birch et al. 2009), including mechanisms that describe layer formation by straining through vertical shear and by phytoplankton motility or buoyancy (Stacey et al. 2007; Birch et al. 2008). Several studies have inferred the relative importance of a given mechanism for a particular layer (Gallager et al. 2004; Cheriton et al. 2009; Sullivan et al. 2010). Although we cannot resolve the exact mechanisms by which the cryptic peaks observed in this study were formed, we were able to qualitatively explore the importance of specific mechanisms by analyzing the concurrent physical and biological data. Of all the particle concentration peaks observed, the majority (74%) were found in regions of stable water (> 0.01 s^{-1} buoyancy frequency) relative to the water column as a whole. Additionally, water samples taken before and after the FIDO-Φ deployments revealed the community of phytoplankton > 20 μm was almost entirely composed of nonmotile chain diatom species ($\sim$ 95% on average by number), the most abundant of which belonged to the genera *Pseudo-nitzschia*, *Chaetoceros*, *Thalassiosira*, and *Nitzschia*. Peaks lying on strong density gradients and composed of passive (nonswimming) particles are consistent with formation by shear (Franks 1995; Stacey et al. 2007; Birch et al. 2008) or variable sinking rates because of density gradients (Derenbach et al. 1979). Observing how the peaks changed horizontally can aid in distinguishing between the relative likelihood of these two mechanisms because formation by shear would be indicated by horizontal layers tilted across isopycnals (Eckart

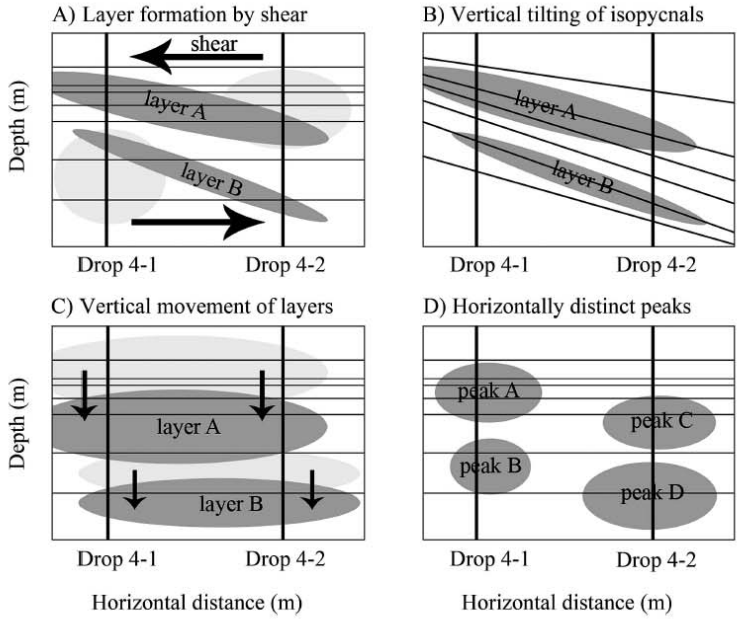

Fig. 10. Schematic of four proposed mechanisms for the offset in depth observed for peaks of high particle concentration found in drops 4-1 and 4-2 (indicated by heavy vertical lines). (A) Peaks offset in depth because of layer formation by shear. Existing phytoplankton patches (shown in light gray) can be thinned out by vertical shear, producing layers (shown in darker gray) tilted across isopycnals (horizontal lines). When these layers are sampled at two locations separated by some horizontal distance, corresponding peaks will be offset in both depth and density (Eckart 1948). (B) Peaks offset in depth because of tilting of the isopycnals on which the layers lie. Peaks have no offset in density. (C) Downward vertical movement of peaks by swimming or sinking of particles. Although the layers are not tilted, when sampled during drop 4-1 (shown in light gray), the peaks are shallower than when sampled during drop 4-2 (shown in darker gray). (D) Separate peaks, disconnected horizontally.

1948; Franks 1995; Birch et al. 2008). Here, by examining the depth offsets observed between the highly correlated peaks in subsequent drops in deployments 4 and 7 (Fig. 9), we explore these hypotheses in more detail.

Four likely mechanisms explain these offsets in the depths of peaks between subsequent drops: horizontal tilting of the layers from vertical shearing of patches, vertical tilting of isopycnals on which layers lie, vertical movement of the layers by swimming or sinking, and distinct peaks that were unconnected horizontally. We now explore each of these possible mechanisms to try to identify those that are consistent with our data.

Vertical shearing of an existing patch of phytoplankton will lead to layers tilted across isopycnals (Fig. 10A; Franks 1995; Birch et al. 2008). That is, the same peak should be found on different isopycnals in horizontally separated vertical profiles. However, if the isopycnals are tilted horizontally, or moved vertically by internal waves, it is possible that a layer lying on the same density surface will be found at different depths in subsequent drops (Fig. 10B). Examination of the water densities at the peaks showed that the peaks were found both at different depths *and* different density surfaces in pairs of drops. Thus, even accounting for the changes of isopycnal depths between drops, the layers must have been inclined across density surfaces, consistent with their formation by vertical shearing of an existing patch of phytoplankton.

Because pairs of drops were not coincident in time, we cannot eliminate the possibility that these peaks were part of layers that were not tilted horizontally in depth and density, but rather were formed by phytoplankton moving vertically by swimming or sinking (Fig. 10C). Layer formation has been proposed to occur both by the slowing of vertically migrating motile phytoplankton at strong shear layers (Durham et al. 2009) and by locally decreased sinking speeds of particles (Derenbach et al. 1979; MacIntyre et al. 1995). Both of these processes are expected to occur at regions of locally high density gradient because such gradients are necessary to support strong shear layers and will lead to rapid changes in sinking speed with depth. These hypotheses are consistent with our observations that cryptic peaks are often associated with regions of high buoyancy frequency. By comparing the time between drops and the vertical offset in depth, we can calculate the approximate swimming or sinking speed required to account for the observed depth offset. Drops 4-1 and 4-2

were separated in time by ~ 55 min (calculated from the time the FIDO-Φ reached equivalent depths in each profile). With the observed depth offset of 3.9 m, this would imply a sinking or downward swimming speed of ~ 0.118 cm s^{-1}. This would be an extremely high sinking speed even for large particles (MacIntyre et al. 1995). In the case of deployment 7, the cross-correlation analysis suggested that the peaks had moved upward. With drops 7-1 and 7-2 separated by ~ 60 min, this would imply an upward vertical swimming speed of 0.033 cm s^{-1} and eliminates entirely the possibility of the peaks moving because of sinking. Because motile phytoplankton consistently contributed < 5% of the total abundance of large phytoplankton, however, peak formation by swimming is improbable for the cryptic peaks observed in this study. Thus, it is very unlikely that the depth and density offsets observed between pairs of drops during deployments 4 and 7 were caused by vertical movements of the plankton forming the peaks.

Possibly the high–particle concentration peaks in successive drops were offset in depth because they were distinct patches, unconnected horizontally (Fig. 10D). However, such a strong cross-correlation between multiple peaks in the paired particle concentration profiles makes this scenario seem unlikely.

These analyses suggest that the cryptic peaks observed in deployments 4 and 7 (Fig. 9), composed largely of nonmotile chain-forming diatoms, were coherent horizontally and represented part of a layer that was tilted vertically across isopycnals. Thus, the most probable mechanism for their formation is by vertical shearing of existing patches of phytoplankton (Franks 1995; Birch et al. 2008).

Vertical shear is found almost everywhere in the ocean, driven by wind, tides, geostrophic currents, and a host of other baroclinic processes. In field studies, shear has been shown to be an important mechanism in the formation of layers (Ryan et al. 2008). Any process that creates horizontal patchiness of biological properties should form thin layers of those properties in the presence of vertical shear (Birch et al. 2008). As we have shown, these peaks do not have to be peaks of enhanced Chl *a* fluorescence—they can be peaks of any property of the ecosystem, including taxonomic composition or metabolic activity. Because of technological limitations, such peaks are typically undetectable by traditional sampling methods. However, we predict that cryptic peaks should be ubiquitous features of the world's oceans. Hopefully, improved technologies will continue to reveal the spatial and temporal complexity of the environment on the scales relevant to individual planktonic organisms.

Ecological implications of cryptic peaks—Our data showing that phytoplankton community structure can vary independently of Chl *a* fluorescence has strong implications for processes involving individual organisms at the microscale, including zooplankton foraging and aggregate formation. For example, our observations demonstrate that fluorescence profiles might not always represent the prey patchiness experienced by herbivorous zooplankton, which have been shown to be able to seek out and remain in areas of high food concentration (Bird and Kitting 1982; Tiselius 1992; Menden-Deuer and Grünbaum 2006). Additionally, patchy prey distributions can significantly affect predator feeding and growth rates (Davis et al. 1991; Montagnes et al. 1999; Leising and Franks 2000). Similarly, the formation of aggregates—a process with important implications for carbon flux in the oceans—is strongly determined by the distribution of individual particles in the water column because particle contact rates scale as the square of particle concentration (Jackson 1990; Kiørboe 1997). Cryptic peaks might thus represent disproportionately intense regions for these processes relative to the rest of the water column. Furthermore, our finding that these features contained almost 20% of the total number of fluorescent particles we counted in all drops during our study underscores their potential importance to fundamental ecosystem processes.

Cryptic peaks—peaks of increased fluorescent particle concentration that do not appear in profiles of bulk fluorescence—were found to be common features of the euphotic zone. Additionally, we frequently observed bulk fluorescence–only peaks—that is, peaks in the bulk fluorescence with no coincident peaks in fluorescent particle concentration. By looking at profiles of two particle size classes, we found that the size composition of the phytoplankton community also displayed variability on meter scales. We hypothesize that the peaks we observed formed through vertical shearing of existing patches. Given the ubiquity of vertical shear and horizontal patchiness, we suggest that fine-scale structure in the distribution of phytoplankton, undetected by instruments measuring bulk fluorescence, is common in coastal waters and a predictable feature of planktonic ecosystems.

The differences that can often exist between distributions of bulk fluorescence and the concentration of fluorescent particles (> 20–100 μm) emphasize the importance of understanding how these two measures of phytoplankton distribution relate to one another. The presence of cryptic peaks and bulk fluorescence–only peaks demonstrates that bulk fluorescence and particle concentration could be providing distinct information about planktonic ecosystems: although bulk fluorescence is relevant to questions involving bulk properties of phytoplankton communities, the concentration of specific groups or sizes of phytoplankton is central to questions concerning individual processes of ecosystem dynamics for those phytoplankton. Further examination of the extent of small-scale structure of planktonic organisms will be important for understanding their underlying dynamics and their implications to zooplankton foraging, aggregation formation, and carbon fluxes in the ocean.

Acknowledgments

We thank F. Simonet, P. Roberts, and Y. Platoshyn for their help in designing, building, and deploying the free-fall imaging device for observing phytoplankton (FIDO-Φ) and E. Karaköylü and A. Lucas for their help configuring the auxiliary instrumentation. We thank E. Daniels and C. Anderson for the shipboard conductivity-temperature-depth (CTD) deployments and processing chlorophyll samples and H. McClelland for analyzing samples

for species composition. Additionally, we thank two anonymous reviewers whose substantial helpful comments greatly improved the quality of this manuscript.

This work was supported by the U.S. Office of Naval Research grant N00014-06-1-0304 and the National Science Foundation grant Division of Ocean Sciences 08-25154.

References

Birch, D. A., W. R. Young, and P. J. S. Franks. 2008. Thin layers of plankton: Formation by shear and death by diffusion. Deep-Sea Res. I **55:** 277–295, doi:10.1016/j.dsr.2007.11.009

———, ———, and ———. 2009. Plankton layer profiles as determined by shearing, sinking and swimming. Limnol. Oceanogr. **54:** 397–399.

Bird, J. L., and C. L. Kitting. 1982. Laboratory studies of a marine copepod (*Temora turbinata* Dana) tracking dinoflagellate migrations in a water column. Contrib. Mar. Sci. **25:** 27–44.

Bjornsen, P. K., and T. G. Nielsen. 1991. Decimeter scale heterogeneity in the plankton during a pycnocline bloom of *Gyrodinium aureolum*. Mar. Ecol. Prog. Ser. **73:** 263–267, doi:10.3354/meps073263

Cheriton, O. M., M. A. McManus, M. T. Stacey, and J. V. Steinbuck. 2009. Physical and biological controls on the maintenance and dissipation of a thin phytoplankton layer. Mar. Ecol. Prog. Ser. **378:** 55–69, doi:10.3354/meps07847

Cowles, T. J., R. A. Desiderio, and M. Carr. 1998. Small-scale planktonic structure: Persistence and trophic consequences. Oceanography **11:** 4–9.

Cudaback, C. N., and E. Mcphee-Shaw. 2009. Diurnal-period internal waves near point conception, California. Estuar. Coast. Shelf Sci. **83:** 349–359, doi:10.1016/j.ecss.2008.12.018

Davis, C. S., G. R. Flierl, P. H. Wiebe, and P. J. S. Franks. 1991. Micropatchiness, turbulence, and recruitment in plankton. J. Mar. Res. **49:** 109–151, doi:10.1357/002224091784968602

———, S. M. Gallager, M. Marra, and W. K. Stewart. 1996. Rapid visualization of plankton abundance and taxonomic composition using the Video Plankton Recorder. Deep-Sea Res. II **43:** 1947–1970, doi:10.1016/S0967-0645(96)00051-3

———, ———, and A. R. Solow. 1992. Microaggregations of oceanic plankton observed by towed video microscopy. Science **257:** 230–232, doi:10.1126/science.257.5067.230

Dekshenieks, M. M., P. L. Donaghay, J. M. Sullivan, J. E. B. Rines, T. R. Osborn, and M. S. Twardowski. 2001. Temporal and spatial occurrence of thin phytoplankton layers in relation to physical processes. Mar. Ecol. Prog. Ser. **223:** 61–71, doi:10.3354/meps223061

Derenbach, J. B., H. Astheimer, H. P. Hansen, and H. Leach. 1979. Vertical microscale distribution of phytoplankton in relation to the thermocline. Mar. Ecol. Prog. Ser. **1:** 187–193, doi:10.3354/meps001187

Desiderio, R. A., T. J. Cowles, and J. N. Moum. 1993. Microstructure profiles of laser-induced chlorophyll fluorescence spectra: Evaluation of backscatter and forward-scatter fiber-optic sensors. J. Atmos. Ocean. Technol. **10:** 209–224, doi:10.1175/1520-0426(1993)010<0209:MPOLIC>2.0.CO;2

Doubell, M. J., L. Seuront, J. R. Seymour, N. L. Patten, and J. G. Mitchell. 2006. High-resolution fluorometer for mapping microscale phytoplankton distributions. Appl. Environ. Microbiol. **72:** 4475–4478, doi:10.1128/AEM.02959-05

Duda, T. F., and C. R. Rehmann. 2002. Systematic microstructure variability in double-diffusively stable coastal waters of nonuniform density gradient. J. Geophys. Res. **107:** 3144, doi:10.1029/2001JC000844

Durham, W. M., J. O. Kessler, and R. Stocker. 2009. Disruption of vertical motility by shear triggers formation of thin phytoplankton layers. Science **323:** 1067–1070, doi:10.1126/science.1167334

Eckart, C. 1948. An analysis of the stirring and mixing processes in incompressible fluids. J. Mar. Res. **7:** 265–275.

Franks, P. J. S. 1995. Thin layers of phytoplankton: A model of formation by near-inertial wave shear. Deep-Sea Res. I **42:** 75–91, doi:10.1016/0967-0637(94)00028-Q

———, and J. S. Jaffe. 2001. Microscale distributions of phytoplankton: Initial results from a two-dimensional imaging fluorometer, OSST. Mar. Ecol. Prog. Ser. **220:** 59–72, doi:10.3354/meps220059

———, and ———. 2008. Microscale variability in the distributions of large fluorescent particles observed in situ with a planar laser imaging fluorometer. J. Mar. Syst. **69:** 254–270, doi:10.1016/j.jmarsys.2006.03.027

Gallager, S. M., H. Yamazaki, and C. S. Davis. 2004. Contribution of fine-scale vertical structure and swimming behavior to formation of plankton layers on Georges Bank. Mar. Ecol. Prog. Ser. **267:** 27–43, doi:10.3354/meps267027

Harms, S., and C. D. Winant. 1998. Characteristic patterns of the circulation in the Santa Barbara Channel. J. Geophys. Res. **103:** 3041–3065, doi:10.1029/97JC02393

Holliday, D. V., P. L. Donaghay, C. F. Greenlaw, D. E. McGehee, M. A. McManus, J. M. Sullivan, and J. L. Miksis. 2003. Advances in defining fine- and micro-scale pattern in marine plankton. Aquat. Living Resour. **16:** 131–136, doi:10.1016/S0990-7440(03)00023-8

Jackson, G. A. 1990. A model of the formation of marine algal flocs by physical coagulation processes. Deep-Sea Res. **37:** 1197–1211.

Jaffe, J. S., P. J. S. Franks, and A. W. Leising. 1998. Simultaneous imaging of phytoplankton and zooplankton distributions. Oceanography **11:** 24–29.

Katz, J., P. L. Donaghay, J. Zhang, S. King, and K. Russell. 1999. Submersible holocamera for detection of particle characteristics and motions in the ocean. Deep-Sea Res. I **46:** 1455–1481, doi:10.1016/S0967-0637(99)00011-4

Kiorboe, T. 1997. Small-scale turbulence, marine snow formation, and planktivorous feeding. Sci. Mar. **61:** 141–158.

Leising, A. W., and P. J. S. Franks. 2000. Copepod vertical distribution within a spatially variable food source: A simple foraging-strategy model. J. Plankton Res. **22:** 999–1024, doi:10.1093/plankt/22.6.999

MacIntyre, S., A. L. Alldredge, and C. C. Gotschalk. 1995. Accumulation of marine snow at density discontinuities in the water column. Limnol. Oceanogr. **40:** 449–468, doi:10.4319/lo.1995.40.3.0449

Malkiel, E., J. N. Abras, E. A. Widder, and J. Katz. 2006. On the spatial distribution and nearest neighbor distance between particles in the water column determined from in situ holographic measurements. J. Plankton Res. **28:** 149–170, doi:10.1093/plankt/fbi107

McManus, M. A., R. M. Kudela, M. W. Silver, G. F. Steward, P. L. Donaghay, and J. M. Sullivan. 2008. Cryptic blooms: Are thin layers the missing connection? Estuar. Coasts **31:** 396–401, doi:10.1007/s12237-007-9025-4

———, and others. 2003. Characteristics, distribution and persistence of thin layers over a 48 hour period. Mar. Ecol. Prog. Ser. **261:** 1–19, doi:10.3354/meps261001

Menden-Deuer, S., and C. Grünbaum. 2006. Individual foraging behaviors and population distributions of a planktonic predator aggregating to planktonic thin layers. Limnol. Oceanogr. **51:** 109–116.

MITCHELL, J. G., AND J. A. FUHRMAN. 1989. Centimeter scale vertical heterogeneity in bacteria and chlorophyll *a*. Mar. Ecol. Prog. Ser. **54:** 141–148, doi:10.3354/meps054141

MONTAGNES, D. J. S., A. J. POULTON, AND T. M. SHAMMON. 1999. Mesoscale, finescale and microscale distribution of micro- and nanoplankton in the Irish Sea, with emphasis on ciliates and their prey. Mar. Biol. **134:** 167–179, doi:10.1007/s002270050535

NORRBIN, M. F., C. S. DAVIS, AND S. M. GALLAGER. 1996. Differences in fine-scale structure and composition of zooplankton between mixed and stratified regions of Georges Bank. Deep-Sea Res. II **43:** 1905–1924, doi:10.1016/S0967-0645(96)00046-X

RINES, J. E. B., P. L. DONAGHAY, M. M. DEKSHENIEKS, J. M. SULLIVAN, AND M. S. TWARDOWSKI. 2002. Thin layers and camouflage: Hidden *Pseudo-nitzschia* spp. (Bacillariophyceae) populations in a fjord in the San Juan Islands, Washington, USA. Mar. Ecol. Prog. Ser. **225:** 123–137, doi:10.3354/meps225123

RYAN, J. P., M. A. MCMANUS, J. D. PADUAN, AND F. P. CHAVEZ. 2008. Phytoplankton thin layers caused by shear in frontal zones of a coastal upwelling system. Mar. Ecol. Prog. Ser. **354:** 21–34, doi:10.3354/meps07222

STACEY, M. T., ———, AND J. V. STEINBUCK. 2007. Convergences and divergences and thin layer formation and maintenance. Limnol. Oceanogr. **52:** 1523–1532.

SULLIVAN, J. M., P. L. DONAGHAY, AND J. E. B. RINES. 2010. Coastal thin layer dynamics: Consequences to biology and optics. Cont. Shelf Res. **30:** 50–65, doi:10.1016/j.csr.2009.07.009

———, M. S. TWARDOWSKI, P. L. DONAGHAY, AND S. A. FREEMAN. 2005. Use of optical scattering to discriminate particle types in coastal waters. Appl. Optics **44:** 1667–1680, doi:10.1364/AO.44.001667

TISELIUS, P. 1992. Behavior of *Acartia tonsa* in patchy food environments. Limnol. Oceanogr. **37:** 1640–1651, doi:10.4319/lo.1992.37.8.1640

WATERS, R. L., J. G. MITCHELL, AND J. SEYMOUR. 2003. Geostatistical characterisation of centimetre-scale spatial structure of in vivo fluorescence. Mar. Ecol. Prog. Ser. **251:** 49–58, doi:10.3354/meps251049

WINANT, C. D., AND C. E. DORMAN. 1997. Seasonal patterns of surface wind stress and heat flux over the Southern California Bight. J. Geophys. Res. **102:** 5641–5653, doi:10.1029/96JC02801

YAMAZAKI, H., J. G. MITCHELL, L. SEURONT, F. WOLK, AND H. LI. 2006. Phytoplankton microstructure in fully developed oceanic turbulence. Geophys. Res. Lett. **33:** L01603, doi:10.1029/2005GL024103

ZAWADA, D. G. 2002. The application of a novel multispectral imaging system to the in vivo study of fluorescent compounds in selected marine organisms. Ph.D. thesis. Univ. of California, San Diego.

Associate Editor: Heidi M. Sosik

Received: 27 July 2009
Amended: 19 June 2010
Accepted: 21 June 2010

Chapter 2, in full, is a reprint of previously published material as it appears in Limnology and Oceanography, 2010, Prairie, J. C., Franks, P. J. S., and Jaffe, J. S. The dissertation author was the primary investigator and author of this paper.

CHATER III.

UNEXPLAINED VARIABILITY IN THE DISTRIBUTION AND SIZE SPECTRA OF PARTICLES IN THE OCEAN

Abstract

Vertical heterogeneity in phytoplankton abundance, which has recently been observed on the scale of meters in many marine ecosystems, can have significant implications for food web dynamics and carbon cycling. Here, we investigate the implications of small-scale phytoplankton structure for ecosystem dynamics by comparing vertical profiles of fluorescent particle concentration to concurrent profiles of the concentration of particles as a whole in the water column. We observed frequent meter-scale variability in both the concentration of fluorescent particles and total particles; however, at times the distribution of fluorescent particles and total particles varied independently from one another. By analyzing environmental and size spectral parameters within total particle concentration peaks, we draw inferences about the composition of the peaks and their ecological significance. Finally, by analyzing the particle size spectra for both fluorescent particles and particles as a whole, we determine how particle size structure varies in the ocean and its relation with total fluorescent particle concentration and bulk fluorescence. Our results show that the size composition of phytoplankton can fluctuate on small-scales vertically, but is not well predicted by indices of productivity. Small-scale changes in particle size spectra can affect local rates of aggregate formation, grazing, and carbon export; thus, multidisciplinary research on

particle size-spectra will be important to fully resolve small-scale variability in these ecological processes.

Introduction

Phytoplankton play important roles in pelagic marine ecosystems as carbon fixers and the base of the food chain. With recent observations that phytoplankton distributions are vertically heterogeneous on the scale of meters (Cowles et al. 1998; Dekshenieks et al. 2001; Sullivan et al. 2010), many studies have suggested that phytoplankton layers may be regions where many ecological processes, such as zooplankton foraging and aggregate formation, occur at enhanced rates (Alldredge et al. 2002; McManus et al. 2003; Prairie et al. 2010). Although this hypothesis has been supported by significant theoretical and laboratory work (Jackson 1990; Davis et al. 1991; Tiselius 1992; Leising and Franks 2000; Menden-Deuer and Grünbaum 2006), there is still not a strong understanding of the effect of increased phytoplankton concentrations on zooplankton foraging and aggregate formation in the field. To elucidate the implications of phytoplankton patchiness for these ecological processes, it is essential to compare vertical phytoplankton distributions with distributions of their predators and aggregates. Understanding the composition of the phytoplankton community, in particular its size distribution, may provide additional insight into the ecological significance of vertical phytoplankton structure.

A surge of field studies in the past decade has presented observations of phytoplankton and chlorophyll *a* fluorescence peaks and thin layers on the scale of meters (e.g., Rines et al. 2002; Prairie et al. 2010; Ryan et al. 2010). However, few of

these studies have compared these small-scale structures with distributions of other types of ecologically important particles, such as zooplankton or aggregates. Advances in optical and acoustic technologies have allowed the coincident measurement of phytoplankton and zooplankton distributions, often revealing significant small-scale associations between the two groups (Holliday et al. 2003; McManus et al. 2003; Benoit-Bird et al. 2009). Heterotrophic protist abundance has also been shown to be strongly correlated with phytoplankton layers (Menden-Deuer 2008). Many studies have begun to employ the use of in situ video imaging to identify the vertical distributions of many types of particles, including phytoplankton, zooplankton, and aggregates (Jackson et al. 1997; Gorsky et al. 2000; Picheral et al. 2010). Alldredge et al. (2002) observed a thin layer of marine snow particles associated with a density discontinuity just a few meters below a phytoplankton thin layer. Checkley et al. (2008) suggested that observed diel variation in the concentration of particles was consistent with phytoplankton-derived aggregates that were lost due to sinking or grazing. These findings all underscore the importance of vertical phytoplankton patchiness for zooplankton and aggregate formation.

Phytoplankton community composition provides another source of information about phytoplankton distributions. Studies have explored phytoplankton composition in a number of ways, including taxonomy and motility (Rines et al. 2002; Cheriton et al. 2009; Sullivan et al. 2010). However, one of the most informative methods to analyze phytoplankton communities is by size (Sheldon et al. 1972), since particle size distributions have been shown to be connected to many ecological processes, including

phytoplankton growth rate and carbon flux (Shanks and Trent 1980; Zhou and Huntley 1997; McDonnell and Buesseler 2010).

Size spectra in a wide range of marine environments have been shown to be strikingly linear on log-log plots over a broad range of particle sizes (Sheldon et al. 1972; Jackson et al. 1997; San Martin et al. 2006). However, the slope and intercept of these size spectra can vary spatially significantly over both large scales (Barnes et al. 2011) and vertically over small scales (Ruiz et al. 1996; Franks and Jaffe 2008). Relationships between particle size spectral properties and various ecosystem properties, such as chlorophyll *a*, have been demonstrated, but with inconsistent results. While many studies have observed steeper size spectral slopes in less productive ecosystems (Marañón et al. 2007; Barnes et al. 2011), others have shown that steeper slopes can be significantly correlated with higher phytoplankton biomass or total chlorophyll *a* (Ruiz et al. 1996; San Martin et al. 2006; Franks and Jaffe 2008). Although many studies have compared particle size spectra to total fluorescence and chlorophyll *a*, it is also important to uncover how spectral properties vary with phytoplankton concentration, which can differ considerably from chlorophyll *a* fluorescence on meter scales (Prairie et al. 2010).

In this study, we explore the ecological implications of phytoplankton patchiness using data from a planar laser imaging fluorometer, the free-falling imaging device for observing phytoplankton (FIDO-Φ). We present observations of small-scale structure in the vertical distribution of both fluorescent particles and all particles that scatter light; however, we show that there is no consistent pattern of how these two types of particles are associated with one another. Furthermore, by analyzing the size spectra of both fluorescent particles and all particles, we demonstrate that, although some of the size

spectral parameters are significantly correlated with total particle concentration, these relationships did not predict much of the observed vertical variability in size composition. The results of this study suggest that the substantial vertical heterogeneity in phytoplankton distributions and size structure is difficult to explain using simple correlations with certain biological variables, indicating that the dynamics which control vertical phytoplankton distributions include a complex interplay of many different biotic and abiotic factors.

Methods

Description of the FIDO-Φ instrument package

The free-fall imaging device for observing phytoplankton (FIDO-Φ) is a planar laser imaging fluorometer system that can resolve individual fluorescent particles in the imaging plane (Jaffe et al. 1998; Franks and Jaffe 2001; Franks and Jaffe 2008). The FIDO-Φ has a laser and camera mounted on opposite sides of a frame and angled downward at 45˚. The 3 W 532 nm diode-pumped solid-state laser emits a sheet of light 6.5 mm thick that is imaged by the camera at a 90˚ angle, with the center of the image plane ~60 cm below the bottom of the frame. Attached to the camera is a filter wheel with 4 filter slots, which alternates between channels of wavelengths 670-690 nm (chlorophyll *a* fluorescence) and 520-540 nm (scattered light). The filter wheel is a Lambda 4 from Sutter Inc. and changes filters at a rate of 250 ms (or 4 filters per second). The images from the FIDO-Φ have a field of view of ~9.8 cm x 13 cm with a resolution slightly less than 100 μm pixel^{-1}. For a full description of the FIDO-Φ see Prairie et al. (2010).

Auxiliary instruments were attached to the FIDO-Φ to measure various biological and physical variables (Prairie et al. 2010) including a self-contained autonomous microstructure profiler (SCAMP, Precision Measurement Engineering), which was mounted with the probes 48 cm below the depth sensor of the FIDO-Φ. The SCAMP measured temperature, conductivity, and pressure at 100 Hz. The data streams of the different instruments and the FIDO-Φ were merged together based on depth, after the depth offsets were applied.

Description of the 2006 cruise

The FIDO-Φ was deployed at night during a cruise on the R/V *Wecoma* from 31 August 2006 to 07 September 2006 in the Santa Barbara Channel (SBC) off the coast of Southern California. For a complete description and map of the study site, see Prairie et al. (2010). Each deployment of the FIDO-Φ consisted of 1 or 2 consecutive drops with images acquired during the vehicle's descent. Although the FIDO-Φ primarily descends vertically, some horizontal movement occurs due to the semi-Lagrangian nature of the vehicle. This horizontal movement, combined with the effects of internal waves, produced ~10 cm-scale noise in FIDO-Φ data that was removed by binning and smoothing the data (see *Image processing and beam corrections*). This noise was so pronounced in the top 10 to 20 m of the profiles (varying among drops) that these regions were not used in the analyses. The descent rate of the instrument package ranged between 3 to 12 cm s^{-1} among drops, but was relatively constant within a drop. Images of

fluorescent particles were acquired at a rate of 2 Hz. In total, 11 FIDO-Φ drops were used for this analysis (see Prairie et al. 2010).

Profiles were also made with the ship-deployed SBE 911plus CTD system (equipped with a rosette with 10 L Niskin bottles and a WET Labs WETStar fluorometer) before or after each of the FIDO-Φ deployments. Analysis of the water samples included quantifying species composition as described in Prairie et al. (2010).

Image processing and beam correction

The processing of the FIDO-Φ images is described in detail in Prairie et al. (2010); here we provide a brief summary. The raw 1040 x 1376 pixel images were corrected for the spreading of the laser sheet that created systematic variations of signal strength across the image (Zawada 2002). The corrected images show relative fluorescence or scattered light independent of the incident illumination.

Particle concentrations of each image for both the fluorescence (670-690 nm) and scattered light (520-540 nm) filters were calculated by labeling every particle above a threshold in the image (see Prairie et al. 2010) and dividing the number of particles by the imaging volume. For every drop except one, the same threshold was used for both the fluorescence and scattered light filters; for Drop 3-2, it was necessary to use a higher threshold for the scattered light filter in order to exceed the noise level. The threshold was necessary to eliminate the background signal, and resulted in exclusion of the smaller (less bright) particles. Thus, only the largest and brightest particles are included in our profiles of particle concentration. Particles from the fluorescence filter, which will hereafter be referred to as fluorescent particles, include large eukaryotic phytoplankton,

chains, and fluorescent aggregates. Particles from the scattered light filter, which will hereafter be referred to as scattering particles, include large fluorescent particles in addition to zooplankton, detritus, non-fluorescent aggregates, and fecal pellets. Although we cannot definitively determine the minimum size of the particles we count in our images, from instrument specifications and laboratory experiments (Zawada 2002) we estimate that this value is between 20 μm and 100 μm. For a full description of the thresholding process, see Prairie et al. (2010).

Profiles of both fluorescent and scattering particle concentration versus depth were constructed by calculating the number of particles from the respective filter per image at each depth, and dividing it by the volume of the imaged region. These profiles were binned to 30 cm and smoothed using a LOWESS (locally weighted smoothing scatter) method over 1.5 m to remove noise at scales < 30 cm. The smoothing did not remove structures < 1.5 m, but rather attenuated the fluorescence signal of one- or two-point peaks.

Identification of peaks and peak properties

Peaks were identified in the vertical profiles of both fluorescent and scattering particle concentration using the operational definition of local maxima with at least a 50% increase over the local background signal, measured as the nearest minima above and below the peak. This criterion identified significant peaks over the background while eliminating ephemeral features. The depth of a peak was defined as the location of the maximum in peak intensity. The thickness of the peak was defined as the full-width-half-maximum (FWHM) as described in Sullivan et al. (2010). The FWHM is the width of the

peak measured as the sum of the distances from the depth of the peak maximum to the depths above and below the peak at which the intensity was half the peak intensity above the background. The background was defined as the average of the minima surrounding the peak. Peaks with a FWHM thickness greater than 5 m were neglected. The definition of peaks used here differs from the definition of thin layers used in many studies in that thin layers must persist over time and space (Dekshenieks et al. 2001; Ryan et al. 2008; Cheriton et al. 2009).

Calculation of physical parameters

Density profiles were obtained from the SCAMP, binned to 1 cm, and smoothed over 30 cm. The water density at a peak was defined as the density at the peak maximum. The buoyancy frequency, N, is defined as

$$N = \sqrt{-\frac{g}{\rho}\frac{d\rho}{dz}} \quad (1)$$

where g is the acceleration due to gravity, ρ is density, and z is depth. N was calculated from the smoothed SCAMP density data by calculating the change in depth necessary to yield density intervals of $\Delta\rho = 0.005$ kg m^{-3}, as outlined in Duda and Rehmann (2002). This method is numerically stable as it avoids N values of 0 s^{-1}. Buoyancy frequency profiles were linearly interpolated to obtain the buoyancy frequency of the peaks defined at the peak maximum.

Calculation of particle size spectral parameters

Profiles of particle area-abundance spectra were calculated by counting the number of particles of a given area (pixels^2) for each image. These profiles were binned to 30 cm and smoothed using a LOWESS (locally weighted smoothing scatter) method over 1.5 m in the same way as for the particle concentration profiles. Linear regressions of the $\log_{10}$-$\log_{10}$ area-abundance spectra were then calculated for each point in the profile generating the slope (β) and intercept (α) for each spectrum:

$$N = 10^{\alpha} A^{-\beta} \quad (2)$$

where A is area and N is the number of particles of a given area. In plotting the size spectra, only the first ten size bins (up to an area of 10 pixels^2) were used and any points where $N = 0$ were neglected. Note that the slope presented in this paper is actually the negative of the size spectral slope. The mean and standard deviation of the correlation coefficients (r^2) for the least square fits for each drop are provided in Table 3.1. The slope and intercept of the size spectra of each peak were defined as the mean value for the points in the profile within each peak (as defined by the FWHM thickness).

Results

Fluorescent and scattering particle concentration peaks

In total, 20 peaks in fluorescent particle concentration were identified among all drops. Peaks in fluorescent particle concentration were located on average at depths of 28.4 m, and had an average thickness of 2.82 m. The majority of peaks in fluorescent particle concentration (75%) were located in regions of buoyancy frequency > 0.01 s^{-1}, even though these regions represented only about half (55%) of the water column. A

Monte Carlo test (with $n = 20$) showed that the percentage of fluorescent particle concentration peaks in these high buoyancy frequency regions was significantly higher than the water column as a whole, using the $p < 0.10$ level to determine significance ($p = 0.054$). Regions with a buoyancy frequency above 0.01 s^{-1} correspond to stable parts of the water column when the vertical shear values are < 0.02 s^{-1}, giving a Richardson number > 0.25. This is in agreement with other studies that have shown an association between phytoplankton layers and density gradients (Dekshenieks et al. 2001; McManus et al. 2003, Prairie et al. 2010). Properties of all fluorescent particle concentration peaks are shown in Table 3.2.

In total, 19 peaks in scattering particle concentration were identified among all drops. Peaks in scattering particle concentration were located on average at depths of 34.8 m, and had an average thickness of 2.74 m. Only 63% of peaks in scattering particle concentration were located in regions of buoyancy frequency > 0.01 s^{-1}, not significantly higher than the occurrence of these regions in the water column as a whole. Properties of all scattering particle concentration peaks are shown in Table 3.3. Peaks in both fluorescent and scattering particle concentration can be observed in the particle concentration profiles for each drop (Figures 3.1-3.11).

Of the 20 fluorescent particle concentration peaks, 10 coincided with peaks in scattering particle concentration and 10 did not coincide with peaks in scattering particle concentration. Thus, 9 of the 19 peaks in scattering particle concentration did not coincide with peaks in fluorescent particle concentration. When peaks in fluorescent and scattering particle concentration coincided, the peak maximum for fluorescent particle concentration was on average 0.1 m (+/- 1.0 m standard deviation) deeper than that for

scattering particle concentration. The peaks in fluorescent particle concentration that did not coincide with peaks in scattering particle concentration were located 7.4 m shallower than the peaks in fluorescent particle concentration that did coincide with peaks in particle concentration. By contrast, the peaks in scattering particle concentration that did not coincide with peaks in fluorescent particle concentration were located on average 5.8 m deeper than the peaks in scattering particle concentration that did coincide with peaks in particle concentration.

In most drops, fluorescent particle concentration was significantly positively correlated with scattering particle concentration, although three drops (Drop 8-2, Drop 9-2, and Drop 9-3) showed a significant negative correlation (Table 3.4). To compare fluorescent particle concentration and scattering particle concentration for all drops combined, the fluorescent and scattering particle concentration anomalies were plotted against each other. The anomaly for a given point *i* in a particle concentration profile (either fluorescent or scattering) was defined as:

$$A_{PC}(i) = \frac{PC(i) - \overline{PC}}{s_{PC}} \tag{3}$$

Where A_{PC} is the particle concentration anomaly at point *i*, PC is the particle concentration at point *i*, $\overline{PC}$ is the mean particle concentration for the drop, and s_{PC} is the standard deviation of particle concentration for the drop. The fluorescent particle concentration anomaly for all drops was weakly but significantly positively correlated to the scattering particle concentration anomaly (Figure 3.12) ($r^2 = 0.03$; $p < 0.0001$).

Particle concentration size spectra

Profiles of the slope and intercept of the fluorescent and scattering particle size spectra are shown for each drop (Figures 3.1-3.11). For the majority of drops, the size spectral intercept was positively correlated with fluorescent and scattering particle concentration, while the size spectral slope showed varying relationships with fluorescent and scattering particle concentration between drops. When all drops were combined, fluorescent size spectral slope showed no significant relationship with fluorescent particle concentration, while scattering size spectral slope showed a weak negative correlation with scattering particle concentration (that is, lower particle concentration yielded steeper size spectral slopes). For both fluorescent and scattering particles, the size spectral intercept was strongly positively correlated with particle concentration (Figure 3.13). There was a significant negative correlation between fluorescent size spectral slope and total bulk fluorescence – that is, steeper spectral slopes were found in regions of low fluorescence (Figure 3.14). In addition, fluorescent size spectral intercept was positively correlated with total bulk fluorescence.

The mean slope of the size spectra for fluorescent particles within peaks among all drops was 0.95 with a standard deviation of 0.17. This was not significantly different from the mean slope of the fluorescent particle size spectra overall (0.94 with a standard deviation of 0.20). The mean intercept of the size spectra for fluorescent particles within peaks among all drops was 2.04 $\log_{10}$ number of particles with a standard deviation of 0.38. This was significantly greater than the mean intercept of the size spectra for fluorescent particles overall (1.68 $\log_{10}$ number of particles with a standard deviation of 0.49) ($p < 0.0001$).

The mean slope of the size spectra for scattering particles within peaks among all drops was 0.84 with a standard deviation of 0.14. This was less steep than the mean slope of the size spectra for scattering particles overall (0.89 with a standard deviation of 0.14) ($p < 0.0001$). The mean intercept of the size spectra for scattering particles within peaks among all drops was 2.23 $\log_{10}$ number of particles with a standard deviation of 0.31. This was significantly less than the mean intercept of the size spectra for scattering particles among all drops (2.28 $\log_{10}$ number of particles with a standard deviation of 0.48) ($p = 0.02$).

Overall, fluorescent and scattering size spectral slopes were significantly positively correlated (Figure 3.15; $p < 0.0001$). On average, slopes of the fluorescent size spectra were steeper than those for the scattering size spectra by 0.04 ($p < 0.0001$). This difference was even greater within peaks (with the fluorescent size spectral slopes steeper than the scattering size spectral slopes by an average of 0.11). However, within only coincident peaks of fluorescent and scattering particle concentration, there was no significant difference between the size spectral slopes of the two types of particles.

Discussion

Comparing fluorescent and scattering particle concentration

The observation of frequent fluorescent and scattering particle concentration peaks during the 2006 cruise demonstrates that the vertical distribution of not only fluorescent particles but also particles as a whole had significant structure on the scale of meters. Ten coincident peaks in fluorescent and scattering particle concentration show

that at times the distributions of these two types of particles can be highly correlated. However, the vertical distribution of fluorescent and scattering particle concentration can also significantly vary independently, as indicated by the presence of peaks in fluorescent particle concentration with no concurrent feature in scattering particle concentration and vice versa.

The composition of scattering particle concentration peaks

Scattering particles in the FIDO-Φ images include detritus, aggregates, and zooplankton in addition to all the particles counted in the fluorescence images (i.e. large phytoplankton, diatom chains, fluorescent aggregates). The broad range of particle types counted in the measure of scattering particle concentration makes it difficult to diagnose what is responsible for the observed scattering particle concentration peaks. However, by comparing these peaks to the distribution of environmental variables and other properties, we can gain information about the peak composition and formation mechanism.

If we assume that the nine scattering particle concentration peaks that did not coincide with fluorescent particle concentration peaks were largely composed of non-fluorescent particles, then these peaks probably represent regions of enhanced concentrations of aggregates, detrital particles, zooplankton or some combination thereof. To distinguish between these possibilities, it is useful to consider the physical environment and the possible layer formation mechanisms. Studies have proposed a wide range of plausible mechanisms for layer formation, including enhanced organism growth, directed swimming, differential sinking, and straining of existing patches by vertical shear (Derenbach et al. 1979; Franks 1995; Stacey et al. 2007; Birch et al. 2008). The

mechanisms which can be applied to passive particles (i.e., layer formation by sinking or shearing) require the layers to be in regions of weak mixing, which can be identified by high stratification (Steinbuck et al. 2009; Prairie et al. in press). However, the percentage of scattering particle concentration peaks observed in regions of high buoyancy frequency was not significantly higher than the occurrence of these regions in the water column as a whole. This suggests that at least some of these scattering particle concentration peaks could not have been composed of passive particles such as aggregates or detritus, since layers of these types of particles would not be able to persist in these regions of potentially high mixing. Thus, some of these scattering particle concentration peaks may represent regions of increased zooplankton abundance. Such layers are likely formed by zooplankton swimming behavior in response to prey. The absence of coincident phytoplankton layers may indicate that zooplankton have depleted phytoplankton concentrations through grazing. Since all peaks were observed at night, layers of vertically migrating zooplankton would be expected to be migrating upwards from depth. The fact that the scattering particle concentration peaks were on average deeper than the fluorescent particle (i.e., potential prey) concentration peaks thus supports the conclusion that some of the observed scattering peaks represented regions of enhanced foraging zooplankton.

It is much more difficult to ascertain the composition of the ten scattering particle concentration peaks that coincided with fluorescent particle concentration peaks, since many or even the majority of these scattering particles could have also been fluorescent. From our data, it is impossible to determine the absolute fraction of scattering particles that were fluorescent. However, differences in the size distributions of fluorescent and

scattering particles may provide clues as to how different size classes of these two types of particles vary in relation to one another. Overall, fluorescent particles had steeper size spectral slopes than scattering particles, indicating a higher proportion of the scattering particles were in the larger size classes. There are a couple of possible reasons for this observed difference in size spectral slopes. This could indicate that the non-fluorescent particles (which only appear in the scattering filter) were on average larger particles. On the other hand, aggregates consisting of some but not totally of fluorescent material could appear larger in the scattering filter than in the fluorescent filter, thus skewing the size distribution. Regions where this difference in size spectral slope is enhanced, for example within non-coincident peaks of scattering particle concentration, show an increase in the relative proportion of these non-fluorescent large particles. However, our results show that in *coincident* peaks of fluorescent and scattering particle concentration, there was no significant difference between the size spectral slopes. This is suggestive that, within these peaks, scattering particles may be dominated by fluorescent particles.

Although we can gain some insight by comparing parameters of the particle size spectra, limitations of our data prohibit us from definitively concluding whether the scattering peaks which coincided with fluorescent particle peaks were created solely from the increase in fluorescent particles, or whether there was a coincident increase of non-fluorescent particles (e.g., a peak of increased zooplankton abundance). Vertical phytoplankton patches have been shown experimentally, theoretically, and even in the field to be regions of increased foraging for zooplankton (Tiselius 1992; Leising and Franks 2000; Menden-Deuer and Grünbaum 2006; Menden-Deuer and Fredrickson 2010). Additionally, regions of enhanced phytoplankton abundance may represent

regions of increased aggregate formation (Jackson 1990; Kiørboe 1997). The ecological relevance of phytoplankton peaks to other organisms and processes emphasizes the importance of being able to distinguish between phytoplankton and other types of particles when investigating vertical particle distributions in the ocean.

Particle size spectra

It is important to understand how particle size spectra vary in pelagic ecosystems since particle size distributions can reveal information about ecosystem processes such as food web dynamics and carbon cycling (Shanks and Trent 1980; McDonnell and Buesseler 2010; Barnes et al. 2011). Although many studies have shown that particle size spectra can differ strikingly in different parts of the ocean (San Martin et al. 2006; Barnes et al. 2011), there has been little analysis on how size spectra change with depth. Our data reveal that both the slope and intercept of particle size spectra can fluctuate significantly with depth on the scale of meters (Figures 3.1-3.11); this finding agrees with previous results using data from the FIDO-Φ (Franks and Jaffe 2008). These small-scale vertical changes in the particle size spectra suggest that phytoplankton species composition is rarely homogeneous throughout the water column, in accordance with studies that have presented observations of phytoplankton layers with unique compositions relative to the rest of the water column (Rines et al. 2002; Prairie et al. 2010). These changes in phytoplankton composition – whether by size, taxonomy or other properties – have important implications for zooplankton foraging, aggregate formation and other ecological processes that depend on the interaction of individual particles (Kiørboe 1997).

Our results also demonstrate the differences between size spectral properties for fluorescent particles and scattering particles. Vertical profiles of both the slope and intercept of the fluorescent particle size spectra often differed markedly from those of the scattering particle size spectra (Figures 3.1-3.11). Although this may not seem like a surprising result, given what these two types of particles represent, most previous analyses of particle size structure have not distinguished between the two particle types. This has been somewhat driven by the long-standing view originally put forth by Sheldon et al. (1972) that roughly equal concentrations of material should occur for all particle sizes ranging from bacteria to whales. Additionally, many commonly used methods to measure particle size spectra, such as in situ imaging devices, are not capable of distinguishing between phytoplankton and non-fluorescent particles (Jackson et al. 1997). Our observations suggest that while all particle size spectra can be grouped together over large scales, strong vertical heterogeneity in particle type can exist over smaller scales, emphasizing the importance of differentiating particles by ecological function.

Relationship between size spectral properties and particle concentration

Many recent studies have compared size spectral properties with measures of ecosystem productivity in order to gain a more mechanistic understanding of how increasing productivity affects ecosystem structure and functioning (Ruiz et al. 1996; Franks and Jaffe 2008; Barnes et al. 2011). Although some of these studies have found significant relationships between size spectral slope and phytoplankton biomass or total chlorophyll, the results have been inconsistent. A previous analysis of the FIDO-Φ data from the 2006 cruise revealed that bulk fluorescence or chlorophyll *a* may often not be

representative of phytoplankton concentration, which may be a more ecologically relevant measure of phytoplankton abundance when addressing processes between individuals (Prairie et al. 2010). Thus, we investigated how the fluorescent and scattering particle size spectral slope and intercept changed with fluorescent and scattering particle concentration respectively (Figure 3.13). In addition, we compared fluorescent particle size spectral slope and intercept to bulk fluorescence (Figure 3.14). The size spectral intercept showed a strong positive correlation with both fluorescent and scattering particle concentration; this was expected since the intercept represents the absolute number of particles of the smallest size which should covary with total particle concentration. The size spectral slope showed a weak negative relationship with scattering particle concentration (lower particle concentrations yielded steeper slopes), indicating that in regions with increased total particle abundances, we would expect to find relatively more large particles compared to small particles. There was no significant relationship between size spectral slope and fluorescent particle concentration. However, a weak negative relationship was found between size spectral slope and total bulk fluorescence (Figure 3.14), demonstrating that total fluorescence better explains fluorescent particle size distributions than fluorescent particle concentration. The weak negative relationship between size spectra slope and total bulk fluorescence is consistent with the paradigm that more productive pelagic ecosystems are dominated by larger size classes of phytoplankton (Cushing 1989; Kiørboe 1993). However, Franks and Jaffe (2008) using data from a previous deployment of the FIDO-Φ observed the opposite relationship, with higher chlorophyll *a* being associated with relatively more small particles (steeper size spectral slopes). Since the relationships between size spectral slope

and productivity or phytoplankton abundance reported here and elsewhere in the literature have been incongruous and mostly weak (San Martin et al. 2006; Franks and Jaffe 2008; Barnes et al. 2011), it seems that these indices alone are not a good predictor of how particle size structure varies in the ocean. Thus, it may be important to analyze how productivity interacts with other environmental and biological variables in determining the composition of planktonic communities.

Conclusions

Using data from a novel free-falling planar laser imaging fluorometer (FIDO-Φ), we compared the vertical distribution of fluorescent particles to that of scattering particles. Fluorescent and scattering particles were heterogeneously distributed with frequent meter-scale peaks. At times, fluorescent and scattering particle concentrations were highly correlated, as demonstrated by the occurrence of coincident peaks in the two types of particle concentrations. However, there were several observations of fluorescent and scattering particle concentration peaks that occurred independent from one another, suggesting that the distribution of particles as a whole does not always track fluorescent particle concentration. Comparing the location of scattering particle concentration peaks with buoyancy frequency allowed us to speculate that some of these peaks are composed of non-passive particles (i.e. foraging zooplankton). However, these results emphasize the importance in developing methods to distinguish between the distributions of different particles, since different particle types have vastly different ecological roles. Finally, we analyzed fluorescent and scattering particle size spectra to determine how the size composition of particles varied in relation to total particle concentration and bulk

fluorescence. We observed significant meter-scale variability in the profiles of size spectral slope and intercept, suggesting that phytoplankton and particle composition may often vary significantly with depth. However, only weak relationships were observed between size spectral slope and scattering particle concentration and bulk fluorescence, with no relationship observed between size spectral slope and fluorescent particle concentration. These results in addition to inconsistent conclusions in the literature suggest that phytoplankton abundance alone may not be a good indicator of how size composition varies in the ocean and more multidisciplinary approaches may be needed to understand this phenomenon. This study demonstrates that small-scale vertical variability in phytoplankton distributions can rarely be explained using simple correlations; thus, to understand the dynamics governing this structure, we must consider interacting biological and physical factors.

Acknowledgements

We thank F. Simonet, P. Roberts, and Y. Platoshyn for their help in designing, building, and deploying the free-fall imaging device for observing phytoplankton (FIDO-Φ), and E. Karaköylü and A. Lucas for their help configuring the auxiliary instrumentation. We thank E. Daniels and C. Anderson for the shipboard conductivity-temperature-depth (CTD) deployments and processing chlorophyll samples and H. McClendon for analyzing samples for species composition. This work was supported by the U.S. Office of Naval Research grant N00014-06-1-0304, the National Science Foundation grant OCE 08-25154.

Chapter 3, in part, is currently being prepared for submission for publication of the material. Prairie, J. C., Franks, P. J. S., and Jaffe, J. S. The dissertation author was the primary investigator and author of this paper.

Table 3.1 Correlation coefficients (r^2) for the least square fit for each drop for both the fluorescent and scattering size spectra. The value given is the mean for each drop (+/- the standard deviation).

	Fluorescent particle size spectra	Scattering particle size spectra
Drop 3-1	0.98 (+/- 0.01)	0.98 (+/- 0.01)
Drop 3-2	0.96 (+/- 0.04)	0.97 (+/- 0.02)
Drop 4-1	0.92 (+/- 0.09)	0.98 (+/- 0.01)
Drop 4-2	0.98 (+/- 0.02)	0.99 (+/- 0.01)
Drop 5-1	0.97 (+/- 0.03)	0.98 (+/- 0.01)
Drop 6-1	0.98 (+/- 0.02)	0.98 (+/- 0.01)
Drop 7-1	0.98 (+/- 0.01)	0.98 (+/- 0.01)
Drop 7-2	0.95 (+/- 0.04)	0.97 (+/- 0.02)
Drop 8-2	0.96 (+/- 0.02)	0.97 (+/- 0.01)
Drop 9-2	0.94 (+/- 0.04)	0.99 (+/- 0.01)
Drop 9-3	0.92 (+/- 0.05)	0.99 (+/- 0.01)
Total	0.96 (+/- 0.05)	0.98 (+/- 0.02)

Table 3.2 List of all fluorescent particle concentration peaks identified in each drop. Depth, thickness (defined as the full-width half-peak), density, buoyancy frequency and the mean slope and intercept of the size spectra are described for each peak. Fluorescent particle concentration peaks with no coincident peaks in scattering particle concentration are indicated by asterisks.

Fluorescent particle concentration peaks	Depth (m)	Thickness (m)	Density (kg m^{-3})	Buoyancy frequency (s^{-1})	Mean size spectral slope within peak	Mean size spectral intercept within peak (log_{10} number of particles)
Drop 3-1						
A	18.9	3.49	1025.152	0.0137	0.91	2.27
B	30.0	1.60	1025.318	0.0285	0.82	2.27
Drop 3-2						
A*	15.6	4.54	1025.120	0.0179	0.92	2.24
Drop 4-1						
A	22.2	1.60	1025.370	0.0200	1.09	2.20
B*	27.6	4.75	1025.492	0.0149	0.93	1.98
Drop 4-2						
A*	22.2	3.28	1025.343	0.0203	0.85	2.57
B*	27.3	1.79	1025.499	0.0161	0.82	2.25
C	45.3	2.46	1025.727	0.0113	1.11	1.62
D	52.8	2.22	1025.856	0.0130	1.12	1.39
Drop5-1						
A	29.1	2.36	1025.199	0.0076	0.75	1.68
Drop 6-1						
A	19.5	4.99	1025.118	0.0055	0.86	1.88
B	33.3	4.26	1025.274	0.0172	0.84	1.96
Drop 7-1						
A*	17.7	0.71	1025.092	0.0389	1.12	2.59
B*	22.2	2.47	1025.125	0.0068	0.98	2.59
C	31.8	3.01	1025.257	0.0206	0.81	2.48
D*	39.0	2.26	1025.441	0.0110	0.76	1.95
Drop 7-2						
A*	21	1.45	1025.107	0.0109	1.24	2.88
B	38.4	1.47	1025.483	0.0268	0.97	2.35
Drop 8-2						
No peaks						
Drop 9-2						
No peaks						
Drop 9-3						
A*	20.1	2.99	1025.482	0.0094	1.00	1.65
B*	34.5	4.71	1025.598	0.0051	1.29	1.55

Table 3.3 List of all scattering particle concentration peaks identified in each drop. Depth, thickness (defined as the full-width half-peak), density, buoyancy frequency, and the mean slope and intercept of the size spectra are described for each peak. Scattering particle concentration peaks with no coincident peaks in fluorescent particle concentration are indicated by asterisks.

Scattering particle concentration peaks	Depth (m)	Thickness (m)	Density (kg m^{-3})	Buoyancy frequency (s^{-1})	Mean size spectral slope within peak	Mean size spectral intercept within peak (log_{10} number of particles)
Drop 3-1						
A	17.4	1.90	1025.118	0.0183	1.36	2.94
B	29.7	1.59	1025.306	0.0134	0.84	2.53
Drop 3-2						
A*	24.0	4.23	1025.278	0.0277	0.75	1.82
B*	31.8	1.64	1025.455	0.0173	0.74	1.88
C*	44.7	4.03	10 25.659	0.0085	0.75	1.78
Drop 4-1						
A	22.8	1.26	1025.436	0.0336	0.97	2.10
B*	38.1	2.93	1025.650	0.0136	0.84	1.91
C*	51.0	3.51	1025.828	0.0187	0.82	2.00
D*	58.5	2.47	1025.920	0.0079	0.77	2.14
Drop 4-2						
A	45.3	2.27	1025.727	0.0113	0.85	2.41
B	54.3	4.97	1025.888	0.0194	0.81	2.46
Drop5-1						
A	29.1	2.23	1025.199	0.0076	0.75	1.86
Drop 6-1						
A	19.5	2.25	1025.118	0.0055	0.94	2.20
B	31.2	3.86	1025.232	0.0084	0.95	2.26
Drop 7-1						
A	32.1	2.07	1025.267	0.0252	0.91	2.53
Drop 7-2						
A*	30.3	1.39	1025.336	0.0188	0.77	2.66
B	38.7	2.23	1025.499	0.0247	0.72	2.47
Drop 8-2						
A*	22.2	3.29	1025.341	0.0098	0.81	2.31
B*	39.6	4.00	1025.550	0.0073	0.86	2.55
Drop 9-2						
No peaks						
Drop 9-3						
No peaks						

Table 3.4 Linear least squares fit line for fluorescent particle concentration vs. scattering particle concentration and corresponding correlation coefficient (r^2) for each drop. Asterisks indicate drops with a significant correlation between fluorescent particle concentration and scattering particle concentration ($p < 0.05$).

	Linear least squares fit line	Correlation coefficient (r^2)
Drop 3-1 *	$y = 1.25x + 6.00$	0.16
Drop 3-2	$y = -0.026x + 3.65$	0.005
Drop 4-1	$y = 0.096x + 4.76$	0.02
Drop 4-2 *	$y = 0.21x + 10.88$	0.26
Drop 5-1 *	$y = 1.84x - 0.38$	0.98
Drop 6-1 *	$y = 1.58x + 1.31$	0.43
Drop 7-1 *	$y = 0.12x + 10.46$	0.11
Drop 7-2 *	$y = 0.50x + 15.03$	0.19
Drop 8-2 *	$y = -3.34x + 25.09$	0.03
Drop 9-2 *	$y = -12.25x + 63.73$	0.30
Drop 9-3 *	$y = -25.87x + 118.13$	0.45

Figure 3.1 Drop 3-1. (A) Number of fluorescent particles of a given size (by area) with depth. Colorbar shows number of fluorescent particles in a given size bin on a logarithmic scale. Red line gives the vertical profile of total fluorescent particle concentration. (B) Black line shows the vertical profile of the slope of the size spectra for fluorescent particles. Red line shows the vertical profile of the intercept of the size spectra for fluorescent particles in $\log_{10}$ number of particles. (C) Number of scattering particles of a given size (by area) with depth. Colorbar shows number of scattering particles in a given size bin on a logarithmic scale. Red line gives the vertical profile of total scattering particle concentration. (D) Black line shows the vertical profile of the slope of the size spectra for scattering particles. Red line shows the vertical profile of the intercept of the size spectra for scattering particles in $\log_{10}$ number of particles. (E) Black line shows vertical density profile. Red line shows vertical profile of buoyancy frequency. (F) Log-log plot of fluorescent particle concentration vs. slope of the size spectra for fluorescent particles. Red line is the linear least squares fit of the log-log relationship ($y = -0.13x + 0.034$; $r^2 = 0.08$). (G) Log-log plot of fluorescent particle concentration vs. intercept of the size spectra for fluorescent particles. Red line is the linear least squares fit of the log-log relationship ($y = 0.21x + 0.14$; $r^2 = 0.68$). (H) Log-log plot of scattering particle concentration vs. slope of the size spectra for scattering particles. Red line is the linear least squares fit of the log-log relationship ($y = 0.32x – 0.38$; $r^2 = 0.17$). (I) Log-log plot of scattering particle concentration vs. intercept of the size spectra for scattering particles. Red line is the linear least squares fit of the log-log relationship ($y = 0.31x + 0.017$; $r^2 = 0.78$).

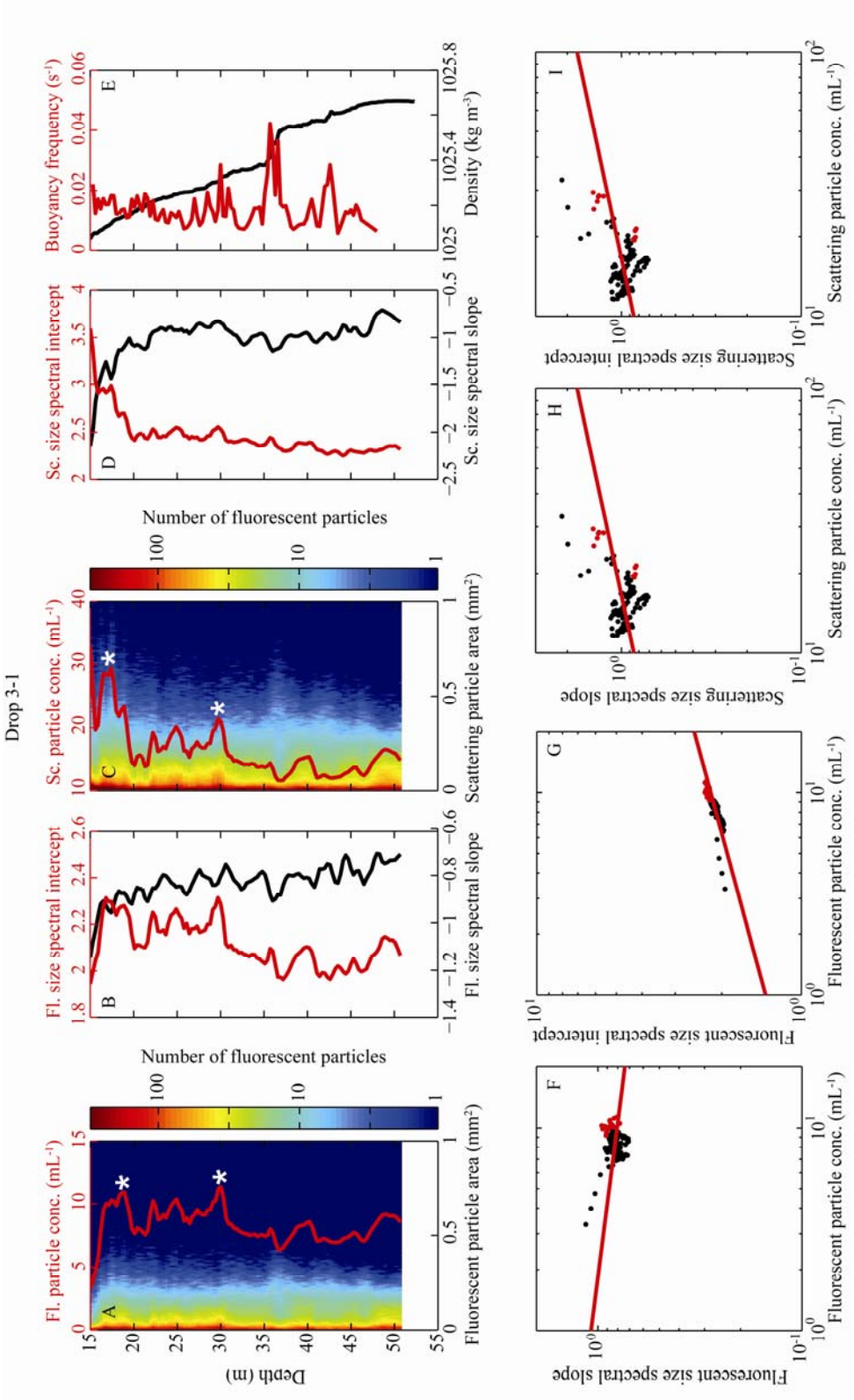
Drop 3-1
Depth (m)
Fl. particle conc. (mL⁻¹)
Fluorescent particle area (mm²)
Number of fluorescent particles
Fl. size spectral intercept
Fl. size spectral slope
Sc. particle conc. (mL⁻¹)
Scattering particle area (mm²)
Number of fluorescent particles
Sc. size spectral intercept
Sc. size spectral slope
Buoyancy frequency (s⁻¹)
Density (kg m⁻³)
Fluorescent size spectral slope
Fluorescent particle conc. (mL⁻¹)
Fluorescent size spectral intercept
Fluorescent particle conc. (mL⁻¹)
Scattering size spectral slope
Scattering particle conc. (mL⁻¹)
Scattering size spectral intercept
Scattering particle conc. (mL⁻¹)

Figure 3.2 Drop 3-2. Legend is the same as for Figure 3.1. (F) The linear least squares fit of the log-log relationship is $y = 0.039x - 0.11$ ($r^2 = 0.04$). (G) The linear least squares fit of the log-log relationship is $y = 0.29x + 0.060$ ($r^2 = 0.95$). (H) The linear least squares fit of the log-log relationship is $y = -0.22x + 0.035$ ($r^2 = 0.67$). (I) The linear least squares fit of the log-log relationship is $y = 0.24x + 0.094$ ($r^2 = 0.96$).

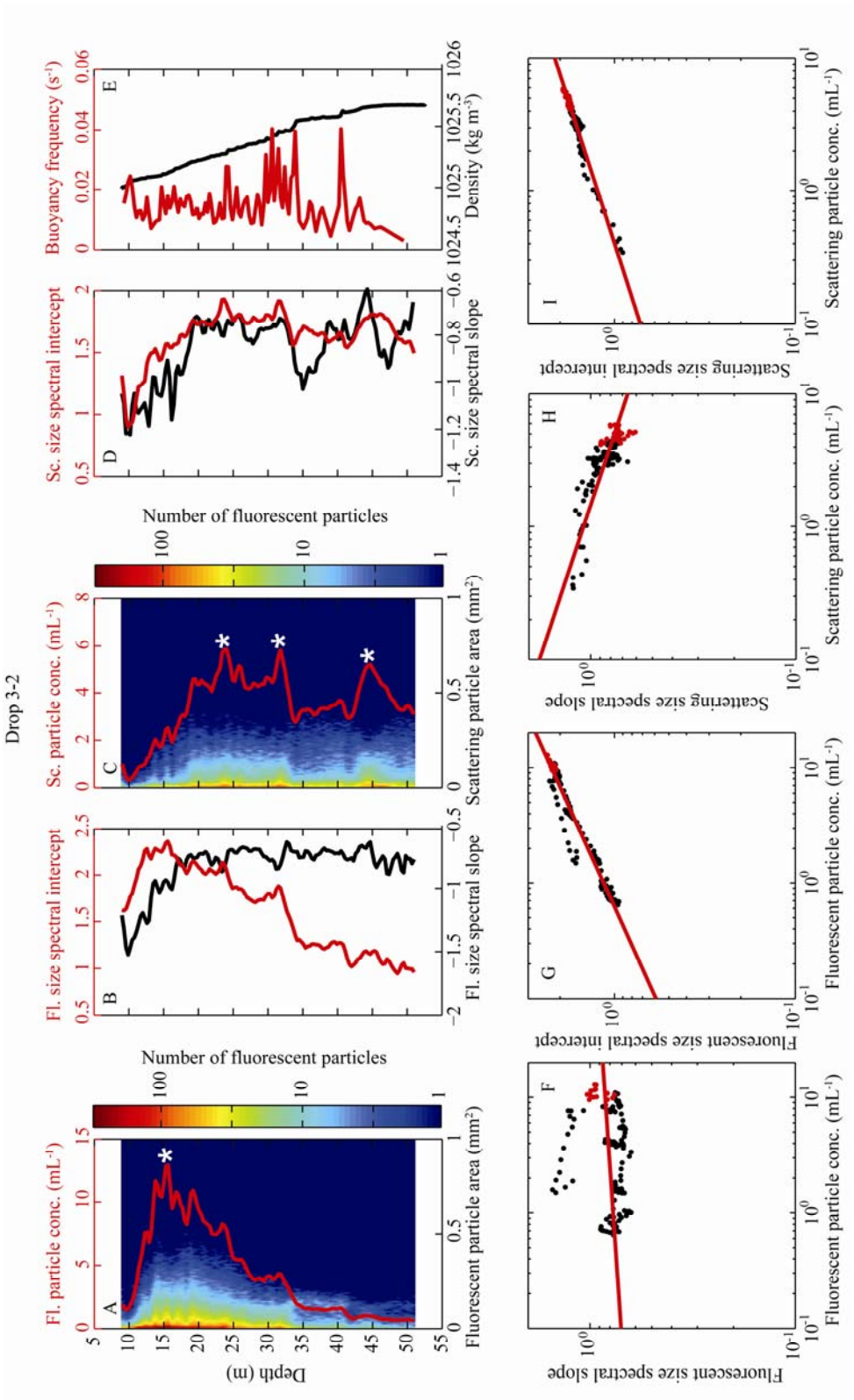
Drop 3-2
Depth (m)
Fl. particle conc. (mL⁻¹)
Fluorescent particle area (mm²)
Number of fluorescent particles
Fl. size spectral intercept
Fl. size spectral slope
Sc. particle conc. (mL⁻¹)
Scattering particle area (mm²)
Sc. size spectral intercept
Sc. size spectral slope
Buoyancy frequency (s⁻¹)
Density (kg m⁻³)
Fluorescent size spectral slope
Fluorescent size spectral intercept
Fluorescent particle conc. (mL⁻¹)
Scattering size spectral slope
Scattering size spectral intercept
Scattering particle conc. (mL⁻¹)
A
B
C
D
E
F
G
H
I

Figure 3.3 Drop 4-1. Legend is the same as for Figure 3.1. The linear least squares fit of the log-log relationship is $y = 0.13x - 0.10$ ($r^2 = 0.39$). (G) The linear least squares fit of the log-log relationship is $y = 0.37x + 0.039$ ($r^2 = 0.96$). (H) The linear least squares fit of the log-log relationship is $y = -0.072x - 0.015$ ($r^2 = 0.04$). (I) The linear least squares fit of the log-log relationship is $y = 0.27x + 0.085$ ($r^2 = 0.94$).

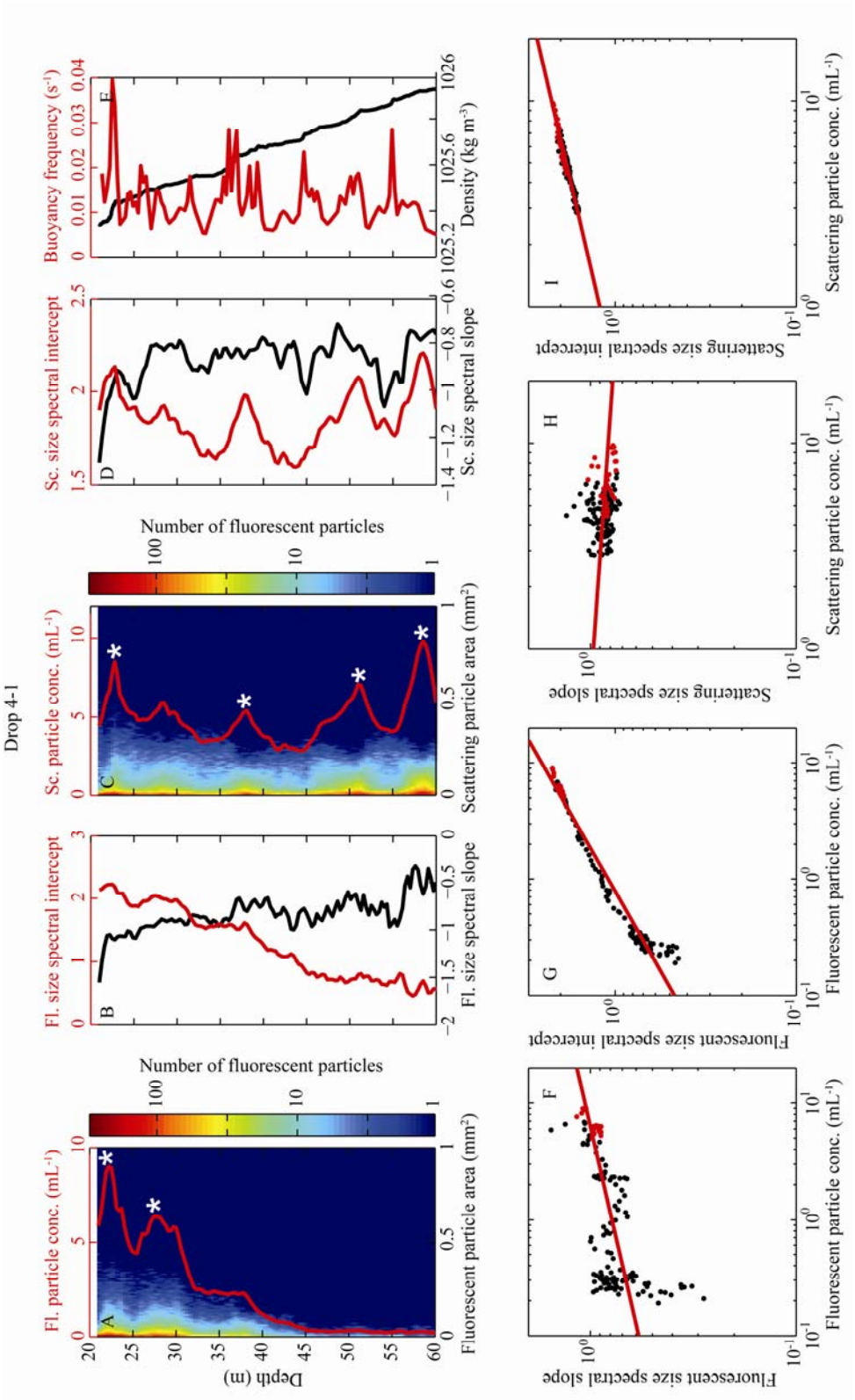
Drop 4-1
Depth (m)
Fl. particle conc. (mL⁻¹)
Fluorescent particle area (mm²)
Number of fluorescent particles
Fl. size spectral intercept
Fl. size spectral slope
Sc. particle conc. (mL⁻¹)
Scattering particle area (mm²)
Number of fluorescent particles
Sc. size spectral intercept
Sc. size spectral slope
Buoyancy frequency (s⁻¹)
Density (kg m⁻³)
Fluorescent size spectral slope
Fluorescent particle conc. (mL⁻¹)
Fluorescent size spectral intercept
Fluorescent particle conc. (mL⁻¹)
Scattering size spectral slope
Scattering particle conc. (mL⁻¹)
Scattering size spectral intercept
Scattering particle conc. (mL⁻¹)

Figure 3.4 Drop 4-2. Legend is the same as for Figure 3.1. The linear least squares fit of the log-log relationship is $y = 0.017x - 0.044$ ($r^2 = 0.03$). (G) The linear least squares fit of the log-log relationship is $y = 0.26x + 0.079$ ($r^2 = 0.95$). (H) The linear least squares fit of the log-log relationship is $y = 0.10x - 0.18$ ($r^2 = 0.10$). (I) The linear least squares fit of the log-log relationship is $y = 0.23x + 0.12$ ($r^2 = 0.95$).

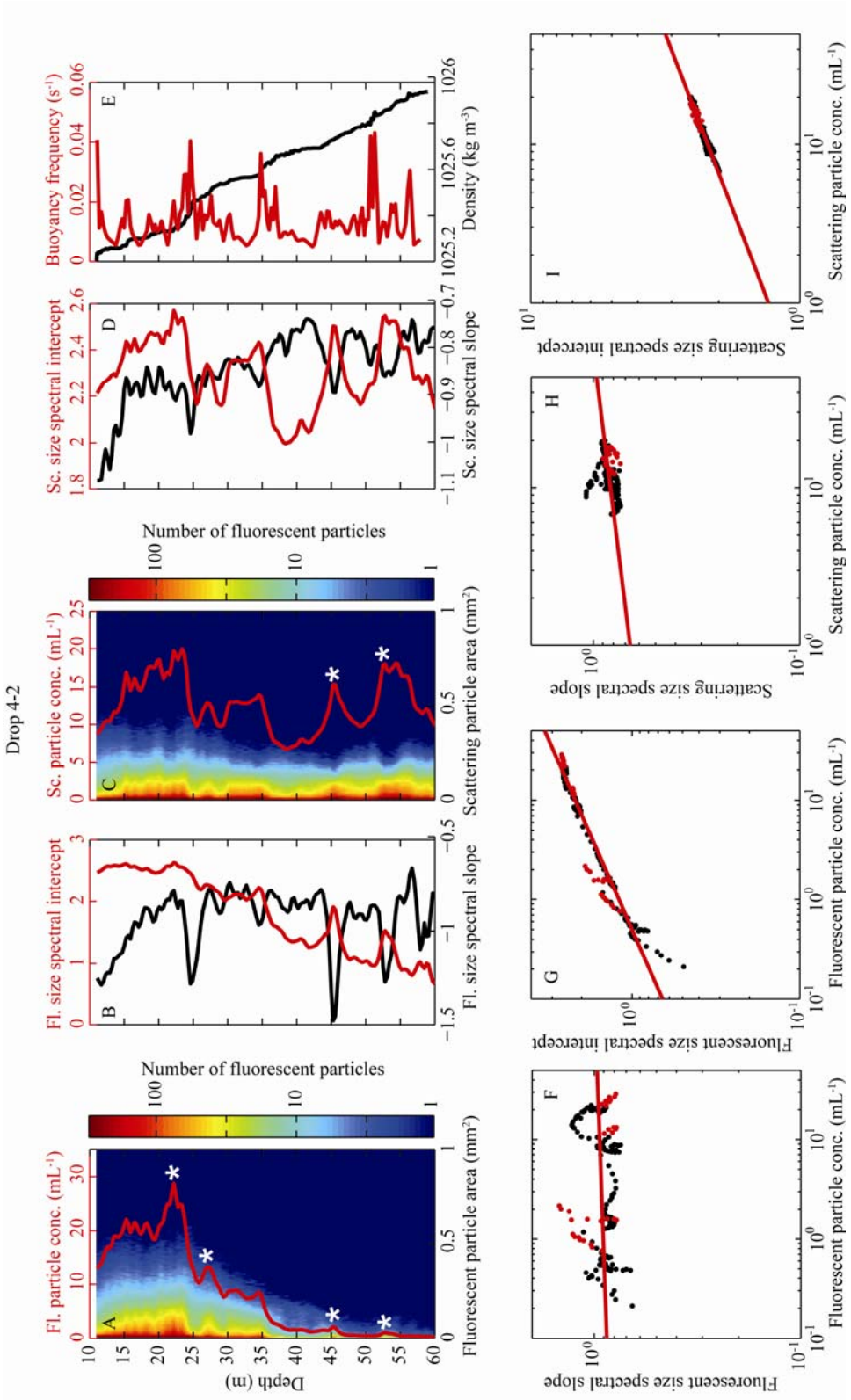
Drop 4-2
Fl. particle conc. (mL⁻¹)
Depth (m)
Fluorescent particle area (mm²)
Number of fluorescent particles
Fl. size spectral intercept
Fl. size spectral slope
Sc. particle conc. (mL⁻¹)
Scattering particle area (mm²)
Number of fluorescent particles
Sc. size spectral intercept
Sc. size spectral slope
Buoyancy frequency (s⁻¹)
Density (kg m⁻³)
Fluorescent size spectral slope
Fluorescent size spectral intercept
Scattering size spectral slope
Scattering size spectral intercept
Fluorescent particle conc. (mL⁻¹)
Scattering particle conc. (mL⁻¹)
A
B
C
D
E
F
G
H
I

Figure 3.5 Drop 5-1. Legend is the same as for Figure 3.1. The linear least squares fit of the log-log relationship is $y = -0.011x - 0.98$ ($r^2 < 0.01$; not significant). (G) The linear least squares fit of the log-log relationship is $y = 0.35x + 0.044$ ($r^2 = 0.91$). (H) The linear least squares fit of the log-log relationship is $y = -0.33x + 0.14$ ($r^2 = 0.66$). (I) The linear least squares fit of the log-log relationship is $y = 0.23x + 0.10$ ($r^2 = 0.90$).

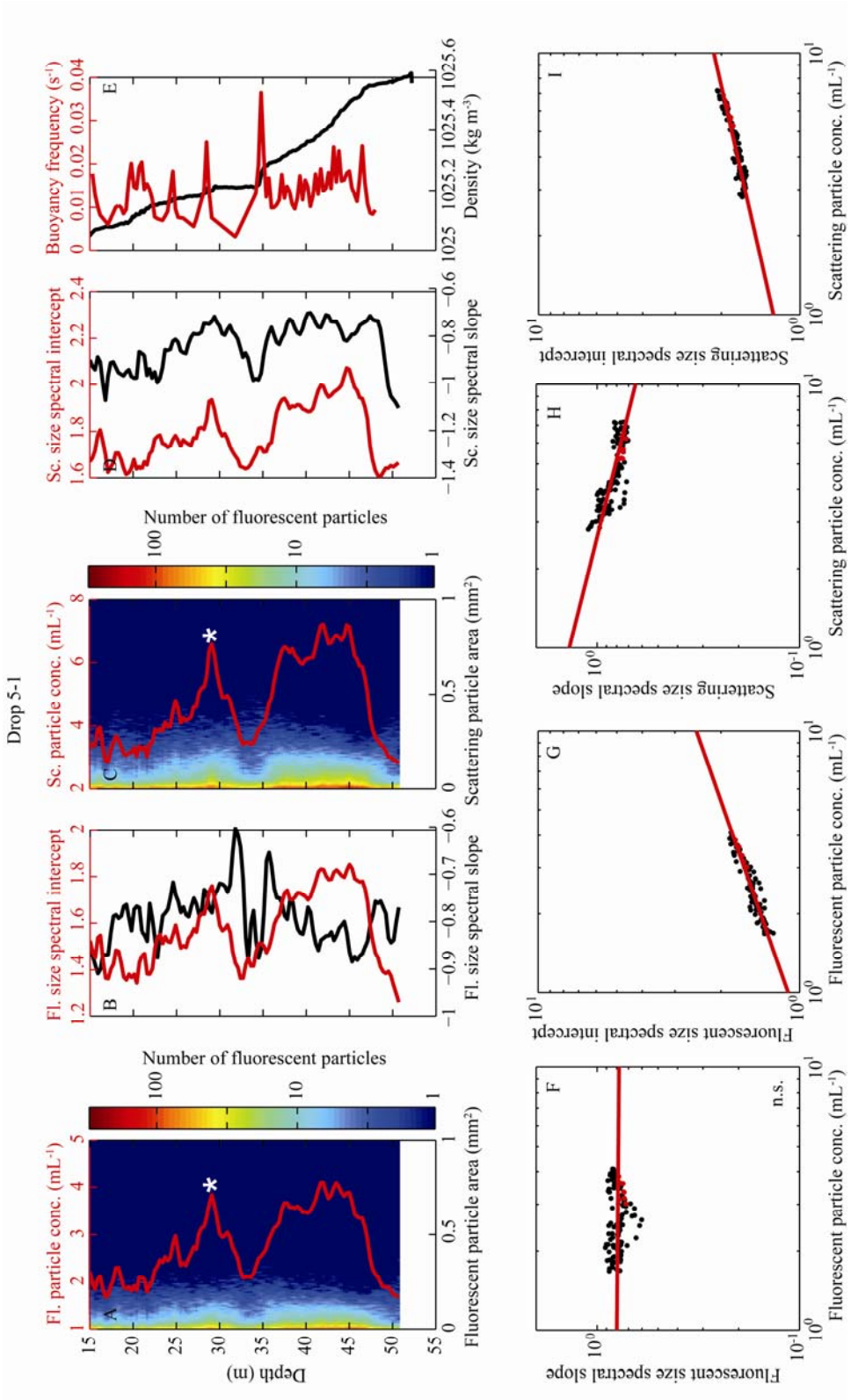
Drop 5-1
Depth (m)
Fl. particle conc. (mL⁻¹)
Fluorescent particle area (mm²)
Number of fluorescent particles
Fl. size spectral intercept
Fl. size spectral slope
Sc. particle conc. (mL⁻¹)
Scattering particle area (mm²)
Sc. size spectral intercept
Sc. size spectral slope
Buoyancy frequency (s⁻¹)
Density (kg m⁻³)
Fluorescent size spectral slope
Fluorescent size spectral intercept
Fluorescent particle conc. (mL⁻¹)
Scattering size spectral slope
Scattering size spectral intercept
Scattering particle conc. (mL⁻¹)
n.s.
A
B
C
D
E
F
G
H
I

Figure 3.6 Drop 6-1. Legend is the same as for Figure 3.1. The linear least squares fit of the log-log relationship is $y = -0.25x + 0.10$ ($r^2 = 0.41$). (G) The linear least squares fit of the log-log relationship is $y = 0.25x + 0.094$ ($r^2 = 0.91$). (H) The linear least squares fit of the log-log relationship is $y = -0.12x + 0.12$ ($r^2 = 0.06$). (I) The linear least squares fit of the log-log relationship is $y = 0.21x + 0.14$ ($r^2 = 0.82$).

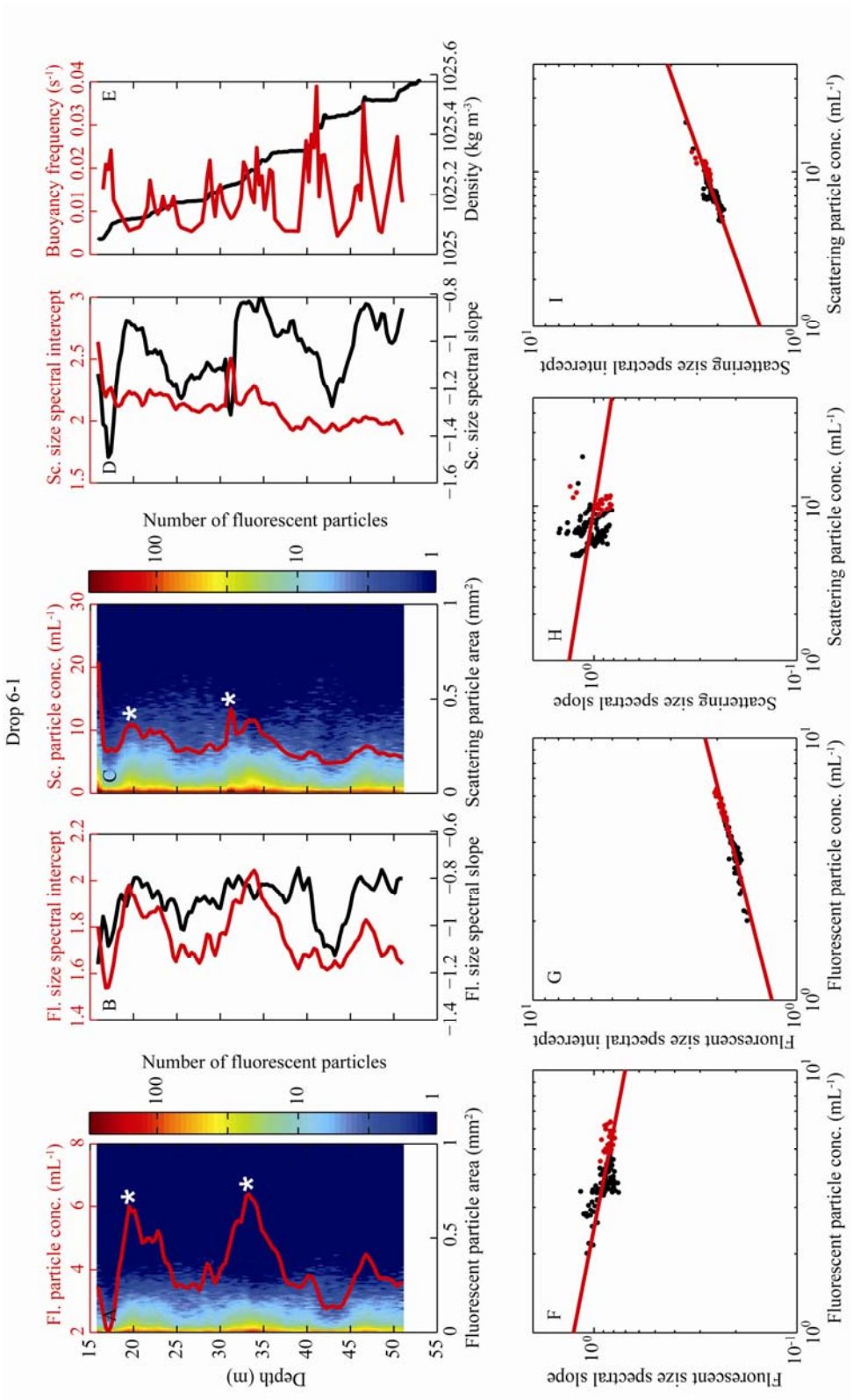
Drop 6-1
Depth (m)
Fl. particle conc. (mL⁻¹)
Fluorescent particle area (mm²)
Number of fluorescent particles
Fl. size spectral intercept
Fl. size spectral slope
Sc. particle conc. (mL⁻¹)
Scattering particle area (mm²)
Sc. size spectral intercept
Sc. size spectral slope
Buoyancy frequency (s⁻¹)
Density (kg m⁻³)
Fluorescent size spectral slope
Fluorescent size spectral intercept
Fluorescent particle conc. (mL⁻¹)
Scattering size spectral slope
Scattering size spectral intercept
Scattering particle conc. (mL⁻¹)
A
B
C
D
E
F
G
H
I

Figure 3.7 Drop 7-1. Legend is the same as for Figure 3.1. The linear least squares fit of the log-log relationship is $y = 0.19x - 0.24$ ($r^2 = 0.41$). (G) The linear least squares fit of the log-log relationship is $y = 0.25x + 0.075$ ($r^2 = 0.95$). (H) The linear least squares fit of the log-log relationship is $y = 0.058x - 0.16$ ($r^2 < 0.01$; not significant). (I) The linear least squares fit of the log-log relationship is $y = 0.25x + 0.074$ ($r^2 = 0.73$).

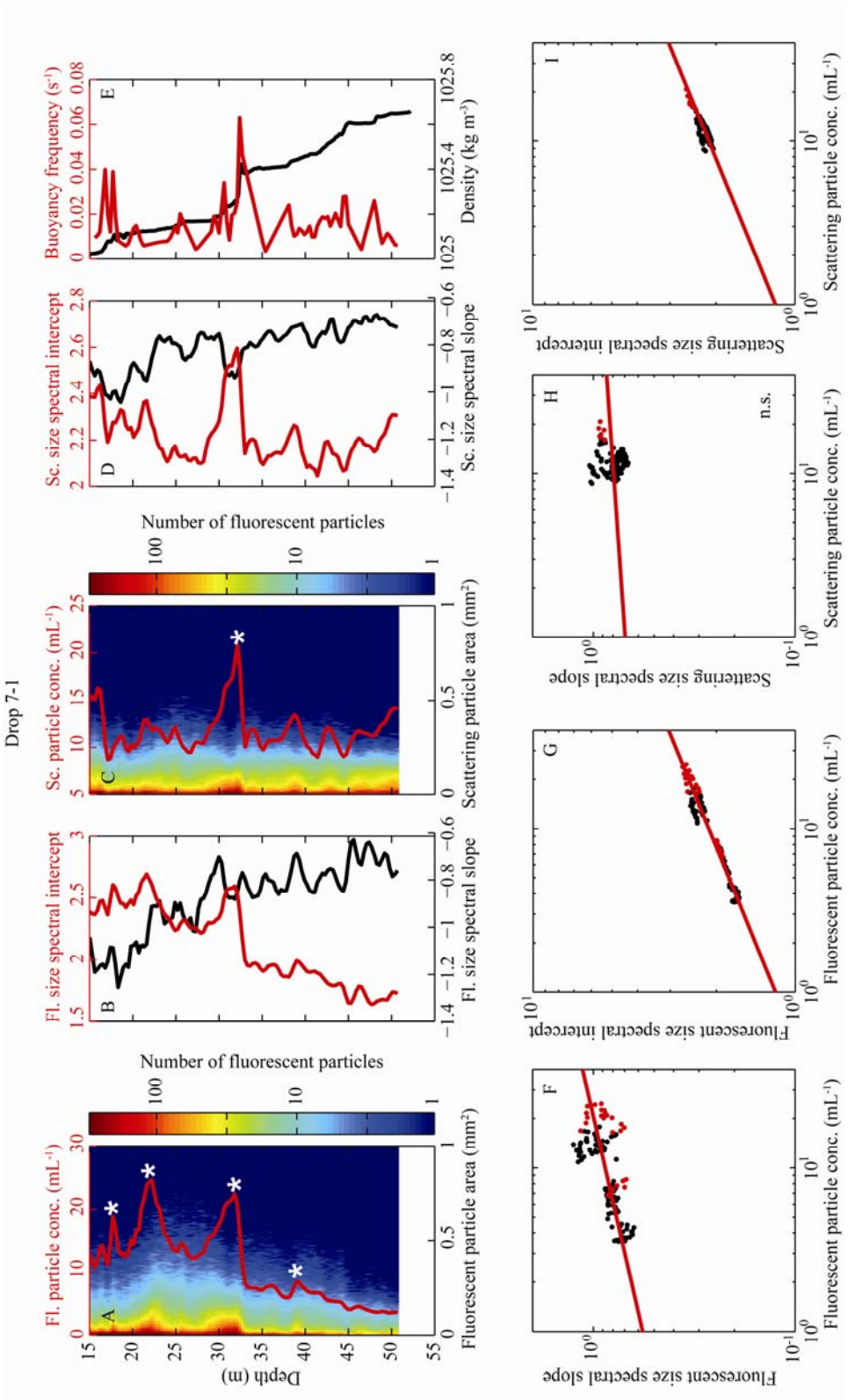
Drop 7-1
Depth (m)
Fl. particle conc. (mL⁻¹)
Fluorescent particle area (mm²)
Number of fluorescent particles
Fl. size spectral intercept
Fl. size spectral slope
Sc. particle conc. (mL⁻¹)
Scattering particle area (mm²)
Number of fluorescent particles
Sc. size spectral intercept
Sc. size spectral slope
Buoyancy frequency (s⁻¹)
Density (kg m⁻³)
A
B
C
D
E
F
G
H
I
n.s.
Fluorescent size spectral slope
Fluorescent particle conc. (mL⁻¹)
Fluorescent size spectral intercept
Fluorescent particle conc. (mL⁻¹)
Scattering size spectral slope
Scattering particle conc. (mL⁻¹)
Scattering size spectral intercept
Scattering particle conc. (mL⁻¹)

Figure 3.8 Drop 7-2. Legend is the same as for Figure 3.1. The linear least squares fit of the log-log relationship is $y = 0.13x - 0.12$ ($r^2 = 0.20$). (G) The linear least squares fit of the log-log relationship is $y = 0.23x + 0.10$ ($r^2 = 0.94$). (H) The linear least squares fit of the log-log relationship is $y = 0.41x - 0.62$ ($r^2 = 0.54$). (I) The linear least squares fit of the log-log relationship is $y = 0.25x + 0.063$ ($r^2 = 0.97$).

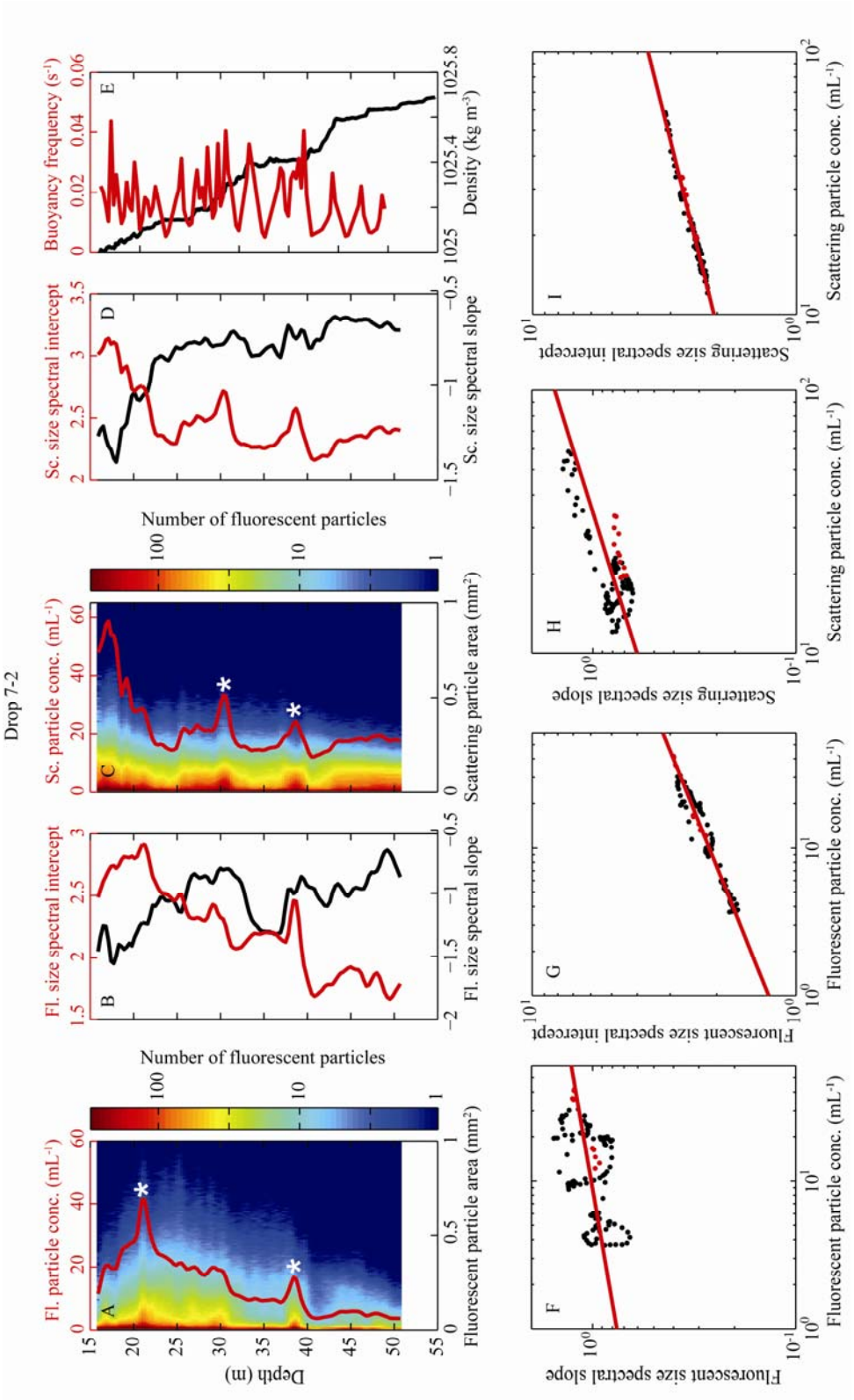
Drop 7-2
Depth (m)
Fl. particle conc. (mL⁻¹)
Fluorescent particle area (mm²)
Number of fluorescent particles
Fl. size spectral intercept
Fl. size spectral slope
Sc. particle conc. (mL⁻¹)
Scattering particle area (mm²)
Sc. size spectral intercept
Sc. size spectral slope
Buoyancy frequency (s⁻¹)
Density (kg m⁻³)
Fluorescent size spectral slope
Fluorescent size spectral intercept
Fluorescent particle conc. (mL⁻¹)
Scattering size spectral slope
Scattering size spectral intercept
Scattering particle conc. (mL⁻¹)
A
B
C
D
E
F
G
H
I

Figure 3.9 Drop 8-2. Legend is the same as for Figure 3.1. The linear least squares fit of the log-log relationship is $y = -0.53x + 0.21$ ($r^2 = 0.19$). (G) The linear least squares fit of the log-log relationship is $y = 0.15x + 0.13$ ($r^2 = 0.12$). (H) The linear least squares fit of the log-log relationship is $y = -0.0096x - 0.0094$ ($r^2 < 0.01$; not significant). (I) The linear least squares fit of the log-log relationship is $y = 0.18x + 0.15$ ($r^2 = 0.91$).

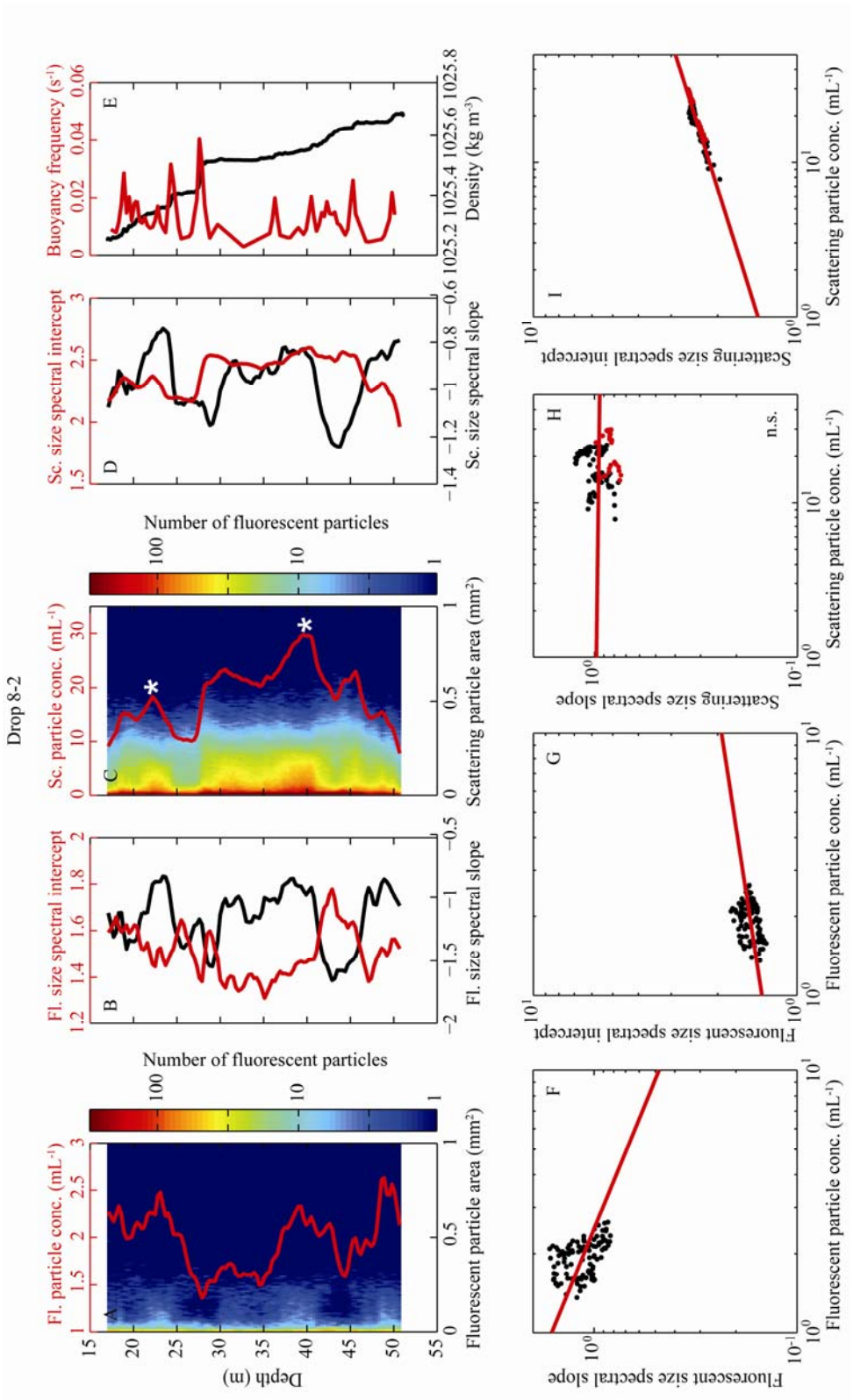
Drop 8-2
Depth (m)
Fl. particle conc. (mL⁻¹)
Fluorescent particle area (mm²)
Number of fluorescent particles
Fl. size spectral intercept
Fl. size spectral slope
Sc. particle conc. (mL⁻¹)
Scattering particle area (mm²)
Number of fluorescent particles
Sc. size spectral intercept
Sc. size spectral slope
Buoyancy frequency (s⁻¹)
Density (kg m⁻³)
A
B
C
D
E
F
G
H
I
n.s.
Fluorescent particle conc. (mL⁻¹)
Fluorescent size spectral slope
Fluorescent size spectral intercept
Scattering particle conc. (mL⁻¹)
Scattering size spectral slope
Scattering size spectral intercept

Figure 3.10 Drop 9-2. Legend is the same as for Figure 3.1. The linear least squares fit of the log-log relationship is $y = -0.024x + 0.028$ ($r^2 = 0.02$; not significant). (G) The linear least squares fit of the log-log relationship is $y = 0.27x + 0.12$ ($r^2 = 0.92$). (H) The linear least squares fit of the log-log relationship is $y = -0.11x + 0.11$ ($r^2 = 0.74$). (I) The linear least squares fit of the log-log relationship is $y = 0.17x + 0.17$ ($r^2 > 0.99$).

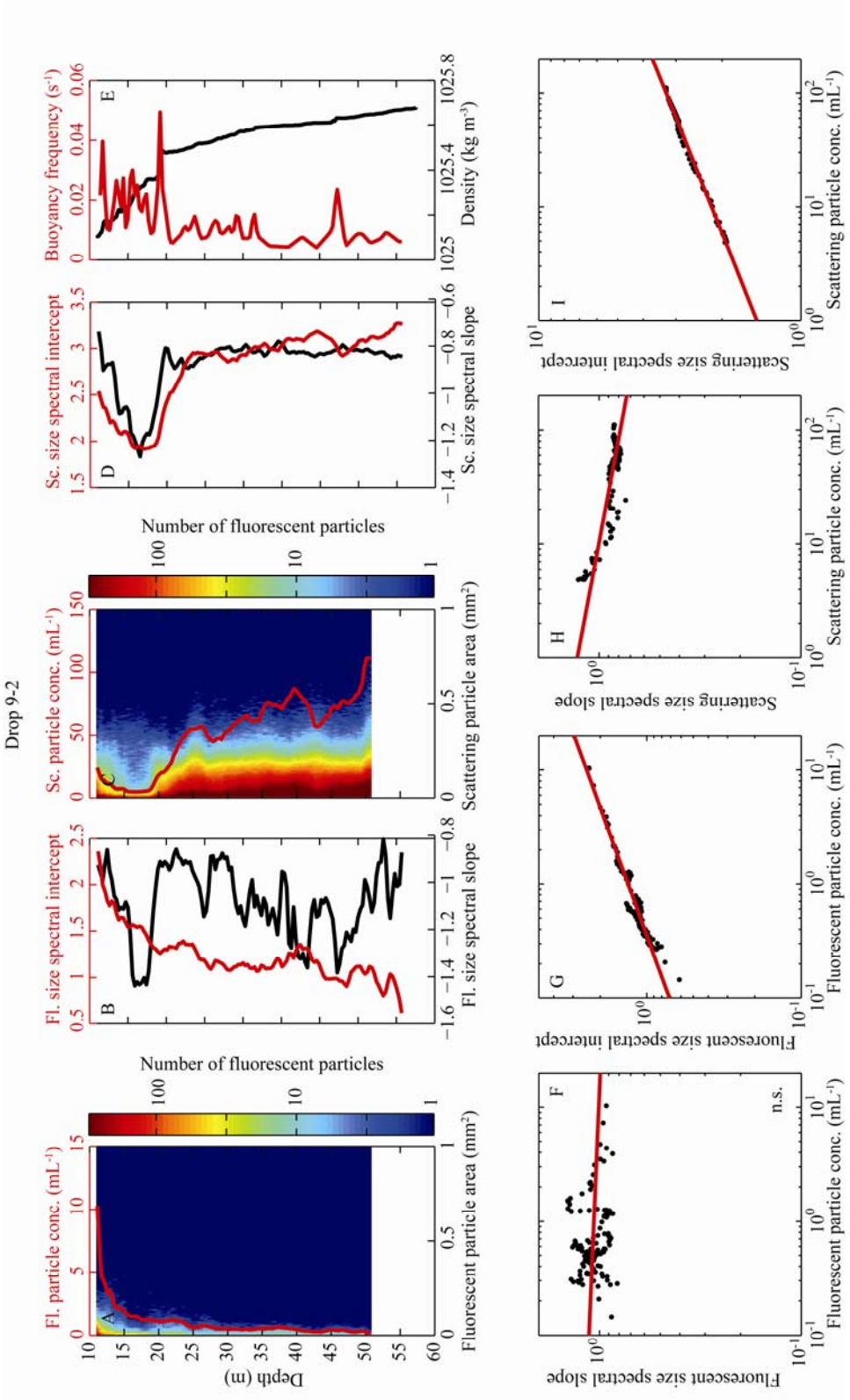
Drop 9-2
Depth (m)
Fl. particle conc. (mL⁻¹)
Fluorescent particle area (mm²)
Number of fluorescent particles
Fl. size spectral intercept
Fl. size spectral slope
Sc. particle conc. (mL⁻¹)
Scattering particle area (mm²)
Number of fluorescent particles
Sc. size spectral intercept
Sc. size spectral slope
Buoyancy frequency (s⁻¹)
Density (kg m⁻³)
Fluorescent size spectral slope
Fluorescent particle conc. (mL⁻¹)
n.s.
Fluorescent size spectral intercept
Fluorescent particle conc. (mL⁻¹)
Scattering size spectral slope
Scattering particle conc. (mL⁻¹)
Scattering size spectral intercept
Scattering particle conc. (mL⁻¹)

Figure 3.11 Drop 9-3. Legend is the same as for Figure 3.1. The linear least squares fit of the log-log relationship is $y = -0.091x + 0.028$ ($r^2 = 0.14$). (G) The linear least squares fit of the log-log relationship is $y = 0.23x + 0.14$ ($r^2 = 0.79$). (H) The linear least squares fit of the log-log relationship is $y = 0.0010x - 0.060$ ($r^2 < 0.01$; not significant). (I) The linear least squares fit of the log-log relationship is $y = 0.17x + 0.17$ ($r^2 > 0.99$).

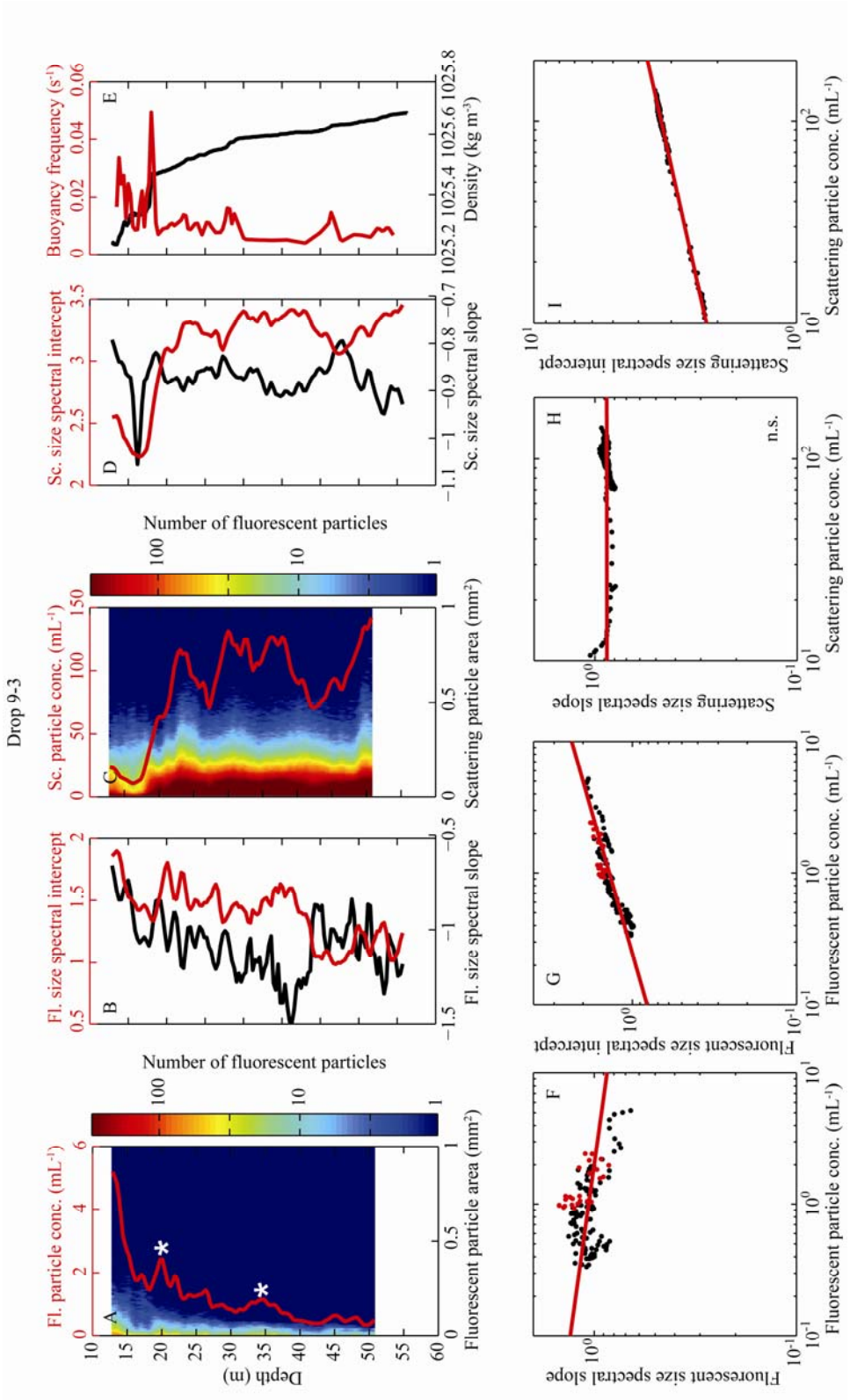
Drop 9-3
Depth (m)
Fl. particle conc. (mL⁻¹)
Fluorescent particle area (mm²)
Number of fluorescent particles
Fl. size spectral intercept
Fl. size spectral slope
Sc. particle conc. (mL⁻¹)
Scattering particle area (mm²)
Number of fluorescent particles
Sc. size spectral intercept
Sc. size spectral slope
Buoyancy frequency (s⁻¹)
Density (kg m⁻³)
A
B
C
D
E
F
G
H
I
Fluorescent size spectral slope
Fluorescent particle conc. (mL⁻¹)
Fluorescent size spectral intercept
Fluorescent particle conc. (mL⁻¹)
Scattering size spectral slope
Scattering particle conc. (mL⁻¹)
n.s.
Scattering size spectral intercept
Scattering particle conc. (mL⁻¹)

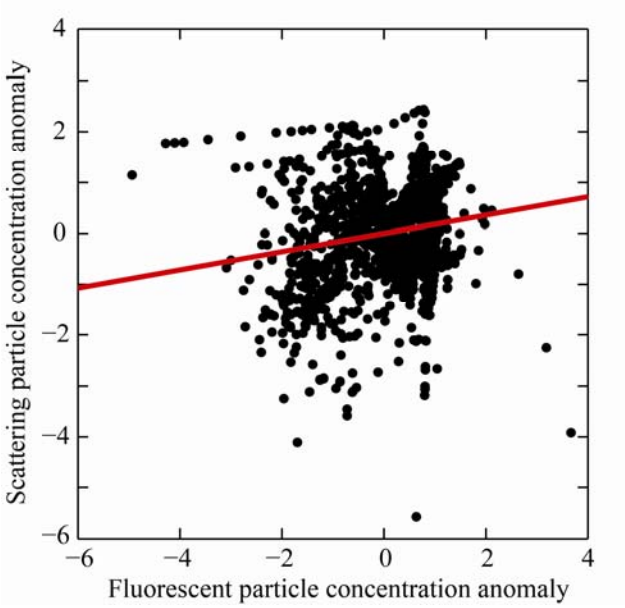

Figure 3.12 Plot of fluorescent particle concentration anomaly vs. scattering particle concentration anomaly for all drops. Red line is the linear least squares fit ($y = 0.18x + 9.6\text{x}10^{-17}$; $r^2 = 0.03$).

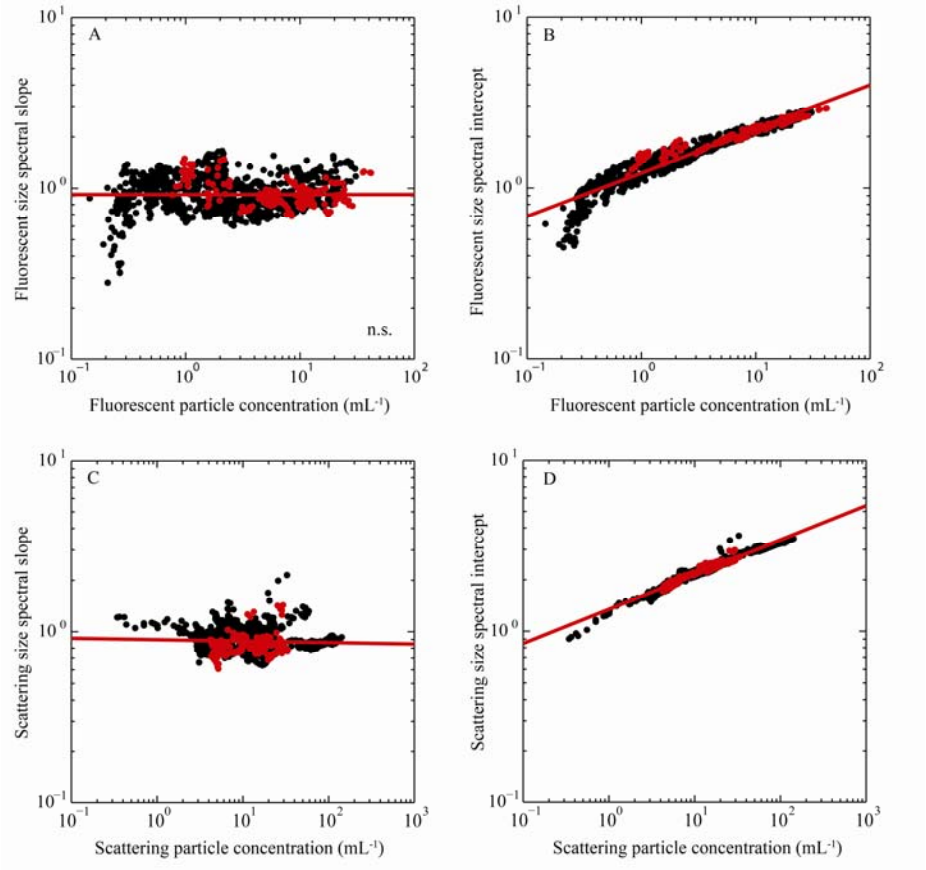

Figure 3.13 Plots of size spectral properties vs. fluorescent and scattering particle concentration for all drops of the FIDO-Φ. (A) Log-log plot of fluorescent particle concentration vs. slope of the size spectra for scattering particles. Red line is the linear least squares fit ($y = -3.26\text{x}10^{-5}x - 0.037$; $r^2 < 0.01$). (B) Log-log plot of fluorescent particle concentration vs. intercept of the size spectra ($\log_{10}$ number of particles) for fluorescent particles. Red line is the linear least squares fit ($y = 0.26x + 0.088$; $r^2 = 0.91$). (C) Log-log plot of scattering particle concentration vs. slope of the size spectra for scattering particles. Red line is the linear least squares fit ($y = -0.0084x - 0.047$; $r^2 < 0.01$). (D) Log-log plot of scattering particle concentration vs. intercept of the size spectra ($\log_{10}$ number of particles) for scattering particles. Red line is the linear least squares fit ($y = 0.20x + 0.13$; $r^2 = 0.97$).

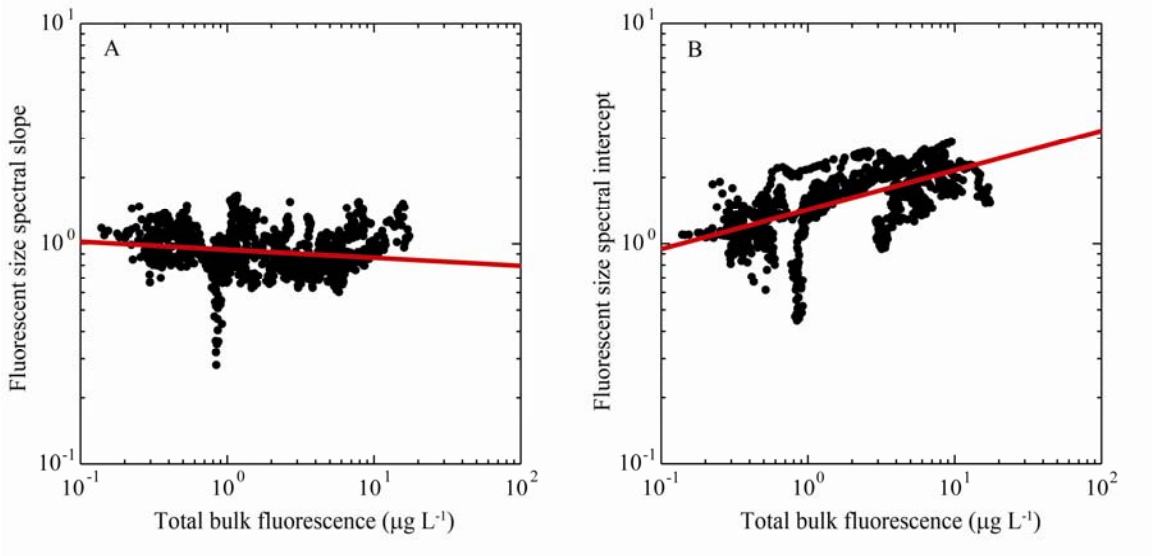

Figure 3.14 Plots of size spectral properties vs. total bulk fluorescence for all drops of the FIDO-Φ. (A) Log-log plot of total bulk fluorescence vs. slope of the size spectra for scattering particles. Red line is the linear least squares fit (y = -0.036x – 0.026; r^2 = 0.03). (B) Log-log plot of total bulk fluorescence vs. intercept of the size spectra ($\log_{10}$ number of particles) for fluorescent particles. Red line is the linear least squares fit (y = 0.18x + 0.15; r^2 = 0.35).

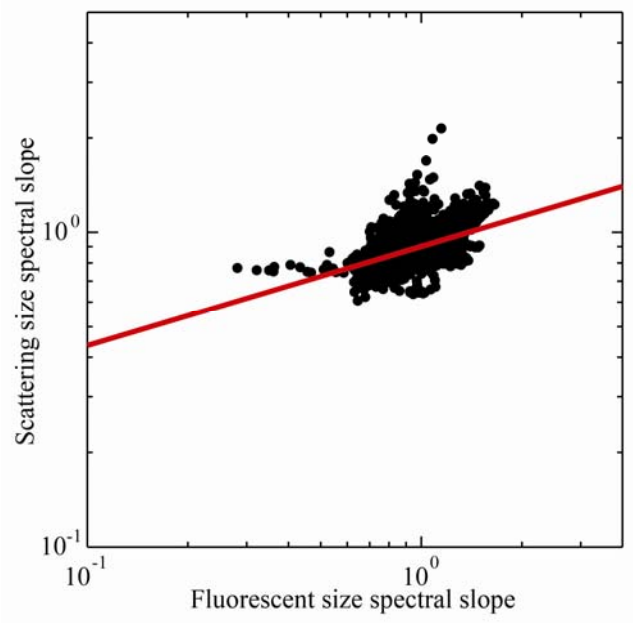

Figure 3.15 Plot of fluorescent particle spectral slope vs. scattering particle spectral slope for all drops. Red line is the linear least squares fit ($y = 0.32x - 0.045$; $r^2 = 0.20$).

References

Alldredge, A. L., T. J. Cowles, S. MacIntyre, J. E. B. Rines, P. L. Donaghay, C. F. Greenlaw, D. V. Holliday, M. M. Dekshenieks, J. M. Sullivan, J. R. V. Zaneveld. 2002. Occurrence and mechanisms of formation of a dramatic thin layer of marine snow in a shallow Pacific fjord. Marine Ecology Progress Series **233**: 1-12.

Barnes, C., X. Irigoien, J. A. A. De Oliveira, D. Maxwell, and S. Jennings. 2011. Predicting marine phytoplankton community size structure from empirical relationships with remotely sensed variables. Journal of Plankton Research **33**: 13-24.

Benoit-Bird, K. J., T. J. Cowles, and C. E. Wingard. 2009. Edge gradients provide evidence of ecological interactions in planktonic thin layers. Limnology and Oceanography **54**: 1382-1392.

Birch, D. A., W. R. Young, and P. J. S. Franks. 2008. Thin layers of plankton: Formation by shear and death by diffusion. Deep-Sea Research Part I **55**: 277-295.

Checkley, D. M., R. E. Davis, A. W. Herman, G. A. Jackson, B. Beanlands, and L. A. Regier. 2008. Assessing plankton and other particles in situ with the SOLOPC. Limnology and Oceanography **53**: 2123-2136.

Cheriton, O. M., M. A. McManus, M. T. Stacey, and J. V. Steinbuck. 2009. Physical and biological controls on the maintenance and dissipation of a thin phytoplankton layer. Marine Ecology Progress Series 378: 55-69.

Cowles, T. J., R. A. Desiderio, and M. Carr. 1998. Small-scale planktonic structure: persistence and trophic consequences. Oceanography **11**:4-9.

Cushing, D. H. 1989. A difference in structure between ecosystems in strongly stratified waters and in those that are only weakly stratified. Journal of Plankton Research **11**: 1-13.

Davis, C. S., G. R. Flierl, P. H. Wiebe, and P. J. S. Franks. 1991. Micropatchiness, turbulence, and recruitment in plankton. Journal of Marine Research **49**: 109-151.

Dekshenieks, M. M., P. L. Donaghay, J. M. Sullivan, J. E. B. Rines, T. R. Osborn, and M. S. Twardowski. 2001. Temporal and spatial occurrence of thin phytoplankton layers in relation to physical processes. Marine Ecology Progress Series **223**: 61-71.

Derenbach, J. B., H. Astheimer, H. P. Hansen, and H. Leach. 1979. Vertical microscale distribution of phytoplankton in relation to the thermocline. Marine Ecology Progress Series **1**: 187-193.

Duda, T. F., and C. R. Rehmann. 2002. Systematic microstructure variability in double-diffusively stable coastal waters of nonuniform density gradient. Journal of Geophysical Research 107: 3144, doi:10.1029/2001JC000844.

Franks, P. J. S. 1995. Thin layers of phytoplankton: a model of formation by near-inertial wave shear. Deep-Sea Research I **42**: 75-91.

Franks, P. J. S. and J. S. Jaffe. 2001. Microscale distributions of phytoplankton: initial results from a two-dimensional imaging fluorometer, OSST. Marine Ecology Progress Series **220**: 59-72.

Franks, P. J. S., and J. S. Jaffe. 2008. Microscale variability in the distributions of large fluorescent particles observed *in situ* with a planar laser imaging fluorometer. Journal of Marine Systems **69**: 254-270, doi:10.1016/j.jmarsys.2006.03.027.

Gorsky, G., M. Picheral, and L. Stemmann. 2000. Use of the underwater video profiler for the study of aggregate dynamics in the North Mediterranean. Estuarine, Coastal and Shelf Science **50**: 121-128.

Holliday, D. V., P. L. Donaghay, C. F. Greenlaw, D. E. McGehee, M. A. McManus, J. M. Sullivan, and J. L. Miksis. 2003. Advances in defining fine- and micro-scale pattern in marine plankton. Aquatic Living Resources 16: 131-136.

Jackson, G. A. 1990. A model of the formation of marine algal flocs by physical coagulation processes. Deep-Sea Research **37**: 1197-1211.

Jackson, G. A., R. Maffione, D. K. Costello, A. L. Alldredge, B. E. Logan, and H. G. Dam. 1997. Particle size spectra between 1 μm and 1 cm at Monterey Bay determined using multiple instruments. Deep-Sea Research I **44**: 1739-1767.

Jaffe, J. S., P. J. S. Franks, and A. W. Leising. 1998. Simultaneous imaging of phytoplankton and zooplankton distributions. Oceanography **11**: 24-29.

Kiørboe, T. 1993. Turbulence, phytoplankton cell size, and the structure of pelagic food webs. Advances in Marine Biology **29**: 1-72.

Kiørboe, T. 1997. Small-scale turbulence, marine snow formation, and planktivorous feeding. Scientia Marina **61**: 141-158.

Leising, A. W., and P. J. S. Franks. 2000. Copepod vertical distribution within a spatially variable food source: a simple foraging-strategy model. Journal of Plankton Research **22**: 999-1024.

Marañón, E., P. Cermeño, J. Rodríguez, M. V. Zubkov, and R. P. Harris. 2007. Scaling of phytoplankton photosynthesis and cell size in the ocean. Limnology and Oceanography **52**: 2190-2198.

McDonnell, A. M. P., and K. O. Buesseler. 2010. Variability in the average sinking velocity of marine particles. Limnology and Oceanography **55**: 2085-2096.

McManus, M. A., A. L. Alldredge, A. H. Barnard, E. Boss, J. F. Case, T. J. Cowles, P. L. Donaghay, L. B. Eisner, D. J. Gifford, C. F. Greenlaw, C. M. Herren, D. V. Holliday, D. Johnson, S. MacIntyre, D. M. McGehee, T. R. Osborn, M. J. Perry, R. E. Pieper, J. E. B. Rines, D. C. Smith, J. M. Sullivan, M. K. Talbot, M. S. Twardowski, A. Weidemann, and J. R. Zaneveld. 2003. Characteristics, distribution and persistence of thin layers over a 48 hour period. Marine Ecology Progress Series **261**: 1-19.

Menden-Deuer, S. 2008. Spatial and temporal characteristics of plankton-rich layers in a shallow, temperate fjord. Marine Ecology Progress Series **355**: 21-30.

Menden-Deuer, S. and D. Grünbaum. 2006. Individual foraging behaviors and population distributions of a planktonic predator aggregating to planktonic thin layers. Limnology and Oceanography **51**: 109-116.

Menden-Deuer, S. and K. Fredrickson. 2010. Structure-dependent, protistan grazing and its implication for the formation, maintenance and decline of phytoplankton patches. Marine Ecology Progress Series **420**: 57-71.

Picheral, M., L. Guidi, L. Stemmann, D. M. Karl, G. Iddaoud, and G. Gorsky. 2010. The Underwater Vision Profiler 5: an advanced instrument for high spatial resolution studies of particle size spectra and zooplankton. Limnology and Oceanography: Methods **8**: 462-473.

Prairie, J. C., P. J. S. Franks, and J. S. Jaffe. 2010. Cryptic peaks: invisible vertical structure in fluorescent particles revealed using a planar laser imaging fluorometer. Limnology and Oceanography **55**: 1943-1958.

Prairie, J. C., P. J. S. Franks, J. S. Jaffe, M. J. Doubell, and H. Yamazaki. in press. Physical and biological controls of vertical gradients in phytoplankton. Limnology and Oceanography: Fluids and Environments.

Rines, J. E. B., P. L. Donaghay, M. M. Dekshenieks, J. M. Sullivan, and M. S. Twardowski. 2002. Thin layers and camouflage: hidden *Pseudo-nitzschia* spp. (Bacillariophyceae) populations in a fjord in the San Juan Islands, Washington, USA. Marine Ecology Progress Series **225**: 123-137.

Ruiz, J., C. M. García, and J. Rodríguez. 1996. Vertical patterns of phytoplankton size distribution in the Cantabric and Balearic Seas. Journal of Marine Systems **9**: 269-282.

Ryan, J. P., M. A. McManus, J. D. Paduan, and F. P. Chavez. 2008. Phytoplankton thin layers caused by shear in frontal zones of a coastal upwelling system. Marine Ecology Progress Series 354: 21-34.

Ryan, J. P., M. A. McManus, and J. M. Sullivan. 2010. Interacting physical, chemical and biological forcing of phytoplankton thin-layer variability in Monterey Bay, California. Continental Shelf Research **30**: 7-16.

San Martin, E., R. P. Harris, and X. Irigoien. 2006. Latitudinal variation in plankton size spectra in the Atlantic Ocean. Deep-Sea Research II **53**: 1560-1572.

Shanks, A. L., and J. D. Trent. 1980. Marine snow: sinking rates and potential role in vertical flux. Deep-Sea Research **27A**: 137-143.

Sheldon, R. W., A. Prakash, and W. H. Sutcliffe, Jr. 1972. The size distribution of particles in the ocean. Limnology and Oceanography **17**: 327-340.

Stacey, M. T., M. A. McManus, and J. V. Steinbuck. 2007. Convergences and divergences and thin layer formation and maintenance. Limnology and Oceanography **52**: 1523-1532.

Steinbuck, J. V., M. T. Stacey, M. A. McManus, O. M. Cheriton, and J. P. Ryan. 2009. Observations of turbulent mixing in a phytoplankton thin layer: Implications for formation, maintenance, and breakdown. Limnology and Oceanography **54**: 1353-1368.

Sullivan, J. M., P. L. Donaghay, and J. E. B. Rines. 2010. Coastal thin layer dynamics: consequences to biology and optics. Continental Shelf Research **30**: 50-65.

Tiselius, P. 1992. Behavior of *Acartia tonsa* in patchy food environments. Limnology and Oceanography **37**: 1640-1651.

Zawada, D. G. 2002. The Application of a Novel Multispectral Imaging System to the *in vivo* Study of Fluorescent Compounds in Selected Marine Organisms. PhD thesis, University of California, San Diego, CA.

Zhou, M., and M. E. Huntley. 1997. Population dynamics theory of plankton based on biomass spectra. Marine Ecology Progress Series **159**: 61-73.

CHAPTER IV.

PHYSICAL AND BIOLOGICAL CONTROLS OF VERTICAL GRADIENTS IN PHYTOPLANKTON

Abstract

Small-scale vertical heterogeneity in phytoplankton distributions is common in coastal waters, and may be a critical feature influencing trophic coupling in planktonic systems. Here we develop a model to investigate the biological and physical dynamics that control vertical gradients in phytoplankton abundance. The model includes phytoplankton layer formation and layer destruction through mixing, and predicts that the local maximum scaled phytoplankton gradient is controlled by the relative strengths of these dynamics. We compare the predictions of this model to highly resolved profiles of phytoplankton concentration and fluorescence collected using a free-falling planar laser imaging fluorometer (FIDO-Φ) and turbulence microstructure profiler data (TurboMAP-L). From these profiles we estimate the model parameters: the maximum rate of layer formation and minimum possible layer thickness. The maximum rate of layer formation ranged from 0.46 - 0.94 d^{-1}, which is comparable to maximum reported growth rates of the most common phytoplankton taxa found in our samples. The minimum layer thickness estimated from our data suggested that persistent phytoplankton layers thinner than ~0.5 m may be rare in coastal waters. This study provides a mechanistic explanation for some of the underlying dynamics governing phytoplankton layer formation, maintenance, and destruction, and will allow us to better predict the magnitude and occurrence of these ecologically important structures in the field.

Introduction

Thin layers of increased fluorescence and phytoplankton concentration on the scale of meters or less have been shown to be common features in coastal waters (e.g., McManus et al. 2003; Sullivan et al. 2005; Doubell et al. 2006). The increased abundance of phytoplankton in thin layers causes many ecological processes to occur at disproportionately high rates compared to background conditions, such as aggregate formation, zooplankton foraging, infection, and sex (e.g., Alldredge et al. 2002; McManus et al. 2003). Thus, understanding the physical and biological processes that drive the formation and maintenance of these layers is fundamental to our understanding of ecosystem dynamics in planktonic systems.

Small-scale vertical structures in plankton distributions have frequently been linked to variations in physical variables (Desiderio et al. 1993; Cowles et al 1998; Yamazaki et al. 2006). For example, phytoplankton layers are often associated with sharp density gradients, representing stable regions of the water column where layers are more easily maintained (McManus et al. 2003; Steinbuck et al. 2009; Prairie et al. 2010). Field sampling has shown that phytoplankton layers are often unusual in species composition, grazing intensity, or organism motility (Rines et al. 2002; Menden-Deuer 2008; Sullivan et al. 2010). All of these studies have demonstrated that layer formation and maintenance is the result of the interaction among many different biological and physical processes.

The KiSS model was perhaps the first to relate plankton patches to a balance of growth and diffusion (Skellam 1951; Kierstead and Slobodkin 1953). Young et al. (2001) demonstrated that spatial heterogeneity of phytoplankton can occur through the spatial asymmetry of reproductive and mortality processes, combined with homogeneous

diffusion. Others have suggested that planktonic spatial structure may be driven by turbulence (Platt 1972), or the combination of turbulence with biological processes (Denman and Platt 1976; Powell and Okubo 1994; Abraham 1998). Lande et al. (1989) used observed vertical distributions of phytoplankton populations in a model to estimate the net population growth rates required to balance vertical diffusion. Several models have been formulated to investigate mechanisms that can form phytoplankton layers despite active mixing (Stacey et al. 2007; Birch et al. 2009). Such models evince a strong consensus that phytoplankton patchiness is controlled by an interplay between biological and physical dynamics (Malchow et al. 2001). These models coupled with interdisciplinary thin layer field studies (Cheriton et al. 2009; Ryan et al. 2010; Wang and Goodman 2010) have greatly increased our understanding of the mechanisms that control the vertical structure of phytoplankton distributions; however, there is still a need for a general model of vertical phytoplankton layering that will provide the ability to predict and compare the occurrence of phytoplankton features across a range of ecosystems.

Phytoplankton layers are bounded locally by sharp vertical gradients in phytoplankton abundance above and below a peak. Thus, analyzing gradients in phytoplankton distributions may provide important indications of the strength of phytoplankton patchiness and aid in quantifying the underlying mechanisms. Asymmetric layers, with marked differences between their upper- and lower-edge gradients, have been found to be common features in coastal waters (Mitchell et al. 2008). Opposite edges of these layers are often associated with large differences in physical properties (Steinbuck et al. 2009). Benoit-Bird et al. (2009) investigated phytoplankton layer shape,

and concluded that increased predator grazing, rather than physical factors, was responsible for the observed asymmetry in layers.

Sharp gradients in phytoplankton concentration may form by biological mechanisms including increased local growth or changes in swimming velocity (e.g., Stacey et al. 2007; Birch et al. 2009; Durham et al. 2009). In addition, certain physical dynamics – vertical shear, for example – may also play a role in sharpening and maintaining gradients (Franks 1995; Birch et al. 2008). Other physical mechanisms, such as turbulent mixing, tend to erode phytoplankton gradients (e.g., Stacey et al. 2007; Birch et al. 2008).

Here, we attempt to identify the biological and physical factors underlying observed phytoplankton distributions by analyzing vertical gradients in phytoplankton concentration data. The data were collected during a cruise in September 2006 off the coast of southern California, and acquired with a novel fluorescent particle imaging system. We interpret our findings using a model that predicts the maximum strength of phytoplankton gradients given a combination of biological and physical parameters. By comparing our data to this model, we were able to make estimates of the layer formation rates required to maintain the observed gradients as well as the minimum attainable thickness for phytoplankton layers in our study.

Methods

Description of the FIDO-Φ instrument package

The free-fall imaging device for observing phytoplankton (FIDO-Φ) is a planar laser imaging fluorometer system that can resolve individual fluorescent particles in the imaging plane (Figure 4.1A) (Jaffe et al. 1998; Franks and Jaffe 2001; Franks and Jaffe 2008). The FIDO-Φ has a laser and camera mounted on opposite sides of a frame and angled downward at 45˚. The 3 W 532 nm diode-pumped solid-state laser emits a sheet of light 6.5 mm thick that is imaged by the camera at a 90˚ angle, with the center of the image plane ~60 cm below the bottom of the frame (Figure 4.1B). A filter interposed between the lens and the camera transmits light between 670-690 nm (chlorophyll *a* fluorescence). The images from the FIDO-Φ have a field of view of ~9.8 cm x 13 cm with a resolution slightly less than 100 μm pixel^{-1}. For a full description of the FIDO-Φ see Prairie et al. (2010).

A WETStar fluorometer (WETLabs Inc., Philomath Oregon) sampling at 0.5 Hz was mounted 8 cm below the pressure sensor of the FIDO-Φ. Additionally, a self-contained autonomous microstructure profiler (SCAMP, Precision Measurement Engineering) was mounted with the probes 48 cm below the depth sensor of the FIDO-Φ. The SCAMP measured temperature, conductivity, and pressure at 100 Hz. The data streams of the different instruments and the FIDO-Φ were merged together based on depth, after the depth offsets were applied.

TurboMAP-L microstructure profiler

A free-falling turbulence ocean microstructure acquisition profiler-laser (TurboMAP-L) (Figure 4.2) was deployed concurrently with the FIDO-Φ during the

2006 cruise (Table 4.1). The TurboMAP-L and FIDO-Φ were deployed ~100 m apart; since both instruments were subject to horizontal drift as they descend, the horizontal displacement between the two sets of measurements was likely much greater. The TurboMAP-L carried sensors for turbulent shear and temperature gradient, in addition to biological and turbidity microstructure (Doubell et al. 2009; Yamazaki et al. 2009). Sample rates ranged between 64 and 512 Hz for different parameters, and typical profiling speeds were between 0.50-0.80 m s^{-1}. For a full instrument description, see Doubell et al. (2009). In the present analyses, shear measurements from the TurboMAP-L were used to estimate dissipation rates of turbulent kinetic energy.

Description of the 2006 cruise

The FIDO-Φ was deployed at night during a cruise on the R/V *Wecoma* from 31 August 2006 to 07 September 2006 in the Santa Barbara Channel (SBC) off the coast of Southern California (see Prairie et al. 2010). Each deployment of the FIDO-Φ consisted of 1 or 2 consecutive drops with images acquired during the vehicle's descent. Although the FIDO-Φ primarily descends vertically, some horizontal movement occurs due to the semi-Lagrangian nature of the vehicle. This horizontal movement, combined with the effects of internal waves, produced ~10 cm-scale noise in FIDO-Φ data that was removed by binning and smoothing the data (see below). This noise was so pronounced in the top 10 to 20 m of the profiles (varying among drops) that these regions were not used in the analyses. The descent rate of the instrument package ranged between 3 to 12 cm s^{-1} among drops, but was relatively constant within a drop. Images of fluorescent particles

were acquired at a rate of 2 Hz. Only the seven FIDO-Φ drops that had concurrent TurboMAP-L data were analyzed (Table 4.1).

Profiles were also made with the ship-deployed SBE 911plus conductivity-temperature-depth (CTD) system (Sea-Bird Electronics, Bellevue Washington), equipped with a rosette with 10 L Niskin bottles and a WETStar fluorometer before or after each of the FIDO-Φ deployments to acquire chlorophyll *a* samples in order to calibrate the fluorescence profiles of the FIDO-Φ and the WETStar fluorometer attached to the FIDO-Φ. Analysis of the water samples included quantifying species composition as described in Prairie et al. (2010).

Image processing and beam correction

A brief summary of the processing of the FIDO-Φ images described in detail in Prairie et al. (2010) is provided. The raw 1040 x 1376 pixel images were corrected for the spreading of the laser sheet that created systematic variations of fluorescence signal strength across the image (Zawada 2002). The corrected images show relative fluorescence, necessarily independent of the incident illumination.

For each drop, profiles of bulk fluorescence were obtained by integrating the total fluorescence signal over each FIDO-Φ image. Binning all data (fluorescence, particle concentration, etc.) from the FIDO-Φ over 30 cm and smoothing using a LOWESS (locally weighted smoothing scatter) method over 1.5 m removed noise at scales < 30 cm. This smoothing did not remove structures < 1.5 m, but rather attenuated the fluorescence signal of one- or two-point peaks. Fluorescence profiles were then calibrated to concurrent independent profiles of chlorophyll *a* fluorescence from the WETStar

fluorometer attached to the FIDO-Φ and to the chlorophyll *a* samples taken before or after the FIDO-Φ deployments.

The fluorescent particle concentrations of each image were calculated by labeling every particle above a fluorescence intensity threshold in the image (Figure 4.3), and dividing the number of particles by the imaging volume. The fluorescence threshold was necessary to eliminate the background fluorescence, and resulted in exclusion of the smaller (less fluorescent) fluorescent particles. Thus, only the largest fluorescent particles (e.g., large eukaryotic phytoplankton, chains, and fluorescent aggregates) are included in our profiles of fluorescent particle concentration. Although we cannot definitively determine the minimum size of the particles we count in our images, from instrument specifications and laboratory experiments (Zawada 2002) we estimate that this value is between 20 μm and 100 μm.

The fluorescent particles counted in our images include individual phytoplankters and chains, as well as aggregates including phytoplankton. For the sake of brevity we will refer to all of the fluorescent objects as 'particles'. The fluorescence of the particles counted in our images – that is, those particles above the fluorescence threshold – accounted for 4.4-18.4% (average 10.4%) of the bulk fluorescence signal in our images averaging through entire drops.

Profiles of fluorescent particle concentration versus depth were constructed by calculating the number of particles per image at each depth, and dividing it by the volume of the imaged region. These profiles were binned to 30 cm and smoothed using a LOWESS (locally weighted smoothing scatter) method over 1.5 m just as the fluorescence profiles.

Calculation of phytoplankton and fluorescence gradients

We define the scaled particle concentration gradient (SP_CG) as:

$$SP_CG = \left| \frac{1}{P_C} \frac{\partial P_C}{\partial z} \right| \quad (1)$$

where P_C is particle concentration and z is depth. The SP_CG (units: m^{-1}) was calculated as the difference between two adjacent points in the smoothed and binned fluorescent particle concentration profile divided by the average of the two points. The SP_CG is a local measure of the sharpness of the particle concentration gradient estimated from the fluorescent particle concentration data. Scaling the vertical gradient by the local concentration gives the SP_CG as an inverse length scale, which is the fractional increase (or decrease) in concentration per meter, relative to the local concentration. The SP_CG allows comparison of particle gradients among different regions of the water column.

Similarly, the scaled fluorescence gradient (SFG) was defined as:

$$SFG = \left| \frac{1}{F} \frac{\partial F}{\partial z} \right| \quad (2)$$

where F is fluorescence. The SFG was calculated as the difference between adjacent points in the smoothed and binned FIDO-Φ bulk fluorescence profile divided by the average of the two points.

Calculation of physical parameters

Density profiles were obtained from the SCAMP, binned to 1 cm, and smoothed over 30 cm. The buoyancy frequency, N, is defined as

$$N = \sqrt{-\frac{g}{\rho}\frac{d\rho}{dz}} \tag{3}$$

where g is the acceleration due to gravity, ρ is density, and z is depth. To remove small-scale variability, N was calculated from the smoothed SCAMP density data, using sliding 2 m bins in 30 cm intervals to match the points where the scaled gradients were calculated.

The dissipation rate of turbulent kinetic energy, ε, was calculated from the vertical shear of the horizontal velocities measured by TurboMAP-L using:

$$\varepsilon = \frac{15}{4}\nu\left(\left\langle\left(\frac{\partial u'}{\partial z}\right)^2\right\rangle + \left\langle\left(\frac{\partial v'}{\partial z}\right)^2\right\rangle\right) \tag{4}$$

where $\langle\cdot\rangle$ is an ensemble average, *u'* and *v'* are the fluctuations of the horizontal velocities, and v is the kinematic viscosity (Tennekes and Lumley 1972; Yamazaki et al. 2009). This formula assumes that the turbulence is locally isotropic. The shear variance was estimated by integrating the power spectrum of the velocity shear between length scales of 1 cpm and half the Kolmogorov scale. A correction was made to recover the unresolved variance using the Nasmyth empirical spectrum (Oakey 1982).

The dissipation rates of turbulent kinetic energy were calculated in sliding ~2 m bins in 30 cm intervals, corresponding to the depths of particle concentration and fluorescence data from the FIDO-Φ. Eddy diffusivities (or vertical turbulent diffusivities), K_ρ, were then calculated using the dissipation method (as described in Osborn 1980) for the same 30 cm bins as used for the FIDO-Φ data:

$$K_\rho = \frac{R_f}{(1-R_f)}\frac{\varepsilon}{N^2} \tag{5}$$

where R_f is the flux Richardson number. Osborn (1980) found that an upper bound could be placed on the flux Richardson number, yielding the following upper limit approximation on eddy diffusivity, which we used in this study:

$$K_\rho \leq \frac{0.2\varepsilon}{N^2} \tag{6}$$

The Phytoplankton Gradient Model

To model the observed phytoplankton vertical distributions, we assumed that diffusion K_ρ due to local turbulence would physically displace phytoplankton away from an ideal layered distribution. At steady state, the rate that phytoplankton form a layer (R_{PL}) through enhanced local growth, swimming, or other (unspecified) processes, would balance the diffusion that erodes the layer. These dynamics are described by the differential equation:

$$\frac{\partial P}{\partial t} = K_\rho \frac{\partial^2 P}{\partial z^2} + R_{PL} = 0 \tag{7}$$

where K_ρ is a locally constant vertical eddy diffusivity, P is phytoplankton concentration, z is depth. R_{PL} – the rate of phytoplankton layering – is the depth-dependent rate at which $P(z)$ reforms to an ideal underlying layered distribution $P^*(z)$ in the absence of mixing. R_{PL} is thus defined as:

$$R_{PL} = \gamma(P^*(z) - P(z)) \tag{8}$$

where γ is the phytoplankton-specific layer reformation rate. Note that while γ is constant with depth, the magnitude and sign of R_{PL} at a given depth depend on the difference

between the observed phytoplankton concentration *P(z)* and the ideal distribution *P*(z)*. We model the ideal phytoplankton distribution, *P*(z)* as an exponential peak:

$$P^*(z) = P_0 e^{-\frac{|z-z_0|}{d}} \tag{9}$$

where z_0 is the depth of the layer peak, P_0 is the maximum phytoplankton concentration of *P*(z)*, and *d* is a vertical length scale (specifically, the e-folding scale) describing the thickness of the idealized layer *P*(z)* in the absence of mixing. Note that throughout this paper the "layer thickness" *d* refers to only half the thickness of a layer flanked by positive and negative concentration gradients. Such an isolated layer, if symmetric, would have a full thickness of 2*d*.

Defining a coordinate system $z'=z-z_0$ so that $z'=0$ is centered at the depth of the peak, we used no-flux boundary conditions at the peak maximum and a distance *L* away from the peak (*L*>>*d*):

$$\frac{dP(L)}{dz} = 0 \qquad \frac{dP(0)}{dz} = 0 \tag{10}$$

With these boundary conditions, the steady-state solution of this equation is:

$$P(z) = c_1 e^{\eta z'} + c_2 e^{-\eta z'} + C e^{\frac{-|z'|}{d}} \tag{11}$$

where

$$\eta = \sqrt{\frac{\gamma}{K_\rho}},\ C = \frac{P_0 d^2 \gamma}{d^2\gamma - K_\rho},\quad c_1 = \frac{C(b+1)}{\eta d},\quad c_2 = \frac{Cb}{\eta d},\ b = \frac{e^{-\frac{L}{d}} - e^{\eta L}}{e^{\eta L} - e^{-\eta L}} \tag{12}$$

The steady-state phytoplankton layer in the presence of mixing (Figure 4.4) shows a decrease in the layer intensity (lower peak maximum), and a broader vertical distribution than the ideal underlying layer, *P*(z')*.

The maximum scaled phytoplankton gradient (SPG_{max}) of a layer is defined as:

$$SPG_{\max} = \max\left(\frac{1}{P}\frac{\partial P}{\partial z}\right) \tag{13}$$

The SPG_{max} is the maximum of the local vertical gradient of the phytoplankton, divided by the local concentration. It has dimensions of $length^{-1}$, and gives a measure of the sharpness of local changes in phytoplankton concentration. Through numerical analyses we found that SPG_{max} was nonlinearly related to η, resulting in two scaling regions:

$$SPG_{\max} \approx \eta = \sqrt{\frac{\gamma}{K_\rho}} \qquad \text{for small } \eta \tag{14}$$

$$SPG_{\max} \approx d^{-1} \qquad \text{for large } \eta. \tag{15}$$

where d is the vertical length scale of the idealized layer *P*(z)* as defined in equation 9. As η increases (that is the ratio of the layer reformation rate to the diffusivity increases), the SPG_{max} initially increases linearly with η (Figure 4.5). However, as η increases further, the diffusivity is too weak to displace phytoplankton from their ideal profile *P*(z)*, whose vertical length scale (i.e. SPG_{max}) is given by d^{-1} (eq. 9). Thus for high η (weak diffusivity, strong layer reformation), the maximum scaled phytoplankton gradients asymptote to the inverse of the same length scale as the underlying ideal layered distribution, d – that is, the actual profile *P(z)* is close to the ideal profile *P*(z)*. In this study, we compare the theoretically calculated SPG_{max} (eqs. 14 and 15) to both fluorescent particle concentration and bulk fluorescence data (SP_CG and SFG). We

expect the observed values of SP_CG and SFG to be equal to or less than this theoretical SPG_{max}.

Results

Observation of gradients and physical variables

From the 7 drops we analyzed from the September 2006 cruise, we calculated the scaled particle concentration gradient (SP_CG), buoyancy frequency (N), and vertical eddy diffusivity (K_ρ) for a total of 903 vertical depth bins (each 30 cm). In general, strong SP_CG were associated with sharper density gradients: 77.0% of $SP_CG > 0.20$ m^{-1} and 87.9% of $SP_CG > 0.40$ m^{-1} lay in regions with $N > 0.01$ s^{-1}, while only 64.6% of the water column as a whole had this property. Similarly, strong SP_CG were associated with regions of weaker mixing: 48.5% of $SP_CG > 0.20$ m^{-1} lay in regions with $K_\rho < 10^{-6}$ m^2s^{-1}, while only 37.1% of the water column as a whole had this property (Figure 4.6). The probability density function of the observed SP_CG was skewed to the right, with a mean value of 0.18 m^{-1} and a median value of 0.12 m^{-1} (Figure 4.7A). The scaled fluorescence gradient (SFG) also showed a skewed distribution (Figure 4.7B), but with higher overall values, having a mean of 0.21 m^{-1} and a median of 0.11 m^{-1}.

Comparison of data with the model

Our model (eqs. 11, 12, 14 and 15) predicts that the $SPG_{max} \approx (\gamma / K_\rho)^{1/2}$ for small η (weaker layer reformation rate γ, stronger mixing K_ρ), and then asymptotes to $SPG_{max} \approx d^{-1}$ at higher values of η (stronger layer reformation rate γ, weaker mixing K_ρ). Since there

was no way to measure the layer reformation rate γ directly in the field, we diagnosed it from the data by plotting the observed SP_CG and SFG vs. $(1/K_\rho)^{1/2}$ (Figure 4.8A). If the predictions of the model hold, we would expect to see the SP_CG and SFG values bounded by an envelope formed by the theoretical SPG_{max} (as described in eqs. 14 and 15). The slope of the linear section of this envelope should be the maximum of $\gamma^{1/2}$ (eq. 14) and was used to estimate the maximum layer reformation rate, γ_{max}. Furthermore, the asymptote of the envelope should equal d^{-1} (eq. 15). Since d represents the vertical length scale of the idealized underlying phytoplankton layer in our model, this asymptote can be used to estimate the minimum achievable layer thickness d_{min}, the idealized layer thickness in the absence of mixing (defined as the e-folding scale of P^* as in equation 9).

The data plotted in Figure 4.8 show that the observed SP_CG and SFG were found over a range of diffusivities, with most of the data at low values of $(1/K_\rho)^{1/2}$. There were occasional high values of SP_CG and SFG, which we assumed were close to the SPG_{max}.

Using the envelope SPG_{max} predicted by the model, we fit a family of curves containing 99% of the SP_CG values by varying the slope $\gamma^{1/2}$ and gradient ceiling d^{-1} (Figure 4.8A). The slopes of the linear sections of these envelopes ranged between 0.0023 - 0.0033 $s^{-1/2}$, giving γ_{max} between 0.46 - 0.94 d^{-1}. The model further indicates that the asymptote of the envelopes ranged between 0.9 - 1.25 m^{-1}, corresponding to a d_{min} value (minimum idealized layer thickness) of ~1 m. Sensitivity tests showed that smoothing the data affected the maximum gradients observed; however, by considering both unsmoothed data and data smoothed up to 6 m, we estimated that d_{min} fell between 0.4 m to 1.4 m.

The *SFG* data demonstrated greater spread and a less-defined envelope edge than the SP_CG data (Figure 4.8B). From the SPG_{max} envelopes we estimated γ_{max} to be 2.25 - 9.71 d^{-1}. Likewise, the asymptotes of the envelopes ranged between 1.7 - 2.6 m^{-1}, corresponding to a minimum idealized layer thickness of ~0.5 m. Smoothing had a greater effect on the *SFG* data, only allowing us to constrain d_{min} within the range of 0.2 - 2.7 m for different scales of smoothing.

These estimated values of γ_{max} are the maximum possible layer reformation rates. Given that 99% of the *SPCG* and *SFG* data points lie below the envelope (by design), we expect the realized layer reformation rates, γ. to be considerably lower than the maximum. Similarly, we expect the realized layer thicknesses to be larger than d_{min}, again, placing the SP_CG and *SFG* data below the theoretical envelope.

Discussion

The data presented here show that strong phytoplankton gradients were generally associated with strong density gradients, and thus more stable regions of the water column, consistent with other studies (Cowles et al. 1998; McManus et al. 2003; Steinbuck et al. 2009). However, stratification or diffusivity alone did not explain a great deal of the variability in the strength of observed gradients. This result is not surprising, and most studies in this field have recognized that vertical phytoplankton distributions are controlled by a combination of physical and biological dynamics (Stacey et al. 2007; Birch et al. 2009). For phytoplankton gradients to be maintained, there must be a balance of the processes that create and dissipate them. We developed a simple model that contained these two dynamics – layer formation and dissipation (diffusion) – to aid in the

interpretation of phytoplankton distribution data. The layer reformation rate γ as defined in the model includes any processes that would tend to form a phytoplankton layer at a given depth. These processes include enhanced local growth, decreased local mortality, directed swimming, or local decreases in sinking rates. Some physical processes can also form phytoplankton layers and thus be included in γ. For example, horizontal intrusions of phytoplankton-rich water and vertical shearing of phytoplankton patches can form layers and sharpen phytoplankton gradients (Franks 1995; Birch et al. 2008).

To compare our data with the phytoplankton gradient model, we plotted the observed SP_CG and SFG vs. $(1/K_\rho)^{1/2}$ to estimate values for γ_{max}, the maximum layer reformation rate, and d_{min}, the minimum layer thickness. Given that our measurements of phytoplankton gradients and K_ρ were from completely independent sources, there are some promising features that support the underlying theory of our model. Our data showed that whereas there were many regions with small values of $(1/K_\rho)^{1/2}$ (i.e., relatively strong mixing), very few of these strong mixing regions had strong gradients in particle concentration or fluorescence. There is a clear absence of data in the upper left of Figures 4.8A and 4.8B. These observations support the prediction of our model that sharper phytoplankton gradients occur in regions of weaker mixing. In addition, the model predicted that there should be a limit to the strength of the observed SP_CG and SFG, given by d_{min}^{-1}. This prediction was supported by the relatively well-defined upper limit to the SP_CG and SFG data (Figure 4.8). It is important to note that although the data smoothing affected the magnitude of the maximum observed gradients, the shape of the data (as shown in Figure 4.8) was insensitive to data smoothing. Here we explore aspects

of our analyses, including the differences between the SP_CG and SFG, and the calculated values of γ and d in relation to the assumptions of the model.

Comparison of phytoplankton concentration and fluorescence gradients

The range of scaled gradients was higher in fluorescence (SFG) than in particle concentration (SP_CG) (Figure 4.8). The highest value of SP_CG was <1.5 m^{-1}, while the SFG exceeded 2 m^{-1}. Since only particles greater than ~20-100 μm were counted in profiles of particle concentration, this indicates that the fluorescence of the phytoplankton community as a whole had greater spatial variability than the concentration of the large fluorescent particles counted in our images. This is consistent with the fact that chlorophyll *a* fluorescence varies by factors other than total biomass, including species composition and light history (Cullen 1982).

In the water samples collected before and after the FIDO-Φ deployments, over 95% of the species larger than 20 μm consisted of non-swimming, chain-forming diatoms (Prairie et al. 2010). These large phytoplankton presumably formed the majority of the fluorescent particles imaged. The value of γ_{max} calculated from the slope of the envelopes fit to the SP_CG data ranged between 0.46 - 0.94 d^{-1}. This range is consistent with maximum growth rates of *Pseudo-nitzschia* – the dominant genus found in our samples – as calculated from laboratory studies (e.g., Thessen et al. 2009). Although sinking and other mechanisms may also have played a role forming the observed phytoplankton gradients, from this we infer that the estimated maximum layer reformation rate γ_{max} for the particle concentration data (SP_CG) could potentially be accounted for by local enhanced net growth alone. The large phytoplankton in this study were largely non-

motile; however, many studies of phytoplankton layers have demonstrated that phytoplankton swimming may be an important mechanism for layer formation and maintenance (Cheriton et al. 2009; Ryan et al. 2010; Sullivan et al. 2010). In these cases, much larger values of γ may be expected, allowing sharper gradients to form, possibly even in regions of strong turbulence.

The γ_{max} calculated from the *SFG* data are clearly far larger than realistic phytoplankton growth rates. However, these γ_{max} were driven by a few extreme values. Specifically, 97.9% of the *SFG* data could be enclosed by an envelope with the same slope ($\gamma_{max} = 0.0033$ $s^{-1/2}$) as the envelope fit to the SP_CG data. In addition, the edge of the envelope fit to the *SFG* data was much less well defined than that for the SP_CG data. This analysis implies that the *SFG* was more prone to outliers not contained by what we believe to be a realistic theoretical envelope. These outliers are a consequence of what the variables SP_CG and *SFG* represent. Whereas the SP_CG describes vertical changes in the concentration of large fluorescent particles (greater than ~20-100 μm), the *SFG* data describes changes in the bulk fluorescence, which can often vary significantly due to changes in the size composition of the phytoplankton community (Prairie et al. 2010). Bulk fluorescence is a more general measure that includes all phytoplankton from cyanobacteria to large eukaryotes. These diverse phytoplankton types are likely to react differently to physical and biological forcings, thus violating our model assumption of a constant layer reformation rate γ.

Layer reformation rate

The γ_{max} calculated from the envelopes fit to our data represent the maximum observed values of this parameter. We do not expect the realized values of γ to be nearly as high as the maximum; indeed most of the SP_CG and SFG data were well below the theoretical envelope. We estimated the realized individual values of γ for each of the 903 data points using the measured SP_CG and diffusivity K_ρ:

$$\gamma = \left(\frac{\left| \frac{1}{P_C} \frac{\partial P_C}{\partial z} \right|}{\sqrt{\frac{1}{K_\rho}}} \right)^2 = \left(\frac{SP_CG}{\sqrt{\frac{1}{K_\rho}}} \right)^2 \qquad (16)$$

that is, the square of the slope of the line drawn from the origin to each point in Figure 4.8A. These individual γ values from the SP_CG data had a mean of 0.0360 d^{-1} and median of 0.0025 d^{-1} (Figure 4.9A), suggesting that the individual realized layer reformation rates γ were quite small – much less than a typical phytoplankton growth rate. The ratio γ/γ_{max} (Figure 4.9B) gave a mean of 0.0383 and the median of 0.0027, implying that the majority of the measured vertical gradients could be formed and maintained with growth rates less than 1% of the maximum estimated (0.94 d^{-1}).

One explanation for the observed SP_CG and SFG being much smaller than the maximum is that in a nonlinearly peaked concentration profile, only a small portion of each peak will have a scaled concentration gradient near the maximum; all other scaled concentration gradients measured around that peak would – by definition – be much less.

Another explanation for the observed gradients (SP_CG and SFG) being much less than the maximum is that the observed gradients were not, in fact, at steady state as required by the model, but were being actively eroded or formed. Several persistent phytoplankton features were observed in the FIDO-Φ deployments over consecutive

drops (Prairie et al. 2010); however, horizontal drift between drops and the small time resolution (~1 h) prevented us from using these drop pairs to determine whether gradients were in steady state (Prairie et al. 2010). Instead, we used dimensional analysis to estimate the time to reach a steady state in the model. When K_ρ is small (weak mixing), the time for the model to reach steady state is $\sim\gamma^{-1}$. When K_ρ is large (strong mixing), the time to steady state is $\sim(d^2/\gamma K_\rho)^{1/2}$. Using these approximations (which were confirmed with numerical analyses), we found that only ~17% of our observations represented a time to steady state of <5 days, whereas the median time to steady state was >100 days. Clearly this is unrealistically long, suggesting that most of the observed gradients were not in steady state, and the departures of the observed SP_CG and SFG from the envelope were due to the gradients being out of a biological-physical equilibrium.

Our conclusion that most observed gradients were not in steady state demonstrates that this assumption of our model does not always hold, especially for gradients representing low values of γ. Weak individual gradients not in steady state may represent stronger gradients being actively formed. In this case our calculations of individual γ values would underestimate local layer reformation rates, providing a potential explanation for the skewed distributions of gradients and individual values of γ (Figures 4.7 and 4.9). This reinforces the importance of resolving phytoplankton variability over relevant temporal scales as well as spatial scales: knowledge of the temporal persistence of phytoplankton gradients is important to understanding their underlying dynamics. Although the violation of the steady-state assumption confounds conclusions about individual gradients, our estimates of parameter values from the data as a whole, such as γ_{max} and d_{min} should not be affected.

Minimum phytoplankton layer thickness

The application of the model to our data allowed us to estimate the parameter d, a vertical length scale of the idealized underlying layer $P^*(z)$, or, in other words, the layer thickness in the absence of mixing. Although this length scale describes a theoretical minimum possible layer thickness given our data, this thickness can never be achieved in the presence of mixing. From the model we can relate the idealized length scale d to a realized layer thickness. We define this realized layer thickness as one standard deviation of the Gaussian curve that best fit the vertical profile of the steady-state phytoplankton layer resulting from the model. In conditions of relatively weaker mixing (large η), the phytoplankton are able to form thin layers with a thickness close to their ideal thickness d (Figure 4.10). With stronger mixing (small η), the layers become much thicker than the idealized underlying layer. With our value of d_{min} falling within the range 0.4 to 1.4 m estimated from the SP_CG data, and the values of η calculated from our data, we find that the minimum realizable particle concentration layer thickness ranged between 0.5 - 2.5 m. Likewise, for the *SFG* data, the minimum realizable fluorescence layer thickness ranged between 0.3 - 3.5 m.

Similar to the estimates of the layer reformation rate, the estimates of the minimum layer thickness d_{min} also represent extremes, since most of the gradients in particle concentration and fluorescence were much less than the maximum values observed (Figure 4.7). Individual layer thicknesses can be approximated from the inverse of each of the SP_CG and *SFG* values, and demonstrate the same skewed distribution as γ. Thus, whereas the minimum realizable layer thickness may be as thin as 0.5 m, the layer

thickness represented by gradients is on average much thicker than this minimum, suggesting that persistent phytoplankton layers less than 0.5 m thick may be rare in coastal waters. This conclusion is consistent with other studies measuring vertical phytoplankton structure and provides a possible explanation for infrequent observations of layers < 0.5 m in thickness (McManus et al. 2003; Ryan et al. 2008; Sullivan et al. 2010). The formation of thinner layers would require conditions of strong vertical density gradients, weak mixing, and strong layer reformation – through depth-directed swimming, for example.

Significance to aquatic environments

Phytoplankton thin layers represent regions of enhanced ecologically relevant activity, including processes such as zooplankton foraging, aggregate formation, sexual exchange, infection, and competition (Alldredge et al. 2002; McManus et al. 2003). In laboratory experiments, some zooplankton have been shown to be able to find and remain in regions of high prey concentration (Tiselius 1992; Menden-Deuer and Grünbaum 2006). Moreover, zooplankton models have demonstrated that this foraging behavior can result in significantly higher grazing and growth rates, thus having implications for higher trophic levels and for the speed of layer erosion (Davis et al. 1991; Leising and Franks 2000; Menden-Deuer and Fredrickson 2010). Formation of phytoplankton aggregates, a process with strong implications for carbon cycling in the ocean, will also be intensified in these regions, since aggregate formation relies on the encounter rate of individual particles (Jackson 1990). Other planktonic processes such as sex, infection, and competition also depend on the contact of individuals. The encounter rate between

two groups (e.g. males and females, predator and prey) scales as the product of the local concentrations of each group (Kiørboe 1997). Thus small changes in particle concentration can have disproportionate effects on the biological dynamics. It is these dynamics that determine the rates of fundamental ecosystem processes and the biogeochemical fluxes through a food web. Since these phytoplankton layers are of such ecological importance, it is essential to understand what controls the gradients that support these structures. This study presents a plausible mechanism determining the strength of phytoplankton gradients, which represent a balance of the processes forming layers and mixing that acts to diffuse them. This understanding allows some capability for predicting their occurrence, strength, and persistence, based on biological responses to the physical environment.

Acknowledgements

We thank F. Simonet, P. Roberts, and Y. Platoshyn for their help in designing, building, and deploying the free-fall imaging device for observing phytoplankton (FIDO-Φ), and E. Karaköylü and A. Lucas for their help configuring the auxiliary instrumentation. We thank E. Daniels and C. Anderson for the shipboard conductivity-temperature-depth (CTD) deployments and processing chlorophyll samples and H. McClendon for analyzing samples for species composition. In addition, we thank Y. Kokubu (TUMSAT), H. Li (JEF Advantech) and T. Horiuchi (JEF Advantech) in addition to the students in the laboratory of H. Yamazaki at the Tokyo University of Marine Science and Technology who helped collect and process the TurboMAP-L data. This work was supported by the U.S. Office of Naval Research grant N00014-06-1-0304, the National Science Foundation grant OCE 08-25154, and the Grant-in-Aid for Science Research (B2) 20340127. Finally, we would like to thank Emmanuel Boss and one anonymous reviewer whose helpful and constructive comments have greatly improved this manuscript.

Chapter 4, in full, has been submitted for publication of the material as it may appear in Limnology and Oceanography: Fluids and Environments, 2011, Prairie, J. C., Franks, P. J. S., Jaffe, J. S., Doubell, M. J., and Yamazaki, H. The dissertation author was the primary investigator and author of this paper.

Table 4.1 Description of the times, locations, and number of drops and images for each deployment of the FIDO-Φ on the 2006 cruise. The time of drop is listed as the time of acquisition of the first image.

FIDO-Φ drop number	Date of FIDO-Φ drop	Location of FIDO-Φ drop	Time of FIDO-Φ drop (PDT)	Duration of FIDO-Φ drop (minutes)	Corresponding TurboMAP-L drop	Time of TurboMAP-L drop (PDT)
Drop 3-1	01 Sep 06	34˚24'163 N, 120˚01'780 W	20:09 h	15	Drop 3-1	20:23 h
Drop 3-2	01 Sep 06	34˚24'163 N, 120˚01'780 W	20:38 h	14	Drop 3-7	20:41 h
Drop 4-1	01 Sep 06	34˚23'077 N, 120˚03'175 W	23:05 h	19	Drop 3-15	23:38 h
Drop 4-2	01 Sep 06	34˚23'077 N, 120˚03'175 W	23:39 h	53	Drop 3-19	23:55 h
Drop 7-1	03 Sep 06	34˚22'976 N, 120˚00'007 W	19:06 h	20	Drop 7-2	19:24 h
Drop 7-2	03 Sep 06	34˚22'976 N, 120˚00'007 W	19:53 h	42	Drop 8-2	20:08 h
Drop 8-2	04 Sep 06	34˚23'013 N, 120˚00'011 W	00:40 h	15	Drop 9-3	00:42 h

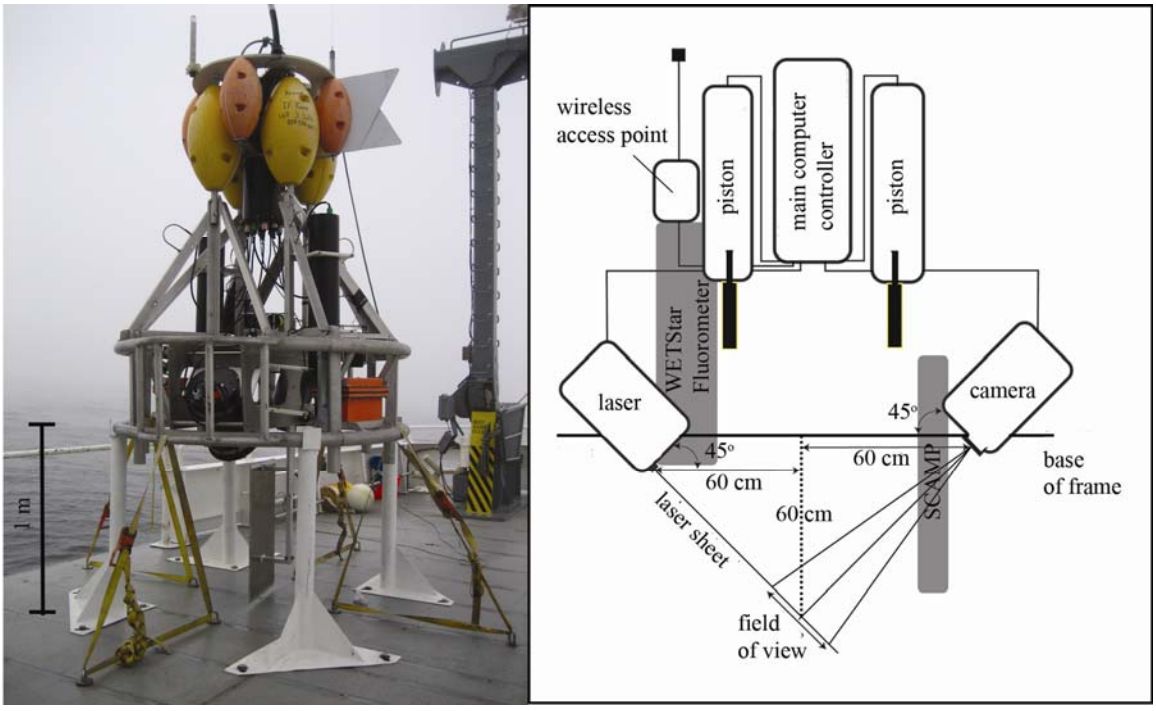

Figure 4.1 (A) The FIDO-Φ on deck of the R/V *Wecoma*. (B) Schematic of the FIDO-Φ system showing the camera and laser housings and the region where the laser sheet is imaged. The placement of the attached WETStar fluorometer and SCAMP are also shown.

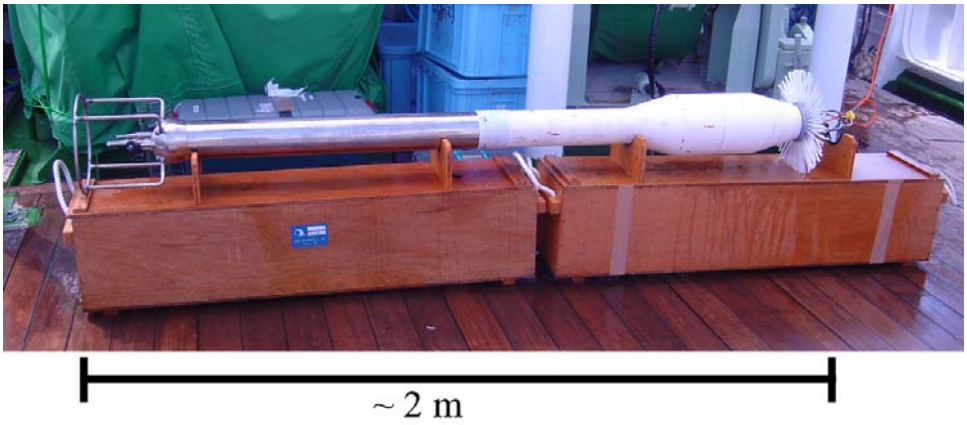

Figure 4.2 A photograph of the TurboMAP-L, deployed on the 2006 cruise concurrently with the FIDO-Φ. Data from the TurboMAP-L was used to estimate dissipation rates of turbulent kinetic energy.

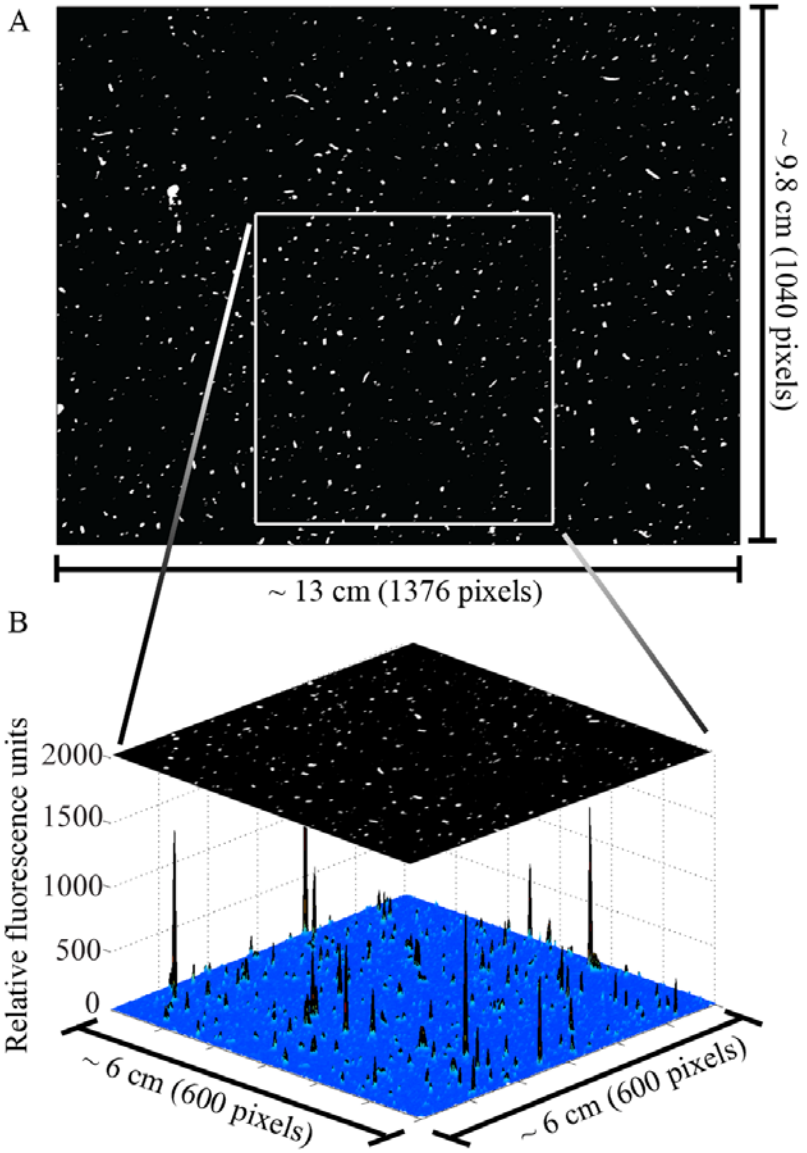

Figure 4.3 (A) An example of an image from the FIDO-Φ showing the distribution of fluorescent particles after the fluorescence threshold was applied. (B) A 600 pixel x 600 pixel inset of the same image. The bottom surface depicts the fluorescence intensities for the image inset. Any peaks that exceeded the fluorescence threshold (the threshold was 85 relative fluorescence units for this drop) are colored black, and are defined as particles. The resulting distribution of particles can be seen in the overlaid image inset.

Figure 4.4 Steady-state solution of the phytoplankton layer model for three different sets of parameters. The idealized underlying distribution $P^*(z')$ in the absence of mixing is shown in red, with a vertical length scale d = 1.2 m, P_0 = 1 mL^{-1}, and L = 5 m. The blue curve shows the steady-state phytoplankton concentration profile, $P(z')$, with parameters $K_\rho = 10^{-6}$ m^2 s^{-1} and $\gamma = 10^{-5}$ s^{-1}. The green curve shows the steady-state phytoplankton concentration profile, $P(z')$, with parameters $K_\rho = 5 \times 10^{-6}$ m^2 s^{-1} and $\gamma = 10^{-5}$ s^{-1}. The black curve shows the steady-state phytoplankton concentration profile, $P(z')$, with parameters $K_\rho = 10^{-5}$ m^2 s^{-1} and $\gamma = 10^{-5}$ s^{-1}. Orange and purple arrows to the right of the plot show the effects of increasing the parameters K_ρ and γ respectively on the steady-state solution of the model. Increases in the parameter K_ρ act to weaken gradients, by broadening and weakening the layer, while increases in γ act to sharpen gradients, by narrowing and intensifying the layer. Bars on the right of plot show regions were $R_{PL} > 0$ – that is, where $P^*(z')$ is greater than $P(z')$ – and regions where $R_{PL} < 0$ – that is, where $P(z')$ is greater than $P^*(z')$.

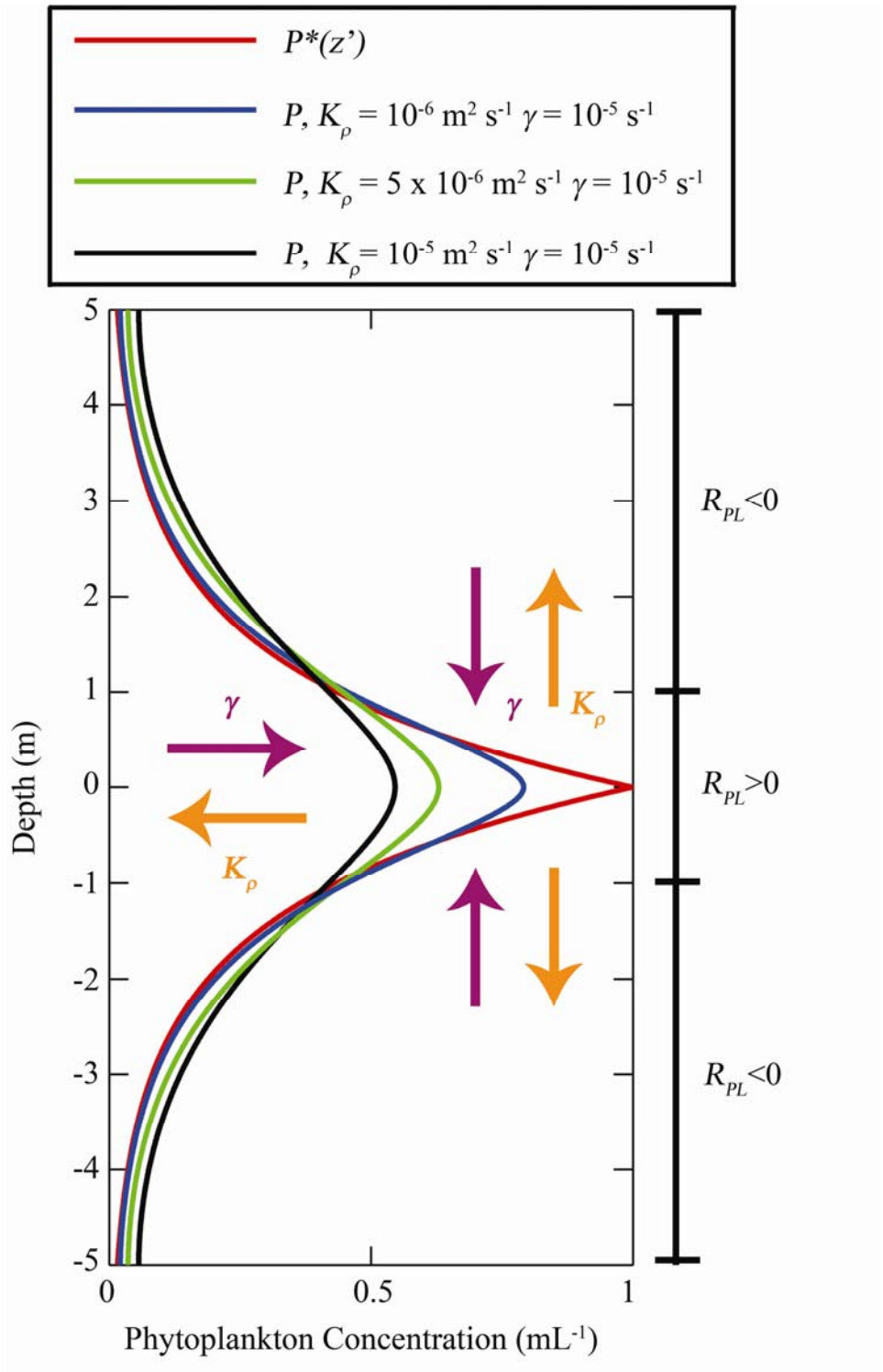
P*(z')
P, K_ρ = 10^-6 m^2 s^-1 γ = 10^-5 s^-1
P, K_ρ = 5 x 10^-6 m^2 s^-1 γ = 10^-5 s^-1
P, K_ρ = 10^-5 m^2 s^-1 γ = 10^-5 s^-1
Depth (m)
Phytoplankton Concentration (mL^-1)
R_PL<0
R_PL>0
R_PL<0
γ
K_ρ
γ
K_ρ

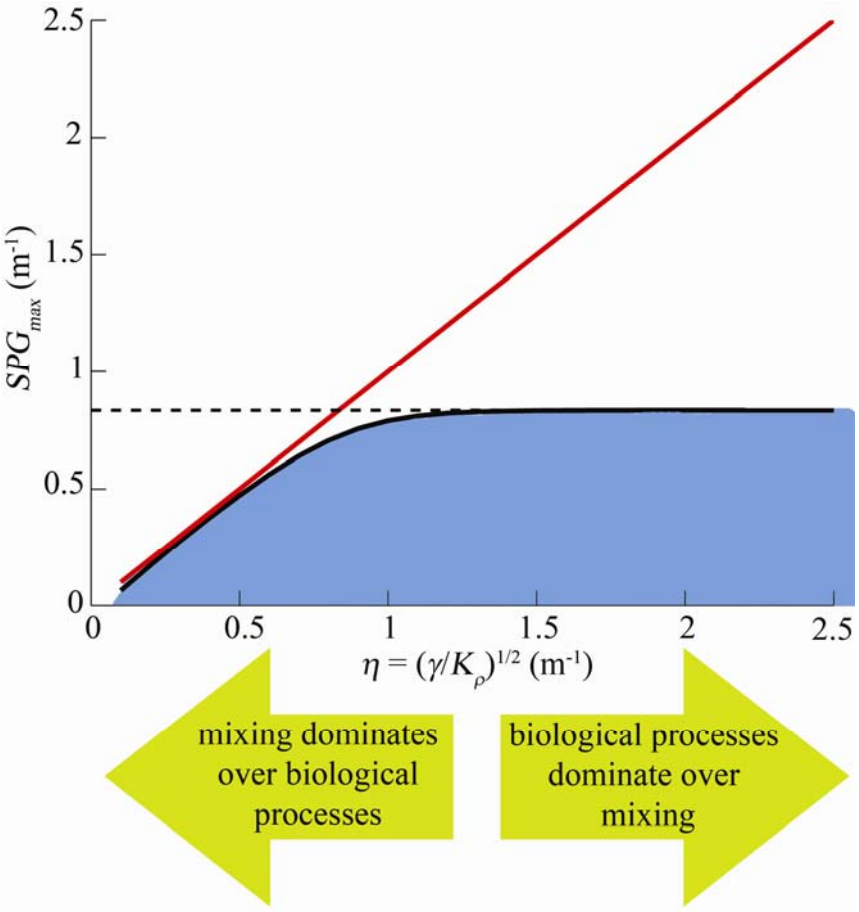

Figure 4.5 An example of the maximum phytoplankton gradient, SPG_{max}, derived empirically from the model at steady state, plotted vs. η, for d = 1.2 m (black line). The red line indicates the line $SPG_{max} = \eta$, and the horizontal dashed black line indicates the line $SPG_{max} = d^{-1}$, the two scaling regions for SPG_{max}. We would expect observed scaled concentration gradients to lie under the black curve, in the region colored blue, i.e. $SPG \leq SPG_{max}$.

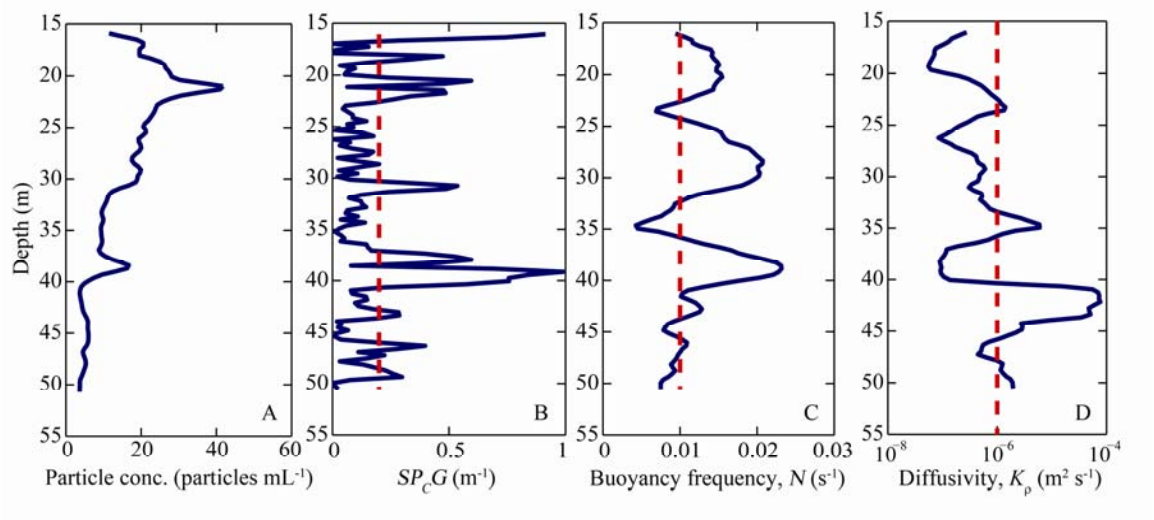

Figure 4.6 Vertical profiles of properties from Drop 7-2. (A) Fluorescent particle concentration. (B) Scaled particle concentration gradient, SP_CG. Red dotted line indicates a scaled particle concentration gradient of 0.2 m^{-1}. (C) Buoyancy frequency, N. Red dotted line indicates a buoyancy frequency value of $N = 0.01$ s^{-1}. (D) Diffusivity, K_ρ. Red dotted line indicates $K_\rho = 10^{-6}$ m^2s^{-1}.

.

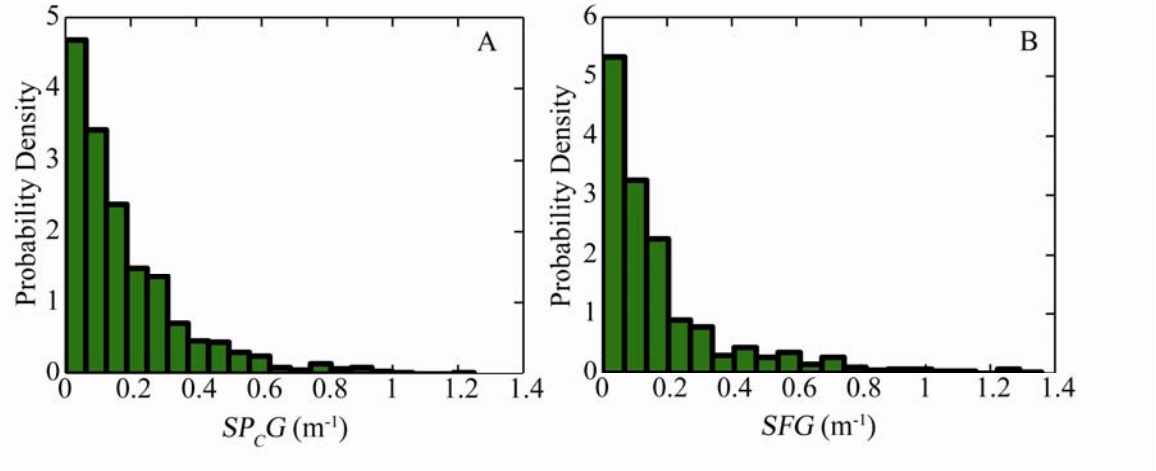

Figure 4.7 (A) Probability density function of all observed scaled particle concentration gradients (SP_CG) from 7 drops of the September 2006 cruise. (B) Probability density function of all observed scaled fluorescence gradients (SFG) from the same data.

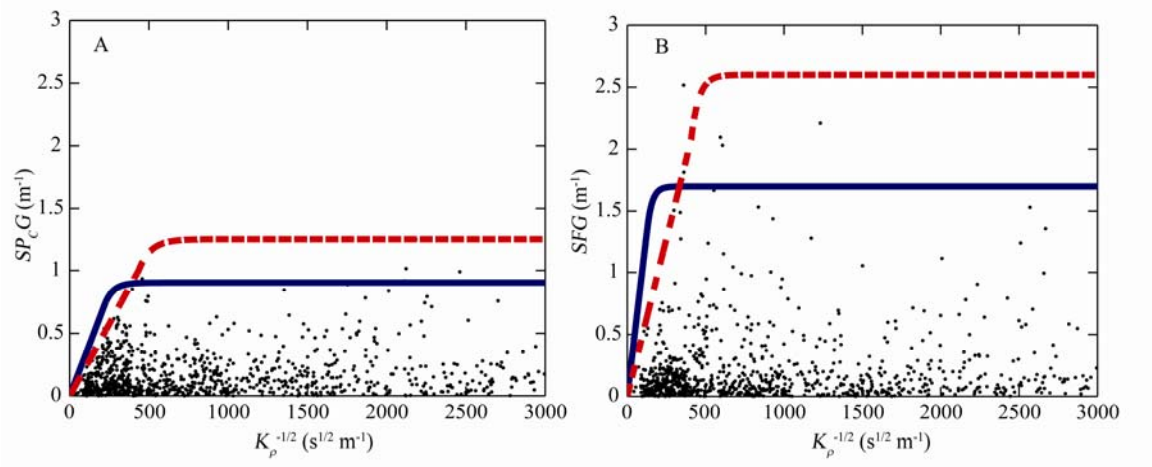

Figure 4.8 (A) Scaled particle concentration gradient (SP_CG) plotted vs. $K_\rho^{-1/2}$ for 30 cm sections of data from 7 drops of the September 2006 cruise. A family of envelopes containing 99% of the data points can be constructed by varying the slope ($\gamma_{max}^{-1/2}$) and gradient ceiling (d_{min}^{-1}). The blue curve displays the envelope with the maximum slope (0.0033 $s^{-1/2}$) and minimum gradient ceiling (0.9 m^{-1}). Conversely, the red dotted envelope displays the envelope with the minimum slope (0.0023 $s^{-1/2}$) and maximum gradient ceiling (1.25 m^{-1}). (B) Scaled fluorescence gradient (SFG) plotted vs. $K_\rho^{-1/2}$ for the same data. The blue curve displays the envelope with the maximum slope (0.0106 $s^{-1/2}$) and minimum gradient ceiling (1.7 m^{-1}). Conversely, the red dotted curve displays the envelope with the minimum slope (0.0051 $s^{-1/2}$) and maximum gradient ceiling (2.6 m^{-1}).

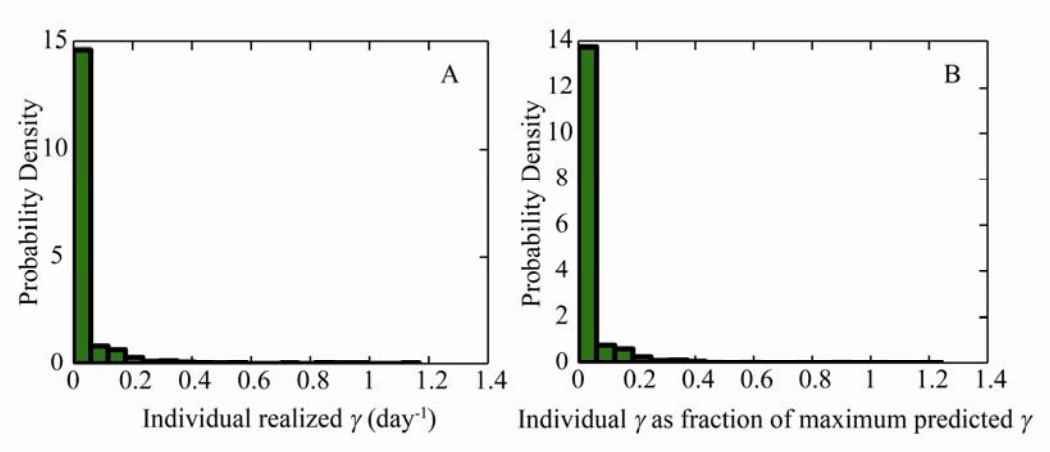

Figure 4.9 (A) Probability density function of the individual realized γ values for each SP_CG in Figure 7A. (B) Probability density function of the individual realized γ values for each SP_CG in Figure 7A as a fraction of the maximum estimated γ_{max} (0.94 day^{-1}).

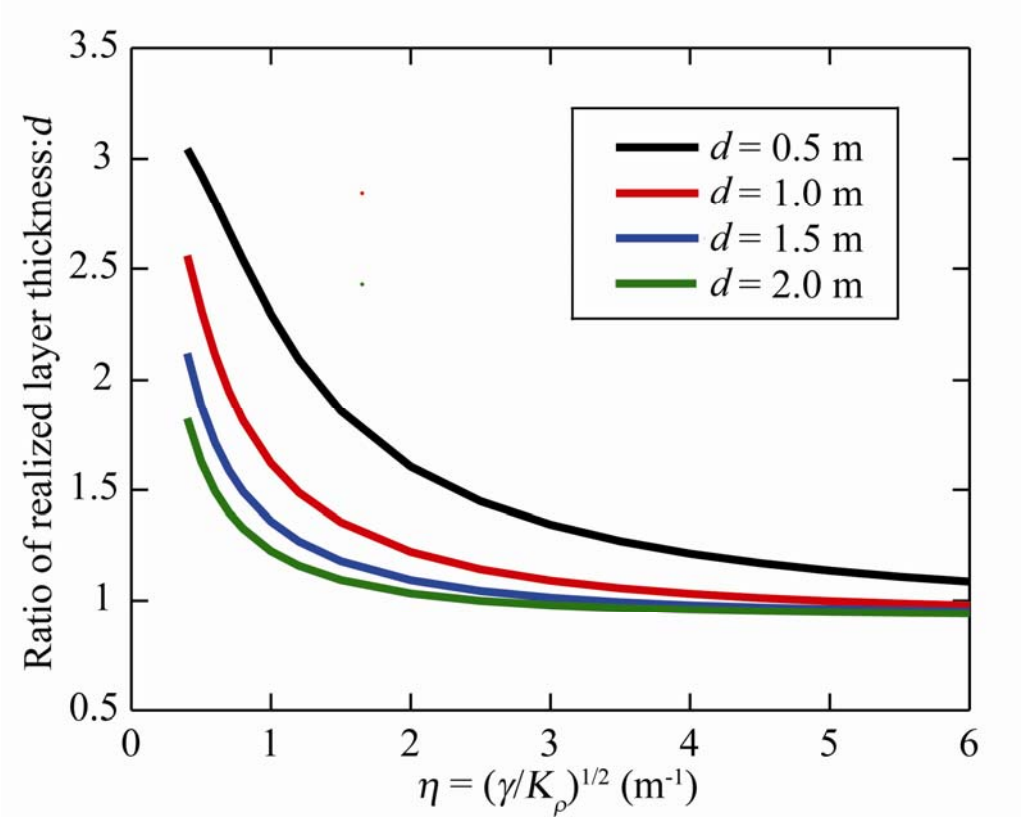

Figure 4.10 From the model solution at steady state, the ratio of the realized layer thickness to d, the idealized layer thickness in the absence of mixing, for given values of $\eta = (\gamma / K_\rho)^{1/2}$.

References

Abraham, E. R. 1998. The generation of plankton patchiness by turbulent stirring. Nature **391**: 577-580.

Alldredge, A. L., T. J. Cowles, S. MacIntyre, J. E. B. Rines, P. L. Donaghay, C. F. Greenlaw, D. V. Holliday, M. M. Dekshenieks, J. M. Sullivan, and J. R. V. Zaneveld. 2002. Occurrence and mechanisms of formation of a dramatic thin layer of marine snow in a shallow Pacific fjord. Mar. Ecol. Prog. Ser. **233**: 1-12.

Benoit-Bird, K. J., T. J. Cowles, and C. E. Wingard. 2009. Edge gradients provide evidence of ecological interactions in planktonic thin layers. Limnol. Oceanogr. **54**: 1382-1392.

Birch, D. A., W. R. Young, and P. J. S. Franks. 2008. Thin layers of plankton: Formation by shear and death by diffusion. Deep-Sea Res., Part I **55**: 277-295.

Birch, D. A., W. R. Young, and P. J. S. Franks. 2009. Plankton layer profiles as determined by shearing, sinking, and swimming. Limnol. Oceanogr. **54**: 397-399.

Cheriton, O. M., M. A. McManus, M. T. Stacey, and J. V. Steinbuck. 2009. Physical and biological controls on the maintenance and dissipation of a thin phytoplankton layer. Mar. Ecol. Prog. Ser. 378: 55-69.

Cowles, T. J., R. A. Desiderio, and M. Carr. 1998. Small-scale planktonic structure: persistence and trophic consequences. Oceanogr. **11**:4-9.

Cullen, J. J. 1982. The deep chlorophyll maximum: Comparing vertical profiles of chlorophyll *a*. Can. J. Fish. Aquat. Sci. **39**: 791-803.

Davis, C. S., G. R. Flierl, P. H. Wiebe, and P. J. S. Franks. 1991. Micropatchiness, turbulence, and recruitment in plankton. J. Mar. Res. **49**: 109-151.

Denman, K. L. and T. Platt. 1976. The variance spectrum of phytoplankton in a turbulent ocean. J. Mar. Res. **34**: 593-601.

Desiderio, R. A., T. J. Cowles, and J. N. Moum. 1993. Microstructure profiles of laser-induced chlorophyll fluorescence spectra: evaluation of backscatter and forward-scatter fiber-optic sensors. J. Atmos. and Oceanic Technol. **10**: 209-224.

Doubell, M. J., L. Seuront, J. R. Seymour, N. L Patten, and J. G. Mitchell. 2006. High-resolution fluorometer for mapping microscale phytoplankton distributions. Appl. Environ. Microbiol. **72**: 4475-4478.

Doubell, M. J., H. Yamazaki, H. Li, and Y. Kokubu. 2009. An advanced laser-based fluorescence microstructure profiler (TurboMAP-L) for measuring bio-physical coupling in aquatic systems. J. Plankton Res. doi: 10.1093/plankt/fbp092

Durham, W. M., J. O. Kessler, and R. Stocker. 2009. Disruption of vertical motility by shear triggers formation of thin phytoplankton layers. Science **323**: 1067-1070.

Franks, P. J. S. 1995. Thin layers of phytoplankton: a model of formation by near-inertial wave shear. Deep-Sea Res., Part I **42**: 75-91.

Franks, P. J. S. and J. S. Jaffe. 2001. Microscale distributions of phytoplankton: initial results from a two-dimensional imaging fluorometer, OSST. Mar. Ecol. Prog. Ser. **220**: 59-72.

Franks, P. J. S., and J. S. Jaffe. 2008. Microscale variability in the distributions of large fluorescent particles observed *in situ* with a planar laser imaging fluorometer. J. Mar. Syst. **69**: 254-270, doi:10.1016/j.jmarsys.2006.03.027.

Jackson, G. A. 1990. A model of the formation of marine algal flocs by physical coagulation processes. Deep-Sea Res. **37**: 1197-1211.

Jaffe, J. S., P. J. S. Franks, and A. W. Leising. 1998. Simultaneous imaging of phytoplankton and zooplankton distributions. Oceanogr. **11**: 24-29.

Kierstead, H., and L. B. Slobodkin. 1953. The size of water masses containing plankton blooms. J. Mar. Res. **12**: 141-147.

Kiørboe, T. 1997. Small-scale turbulence, marine snow formation, and planktivorous feeding. Sci. Mar. **61**: 141-158.

Lande, R., W. K. W. Li, E. P. W. Horne, and A. M. Wood. 1989. Phytoplankton growth rates estimated from depth profiles of cell concentration and turbulent diffusion. Deep-Sea Res. **36**: 1141-1159.

Leising, A. W., and P. J. S. Franks. 2000. Copepod vertical distribution within a spatially variable food source: a simple foraging-strategy model. J. Plankton Res. **22**: 999-1024.

Malchow, H., S. Petrovskii, and A. Medvinsky. 2001. Pattern formation in models of plankton dynamics: A synthesis. Oceanol. Acta **24**: 479-487.

McManus, M. A., A. L. Alldredge, A. H. Barnard, E. Boss, J. F. Case, T. J. Cowles, P. L. Donaghay, L. B. Eisner, D. J. Gifford, C. F. Greenlaw, C. M. Herren, D. V. Holliday, D. Johnson, S. MacIntyre, D. M. McGehee, T. R. Osborn, M. J. Perry, R. E. Pieper, J. E. B. Rines, D. C. Smith, J. M. Sullivan, M. K. Talbot, M. S.

Twardowski, A. Weidemann, and J. R. Zaneveld. 2003. Characteristics, distribution and persistence of thin layers over a 48 hour period. Mar. Ecol. Prog. Ser. **261**: 1-19.

Menden-Deuer, S. 2008. Spatial and temporal characteristics of plankton-rich layers in a shallow, temperate fjord. Mar. Ecol. Prog. Ser. **355**: 21-30.

Menden-Deuer, S., and Grünbaum, D. 2006. Individual foraging behaviors and population distributions of a planktonic predator aggregating to planktonic thin layers. Limnol. Oceanogr. **51**: 109-116.

Menden-Deuer, S., and K. Fredrickson. 2010. Structure-dependent, protistan grazing and its implication for the formation, maintenance and decline of phytoplankton patches. Mar. Ecol. Prog. Ser. **420**: 57-71.

Mitchell, J. G., H. Yamazaki, L. Seuront, F. Wolk, and H. Li. 2008. Phytoplankton patch patterns: seascape anatomy in a turbulent ocean. J. Mar. Sys. **69**: 247-253.

Oakey, N. S. 1982. Determination of the rate of dissipation of turbulent energy from simultaneous temperature and velocity shear microstructure measurements. J. Phys. Oceanogr. **12**: 256-271.

Osborn, T. R. 1980. Estimates of the local rate of vertical diffusion from dissipation measurements. J. Phys. Oceanogr. **10**: 83-89.

Platt, T. 1972. Local phytoplankton abundance and turbulence. Deep-Sea Res. **19**: 183-187.

Powell, T. M. and A. Okubo. 1994. Turbulence, diffusion and patchiness in the sea. Philos. Trans. R. Soc. of London, Ser. B **343**: 11-18.

Prairie, J. C., P. J. S. Franks, and J. S. Jaffe. 2010. Cryptic peaks: invisible vertical structure in fluorescent particles revealed using a planar laser imaging fluorometer. Limnol. Oceanogr. **55**: 1943-1958.

Rines, J. E. B., P. L. Donaghay, M. M. Dekshenieks, J. M. Sullivan, and M. S. Twardowski. 2002. Thin layers and camouflage: hidden *Pseudo-nitzschia* spp. (Bacillariophyceae) populations in a fjord in the San Juan Islands, Washington, USA. Mar. Ecol. Prog. Ser. **225**: 123-137.

Ryan, J. P., M. A. McManus, J. D. Paduan, and F. P. Chavez. 2008. Phytoplankton thin layers caused by shear in frontal zones of a coastal upwelling system. Mar. Ecol. Prog. Ser. **354**: 21-34.

Ryan, J. P., M. A. McManus, and J. M. Sullivan. 2010. Interacting physical, chemical and biological forcing of phytoplankton thin-layer variability in Monterey Bay, California. Cont. Shelf Res. **30**: 7-16.

Skellam, J. G. 1951. Random dispersal in theoretical populations. Biometrika **38**: 196-218.

Stacey, M. T., M. A. McManus, and J. V. Steinbuck. 2007. Convergences and divergences and thin layer formation and maintenance. Limnol. Oceanogr. **52**: 1523-1532.

Steinbuck, J. V., M. T. Stacey, M. A. McManus, O. M. Cheriton, and J. P. Ryan. 2009. Observations of turbulent mixing in a phytoplankton thin layer: Implications for formation, maintenance, and breakdown. Limnol. Oceanog. **54**: 1353-1368.

Sullivan, J. M., M. S. Twardowski, P. L. Donaghay, and S. A. Freeman. 2005. Use of optical scattering to discriminate particle types in coastal waters. Appl. Opt. **44**: 1667-1680.

Sullivan, J. M., P. L. Donaghay, and J. E. B. Rines. 2010. Coastal thin layer dynamics: consequences to biology and optics. Cont. Shelf Res. **30**: 50-65.

Tennekes, H., and J. L. Lumley. 1972. A First Course in Turbulence. The Massachussets Institute of Technology.

Thessen, A. E., H. A. Bowers, and D. K. Stoecker. 2009. Intra- and interspecies differences in growth and toxicity of Pseudo-nitzschia while using different nitrogen sources. Harmful Algae **8**: 792-810.

Tiselius, P. 1992. Behavior of *Acartia tonsa* in patchy food environments. Limnol. Oceanogr. **37**: 1640-1651.

Wang, Z., and L. Goodman. 2010. The evolution of a thin phytoplankton layer in strong turbulence. Cont. Shelf Res. **30**: 104-118.

Yamazaki, H., J. G. Mitchell, L. Seuront, F. Wolk, and H. Li. 2006. Phytoplankton microstructure in fully developed oceanic turbulence. Geophys. Res. Lett. **33**: L01603, doi:10.1029/2005GL024103.

Yamazaki, H., H. Honma, T. Nagai, M. J. Doubell, K. Amakasu, and M. Kumagai. 2009. Multilayer biological structure and mixing in the upper water column of Lake Biwa during summer 2008. Limnology **11**: 63-70, DOI 10.1007/s10201-009-0288-2

Young, W. R., A. J. Roberts, and G. Stuhne. 2001. Reproductive pair correlations and the clustering of organisms. Nature **412**: 328-331.

Zawada, D. G. 2002. The Application of a Novel Multispectral Imaging System to the *in vivo* Study of Fluorescent Compounds in Selected Marine Organisms. PhD thesis, University of California, San Diego, CA.

CHAPTER V.

THE TRANSITION FROM INDIVIDUAL TO CONTINUOUS SCALES IN ECOLOGY: WHAT IS A PHYTOPLANKTON PATCH?

Abstract

Phytoplankton distributions are often measured using bulk properties such as chlorophyll *a* fluorescence and interpreted as though they were continuous in space. However, at the smallest scales, where phytoplankton interact with each other and their environment, phytoplankton are discrete individuals. At what scale does the transition from continuum to discrete occur? From images of in situ chlorophyll *a* fluorescence we show that peaks in fluorescence at < 1 cm scales are often caused by one large phytoplankter, not an increase in phytoplankton concentration. From our profiles, we can estimate the sample scale above which phytoplankton can be truly measured as a continuum. Whether microscale fluorescence peaks are composed of large individuals or increased concentrations of smaller phytoplankton has implications for all planktonic ecologic processes, including trophic dynamics and carbon cycling.

Introduction

Inferences about organism distributions and dynamics depend on the scales at which they are measured (Wiens 1989; Levin 1992; Dungan et al. 2002). Most if not all fundamental ecological processes begin with interactions among individuals, including sex, infection, predation, aggregation and competition. Even regional and global scale patterns are consequences of the individual interactions that occur at smaller scales. The transition from the scale of individuals to the scale of an assemblage is therefore particularly important because of its effects on larger-scale ecological dynamics. Theoretical studies have shown that, at small scales of observation, the presence of individual organisms can obstruct the interpretation of spatial patterns. At larger scales, the variability from individuals is averaged out, allowing spatial patterns to be more easily interpreted, though losing small-scale information (Rand and Wilson 1995; Keeling et al. 1997; Pascual and Levin 1999; Habeeb et al. 2005). The study of this fundamental scale transition in the plankton has been very limited (Siegel 1998) with no empirical work, despite the fact that it influences the interpretation of all planktonic processes, including carbon cycling and trophic dynamics.

Although sampling the distributions of individuals may be a relatively trivial problem in many terrestrial environments, technological limitations have precluded us from doing the same for the plankton. In plankton ecology, bulk measurements have generally been used to quantify properties and dynamics. With improvements in technology we have access to in situ information at increasingly small spatial scales. The fundamental question then is at what sampling scale do stochastic occurrences of individual organisms begin to represent the observed fluctuations in bulk properties?

Phytoplankton biomass remains difficult to measure in situ, especially at small scales. However, a few studies have used high-resolution sampling devices and observed patchiness in plankton distribution on centimeter scales (Mitchell and Fuhrman 1989; Bjornsen and Nielsen 1991; Waters et al. 2003). The use of fluorometers has allowed a more automated method to measure the induced fluorescence of chlorophyll *a* as a proxy for phytoplankton biomass both in the lab and in situ (Lorenzen 1966; Denman and Gargett 1995). As technology has improved, the spatial resolution of fluorometers, and thus the sample scale, has decreased from liters to milliliters (meters to centimeters). At the microscale (<1 cm) recent instruments have revealed intense peaks in fluorescence (Desiderio et al. 1993; Wolk et al. 2002; Doubell et al. 2006; Yamazaki et al. 2006; Doubell et al. 2009). Although these studies using both fluorometers and high-resolution sampling devices have inferred that phytoplankton are heterogeneously disturbed on scales less than 1 cm, it remains unclear whether the observed microscale patches of chlorophyll *a* fluorescence represent 1) increases in phytoplankton cell abundance, or 2) a large cell in a small sample volume (Figure 5.1). The ecological implications of these two different types of peak are significant.

Using data from an in situ planar laser imaging fluorometer, we show that large individual phytoplankton (e.g., diatoms, dinoflagellates) can often be responsible for microscale patches of chlorophyll *a* fluorescence. Analyzing these data across a range of scales, we calculate a minimum sample scale at which the random fluctuations from individual phytoplankton no longer affects the interpretation of bulk spatial patterns.

Methods

Description of the FIDO-Φ

Images of chlorophyll *a* fluorescence were produced from a free-falling planar laser fluorescence imaging system, FIDO-Φ (Figure 5.2A), deployed in the Santa Barbara Channel in September 2006. A full description of the instrument package and cruise can be found in Prairie et al. (2010). The FIDO-Φ was equipped with a laser and camera, mounted on opposite sides of the frame and both angled downward at 45˚. The sensitive charge-coupled device (CCD) camera (Cooke Sensicam) imaged the laser sheet at a 90˚ angle, with the center of the image plane 60 cm below the bottom of the frame. The dimensions of this imaged region were ~9.8 cm x 13 cm x 0.65 cm. Interposed between the lens and the camera was a filter, which transmitted light at a wavelength range of 670-690 nm (chlorophyll *a* fluorescence). Images of fluorescent particles were taken at a rate of 2 Hz. In this study, the seven drops of the FIDO-Φ which corresponded with concurrent Turbo-MAP-L drops were analyzed (Prairie et al. in press).

The images from the FIDO-Φ had a field of view of ~ 9.8 cm x 13 cm with a resolution slightly less than 100 μm pixel^{-1}. The raw 1040 x 1376 pixel images were processed using MATLAB. The spreading of the laser sheet produces a drop in intensity towards the edges, creating systematic variations of fluorescence signal strength in the images that were corrected before analysis (Zawada 2002). This bias was quantified by averaging all of the fluorescent images from each drop to create a reference, then median filtering this reference to create the beam pattern correction image. All images were then divided by this beam pattern correction image to remove the bias (Franks and Jaffe 2001; Franks and Jaffe 2008). The resultant images show relative fluorescence independent of the incident illumination.

TurboMAP-L microsctructure profiler

The turbulence ocean microstructure acquisition profiler-laser (TurboMAP-L) is a free-falling microstructure profiler which was deployed concurrently with the FIDO-Φ during the 2006 cruise (Doubell et al. 2009; Yamazaki et al. 2009; Prairie et al. in press). The TurboMAP-L carries sensors for chlorophyll *a* fluorescence in addition to physical microstructure measurements such as turbulent shear and temperature gradient. Sample rates range between 64 and 512 Hz for different parameters, and typical profiling speeds are between 0.50-0.80 m s^{-1}. For a full instrument description, see Doubell et al. (2009).

Creating microscale fluorescence profiles from the FIDO-Φ

Vertical profiles of chlorophyll *a* fluorescence were created from images by binning 24 x 23 pixel regions which, given a depth of the laser sheet of 6.5 mm, are equivalent to ~32 μL, the approximate sample volume of the TurboMAP-L (Figure 5.2B). Each square bin was vertically displaced ~21 pixels from the subsequent bin to correspond to the 2 mm vertical sampling resolution of the TurboMAP-L, allowing 43 square bins to fit vertically in each image of the FIDO-Φ. From each of the seven drops of the FIDO-Φ, 5 microscale vertical profiles of chlorophyll *a* fluorescence were created, resulting in 35 profiles totaling 224,695 data points.

The top portions of the FIDO-Φ vertical profiles were cropped to remove error created by movement of internal waves. The cropped profiles were then calibrated to the corresponding TurboMAP-L profiles of fluorescence using a linear correction that minimized the root mean square between profiles from the FIDO-Φ and TurboMAP-L

that were median-filtered to ~20 cm. The resulting median-filtered calibrated FIDO-Φ and TurboMAP-L profiles strongly agreed, with each pair of profiles having a root mean square error less than 7.5% of the maximum fluorescence value (Figure 5.3A). However, at the 2 mm scale at which the TurboMAP-L acquires samples (i.e., not median-filtered), the TurboMAP-L and the calibrated FIDO-Φ profiles do not covary (Figure 5.3B); these small-scale differences are expected because of the gaps in times and locations at which the FIDO-Φ and TurboMAP-L were deployed.

Identifying particles in the FIDO-Φ images

Fluorescent particles were identified in each image by labeling every particle above a fluorescence intensity threshold in the image. This threshold was necessary to eliminate the background fluorescence, and resulted in exclusion of the smaller (less fluorescent) fluorescent particles. Thus, only the largest fluorescent particles (large eukaryotic phytoplankton, chains, and fluorescent aggregates) are included in our profiles of fluorescent particle concentration. Although it is possible to estimate the size of particles greater than 1 pixel in length, it is not possible to determine the size of particles that only occupy 1 pixel in our images, since we know from laboratory tests that fluorescent particles much smaller than the image resolution (~100 μm) can be detected by the camera. Thus, we cannot definitively determine the minimum size of the particles we count in our images. However, from instrument specifications and laboratory experiments (Zawada 2002), we can constrain this value between about 20 and 100 μm.

The fluorescence intensity threshold was determined empirically for each drop to be at least 2 standard deviations above the mean fluorescence value in an image. A bias

in the particle-center frequency distribution required the use of a varying threshold matrix, such that when this threshold matrix was interposed over the images, an even particle-center frequency distribution resulted throughout the field of view of the image. Although this threshold matrix varied from drop to drop, it was kept constant within drops to obtain relative fluorescent particle abundances throughout the water column. The calculation of the threshold matrix required a horizontal cropping of the images, thus requiring no data to be used within 200 pixels of either horizontal edge of an image.

Identifying microscale fluorescence peaks

Microscale fluorescence peaks were identified in each cropped and calibrated profile of fluorescence derived from the FIDO-Φ as any region where the fluorescence exceeded a baseline (Figure 5.4A). The baseline was calculated as a 1 m running mean of each fluorescence profile, which was then smoothed to 50 cm. Peaks that were located at the edges of images (and thus were not fully resolved in the profile of fluorescence) were discounted. In the 35 FIDO-Φ microscale fluorescence profiles, a total of 36,285 peaks were identified.

Regions identified as microscale fluorescence peaks were then located in the corresponding FIDO-Φ images to determine whether the peak was formed by one or more large fluorescent particles (Figure 5.1B2) or by an increase in the concentration of smaller phytoplankton (Figure 5.1B1). We identified large fluorescent particles as pixels in the images that were above the set fluorescence threshold as described in the previous section (Figure 5.4); parts of images below this threshold represent small fluorescent particles (Prairie et al. 2010). These large fluorescent particles included large eukaryotic

phytoplankton, cell chains, and fluorescent aggregates; small fluorescent particles included small phytoplankton such as cyanobacteria and eukaryotic picoautotrophs. In addition, the major axis length and area of each large fluorescent particle were recorded.

Calculating the fractional change in fluorescence from individual particles

To determine the effect of individual particles on changes in bulk fluorescence, we ran Monte Carlo simulations using data from the FIDO-Φ to calculate the fractional change in fluorescence that would occur when a single large fluorescent particle was added to a sample volume of a given size, ranging from less than 1 μL to greater than 5 mL. Each simulation consisted of adding the fluorescence of one particle from a probability density function of over 100,000 particles to a background fluorescence value. The background fluorescence value was calculated from the median fluorescence value of a single pixel in a FIDO-Φ image (averaged for all images in a drop), scaled to the size of the given sample volume. To produce mean, median, and 95th percentile curves, we averaged these values from 100 runs of 1000 Monte Carlo simulations each.

Results and Discussion

Composition of Microscale Fluorescence Peaks

To determine the composition of microscale fluorescence peaks, we determined the percentage of peaks that contained at least one large fluorescent particle within the bin at the peak maximum and compared it to the percentage of bins overall that contained at least one large fluorescent particle (Table 5.1). The results show that the majority of

the peaks were caused by the presence of one or more large phytoplankton or aggregates: of the 36,285 microscale fluorescence peaks, 63.2% contained at least one particle. This was significantly higher than the percentage of all sample bins which contained at least one large particle (24.2%), as determined by a two-sample *t* test ($p<0.0001$). Furthermore, we determined the effect of large fluorescent particles when sampling fluorescence at this scale by calculating the percentage of bins with large fluorescent particles that were found within peaks. This analysis illustrated when a large fluorescent particle was present in a sample bin, it most often caused a peak: 64.8% of all bins that contained at least one particle were located within a peak. This was significantly higher than the percentage of bins overall that were located within peaks (31.4%) as determined by a two-sample *t* test ($p<0.0001$).

Our observations clearly show that the majority of the microscale fluorescence peaks were created by the presence of one or more large fluorescent particles. However, peaks most often did not consist of more than one of these particles. The average number of large fluorescent particles within microscale fluorescence peaks (including peaks that spanned more than one sample bin) was 1.25 particles (Table 5.2). The average length of large fluorescent particles within peaks was 5.95 pixels (corresponding to ~535 μm; Table 5.3) while the average area of large fluorescent particles within peaks was 14.58 pixels^2 (corresponding to ~118098 μm^2, Table 5.4). Water samples acquired at the time of image acquisition showed that many large individual phytoplankton (consisting primarily of chain-forming diatoms) were present, thus accounting for many of the large fluorescent particles in our images (Prairie et al. 2010). However, the average size of large fluorescent particles within microscale fluorescence peaks suggests that in addition

to large individual phytoplankton and phytoplankton chains, many of the large fluorescent particles were likely aggregates (i.e., marine snow).

The number and characteristics of particles within microscale fluorescence peaks changed with the relative fluorescence intensity of a peak (i.e., the height of a peak) (Figure 5.5). Peak intensity was defined as the ratio of fluorescence at the peak maximum to the baseline – thus peak intensity ≥ 1. To compare peak intensity with particle data, peaks were divided into four categories of increasing peak intensity (Table 5.5), and differences in particle properties at the peak maximum were calculated using two-sample *t* tests between each pair of peak intensity categories. The probability that a microscale fluorescence peak contained at least one large fluorescent particle significantly increased as peak intensity increased ($p<0.0001$). The average number of large fluorescent particles within the peak maximum was also found to significantly increase with peak intensity ($p<0.0001$). However, even for the peaks of greatest intensity, the average number of large fluorescent particles within the peak maximum was only 1.60. By contrast, both the average length and area of particles within the peak maximum increased significantly with peak intensity ($p<0.0001$). This suggests that the most intense microscale fluorescence peaks do not indicate the presence of more large fluorescent particles, but rather are likely the result of an extremely large fluorescent particle (such as a marine snow particle).

The number and characteristics of large fluorescent particles within microscale fluorescence peaks were also compared to the width of peaks, defined as the number of points in the fluorescence profile in which the peak continuously exceeded the baseline (where one point ~ 2 mm). Just as with peak intensity, peaks were divided into four

categories of increasing peak width (Table 5.6), and differences in particle properties within the entire region occupied by a peak were calculated using two-sample *t* tests between each pair of peak width categories. The average number of large fluorescent particles within peaks significantly increased with peak width ($p < 0.0001$ in all cases, except $p = 0.02$ in the *t* test between the last two width categories; Figure 5.6A). However, the average area and length of large fluorescent particles within peaks did not demonstrate a monotonic relationship with peak width (Figures 5.6B and 5.6C). This implies that wider microscale fluorescent peaks are more likely to be composed of a greater number of larger fluorescent particles, but not necessarily larger than average particles.

The transition scale from individuals to a continuum

The above analyses have shown that sampling at very small scales, individual fluorescent particles can strongly influence the observed spatial patterns. Previous theoretical predictions showed that at small scales, stochastic noise from individuals makes it difficult or impossible to interpret the underlying spatial pattern; however, above a certain scale, this stochasticity becomes negligible allowing generalizations about spatial patterns to be made (Keeling et al. 1997; Pascual and Levin 1999; Habeeb et al. 2005). Here we aimed to determine the sample scale required so that the stochastic occurrence of individual particles would not contribute significantly to the observed fluorescence signal. In other words, above what scale can phytoplankton be measured as a continuum, unaffected by the presence of individuals? Since phytoplankton live in a 3D world, it is appropriate to define sample scale as a sample volume. To determine this

important transition scale, we ran Monte Carlo simulations calculating the fractional change in fluorescence that occurred when a single large particle was added to sample volumes ranging from less than 1 μL to greater than 5 mL (see Methods). The results show that as sample volume increased, the fluorescence of an individual particle had a lesser affect on the change in total fluorescence, eventually becoming negligible (Figure 5.7). When the presence of an individual no longer has a significant effect on the bulk measurement, the variable can then be interpreted as continuous.

The relationship between sample volume and the relative contribution of individual particles to bulk fluorescence provides the information to define a critical sample scale given a set level of acceptable error (Figure 5.7). For example, using the criterion that a single large particle should cause less than a 5% increase over the background fluorescence on average, the sample volume needs to be at least 0.23 mL. However, if we are to apply more stringent conditions on what we consider a continuum, requiring that 95% of the time a large particle will cause less than a 5% increase over background fluorescence levels, then a 0.86 mL sample volume is needed. Although these values are calculated for the specific conditions observed during our sampling, they provide estimates that demonstrate that individual phytoplankton affect bulk measurements at a broad range of small scales, including those resolved by most microscale fluorometers (e.g., the RSVP, Desiderio et al. 1993; the TurboMAP, Wolk et al. 2002 and Yamazaki et al. 2006; the FluoroMAP, Doubell et al. 2006; the TurboMAP-L, Doubell et al. 2009). Furthermore, this analysis shows that with knowledge of the fluorescent particle composition at the time of sampling, one can accurately determine the predicted effect of individual particles on bulk measurements at any scale.

Implications of plankton distributions at the microscale

Global manifestations of ecological phytoplankton dynamics originate from interactions at the microscale – the scale of the individual. Individual phytoplankton interact with bacteria, grazers, and each other to influence fundamental ecosystem processes. However, this study has demonstrated that the patterns observed when measuring phytoplankton distributions at the microscale using traditional methods can be strongly distorted by the presence of large individual fluorescent particles. Thus, when measuring phytoplankton patchiness at these scales using fluorescence or other bulk measurements, it would be impossible to distinguish whether an observed patch is due to a significant increase in the number of small phytoplankton or the presence of one large phytoplankter or marine snow particle (Figure 5.1). The question is, do these different types of fluorescence patches have any ecological significance? In terms of microscale implications for both carbon cycling and trophic dynamics, the answer is certainly yes.

Large marine snow particles (aggregates) have been shown to play an important role in the biological pump (Alldredge and Silver 1988; Turner 2002). Because marine snow sinks rapidly through the water column, its presence can greatly increase vertical carbon flux (Shanks and Trent 1980; Turner 2002; McDonnell and Buesseler 2010). Additionally, the formation of these aggregates strongly depends on the size and abundance of particles in the water column (Jackson 1990). Thus, a microscale patch composed of one large aggregate may contribute much more to vertical carbon export compared to a patch of many small phytoplankton.

The composition of microscale patches may also strongly influence trophic dynamics on these scales. Laboratory studies have demonstrated that mesozooplankton such as copepods have foraging behaviors that allow them to seek out and remain in regions of high prey concentration (Bird and Kitting 1982; Tiselius 1992). It is unlikely that large, rare, individual phytoplankton appear as a prey patch for these larger grazers. However, this is not to imply that individual phytoplankton can never act as patches. Many studies have now shown that bacteria may be able to accumulate on a single particle; marine snow particles can act as hot spots for bacterial activity (Mitchell et al. 1985; Azam and Long 2001; Kiorboe and Jackson 2001; Stocker et al. 2008). Thus, the patch dynamics at this scale strongly depend on the organism – what appears as a patch to bacteria may be only a single prey item for a copepod. Although there is much more to learn about microscale plankton foraging dynamics, the composition of microscale patches of fluorescence clearly has implications for the organisms that rely on phytoplankton.

The significance of individual phytoplankton to marine ecosystem dynamics motivates the importance of finding methods to measure microscale phytoplankton patterns in situ. However, as we attempt to measure phytoplankton distributions at smaller and smaller scales, the patterns are obfuscated by the scale at which we observe them. Although the result that spatial patterns are scale-dependent is not new in ecology, it is necessary to learn how information is passed from one scale to another in order to interpret ecological patterns (Wiens 1989; Levin 1992; Dungan 2002). In many disciplines, such as landscape ecology, there have been great strides in quantifying how patterns change with the scale of observation and analysis (Turner et al. 1989; Wu 2004),

but the same has not been true for microscale phytoplankton distributions. Advances in technology have recently allowed the measurement of phytoplankton properties at the microscale. However, a lack of consideration for the scale-dependence of pattern has hindered the interpretation of true microscale dynamics. Here we have made a first step towards quantifying this phytoplankton scale-dependence by using in situ microscale images of phytoplankton to determine the scale above which individuals no longer significantly affect observations of bulk spatial patterns. Although the findings are specific to the location and time of this study, the general conclusions demonstrate that individuals and community composition have a significant impact on observed bulk phytoplankton patterns at a broad range of small scales. Focusing on individual measurements rather than bulk properties may be the only way to determine the microscale phytoplankton patterns that are critical to global ocean processes.

Acknowledgements

We thank F. Simonet, P. Roberts, and Y. Platoshyn for their help in designing, building, and deploying the free-fall imaging device for observing phytoplankton (FIDO-Φ), and E. Karaköylü and A. Lucas for their help configuring the auxiliary instrumentation. We thank E. Daniels and C. Anderson for the shipboard conductivity-temperature-depth (CTD) deployments and processing chlorophyll samples and H. McClendon for analyzing samples for species composition. In addition, we thank Y. Kokubu (TUMSAT), H. Li (JEF Advantech) and T. Horiuchi (JEF Advantech) in addition to the students in the laboratory of H. Yamazaki at the Toyko University of Marine Science and Technology who helped collect and process the TurboMAP-L data. This work was supported by the U.S. Office of Naval Research grant N00014-06-1-0304, the National Science Foundation grant OCE 08-25154, and the Grant-in-Aid for Science Research (B2) 20340127.

Chapter 5, in part, is currently being prepared for submission for publication of the material. Prairie, J. C., Franks, P. J. S., Jaffe, J. S., Doubell, M. J., and Yamazaki, H. The dissertation author was the primary investigator and author of this paper.

Table 5.1 Description of the microscale fluorescence profiles created from each drop of the FIDO-Φ on the 2006 cruise.

FIDO-Φ drop number	Total data points in microscale fluorescence profiles	Number of data points within a peak	Number of data points containing at least one particle	Number of data points within a peak and containing at least one particle	Total number of peaks	Number of peaks with at least one particle within the peak maximum
Drop 3-1	34117	8329	9664	6508	4961	4338
Drop 3-2	18244	5130	4005	2893	2532	1853
Drop 4-1	34883	14566	2181	1821	5817	1203
Drop 4-2	72972	26279	15407	10332	12825	6836
Drop 7-1	23297	6209	8798	5089	3721	3175
Drop 7-2	36782	8952	13612	7979	5768	5199
Drop 8-2	4400	1091	608	522	661	338
Total	224695	70556	54275	35144	36285	22942

Table 5.2 Average and median number of particles found within all sample bins and within microscale peaks of from each drop of the FIDO-Φ on the 2006 cruise.

FIDO-Φ drop number	Average number of particles in each sample bin	Average number of particles in each microscale peak	Median number of particles in each sample bin	Median number of particles in each microscale peak
Drop 3-1	0.3511	1.4773	0	1
Drop 3-2	0.2661	1.2243	0	1
Drop 4-1	0.0803	0.3534	0	0
Drop 4-2	0.3007	1.0901	0	1
Drop 7-1	0.5686	1.9535	0	1
Drop 7-2	0.5420	1.9012	0	1
Drop 8-2	0.1677	0.7761	0	1
Total	0.3360	1.2461	0	1

Table 5.3 Average and median major axis lengths of particles from each drop of the FIDO-Φ on the 2006 cruise. Lengths are given in pixels, where 1 pixel ~ 90 μm.

FIDO-Φ drop number	Average length of all particles (pixels)	Average length of particles within microscale peaks (pixels)	Median length of all particles (pixels)	Median length of particles within microscale peaks (pixels)
Drop 3-1	4.3246	5.2778	3.8791	5.0094
Drop 3-2	4.7052	5.6629	4.0537	5.0966
Drop 4-1	4.4664	5.1008	3.4976	4.3817
Drop 4-2	4.5071	5.3203	3.8541	4.8661
Drop 7-1	4.6825	5.9682	3.8541	5.2510
Drop 7-2	5.8405	7.3499	5.0667	6.7300
Drop 8-2	5.8546	7.2957	4.4645	5.6272
Total	4.8854	5.9457	4.1633	5.2985

Table 5.4 Average and median area of particles from each drop of the FIDO-Φ on the 2006 cruise. Areas are given in pixels^2, where 1 pixel^2 ~8100 μm^2.

FIDO-Φ drop number	Average area of all particles (pixels^2)	Average area of particles within microscale peaks (pixels^2)	Median area of all particles (pixels^2)	Median area of particles within microscale peaks (pixels^2)
Drop 3-1	10.6069	14.8612	6.0	10.5
Drop 3-2	10.0651	13.4761	5.5	9.0
Drop 4-1	7.3890	8.9193	4.0	6.0
Drop 4-2	8.0582	10.5412	5.5	8.5
Drop 7-1	9.4150	13.8850	5.0	9.0
Drop 7-2	14.2403	21.3625	8.0	15.5
Drop 8-2	11.6260	15.1715	5.0	7.5
Total	10.4721	14.5836	6.0	10.0

Table 5.5 Number of microscale fluorescence peaks and their particle composition categorized by peak intensity among all drops of the FIDO-Φ.

Peak Intensity	Total number of peaks of given peak intensity	Fraction of peaks that contained at least one particle	Average number of particles within peaks	Average length of particles within peaks (pixels)	Average area of particles within peaks ($pixels^2$)
Peak intensity < 1.1	18640	0.36	0.47	4.05	6.10
Peak intensity ≥ 1.1 and < 1.25	7208	0.84	1.23	5.13	9.22
Peak intensity ≥ 1.25 and < 1.5	4878	0.97	1.53	6.47	14.33
Peak intensity ≥ 1.5	5559	1.00	1.60	8.63	30.29

Table 5.6 Number of microscale fluorescence peaks and their particle composition categorized by peak width among all drops of the FIDO-Φ.

Peak width	Total number of peaks of given peak intensity	Average number of particles within peaks	Average length of particles within peaks (pixels)	Average area of particles within peaks (pixels^2)
Peak width = 1 point	21318	0.90	5.60	12.04
Peak width = 2 points	8294	1.47	6.29	15.80
Peak width = 3 points	3046	1.98	6.23	15.66
Peak width ≥ 4 points	3627	2.14	6.05	18.12

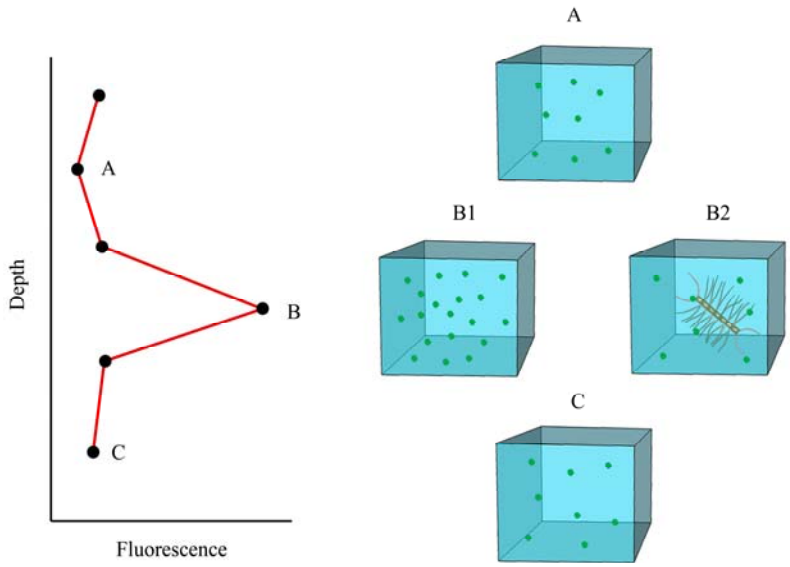

Figure 5.1 A schematic showing two different scenarios for the composition of a microscale fluorescence peak. On the left is a schematic profile of fluorescence showing a microscale peak. Points labeled A and C represent regions of low background levels of fluorescence, while the point labeled B represents a region of increased fluorescence. On the right shows hypothetical microscale sample volumes corresponding to the numbered points on the profile on the left. In sample volumes A and C, corresponding to low levels of fluorescence, we may expect to find a background concentration of small phytoplankton (e.g., cyanobacteria), as represented by the green spheres. However there are two likely scenarios for the composition of a microscale peak as indicated by point B on the profile: the sample volume may be composed of a higher concentration of the small phytoplankton as (B1) or the sample volume may have the same background concentration of small phytoplankton as in A and C, but contain a large eukaryotic phytoplankton (here shown as a diatom chain, B2).

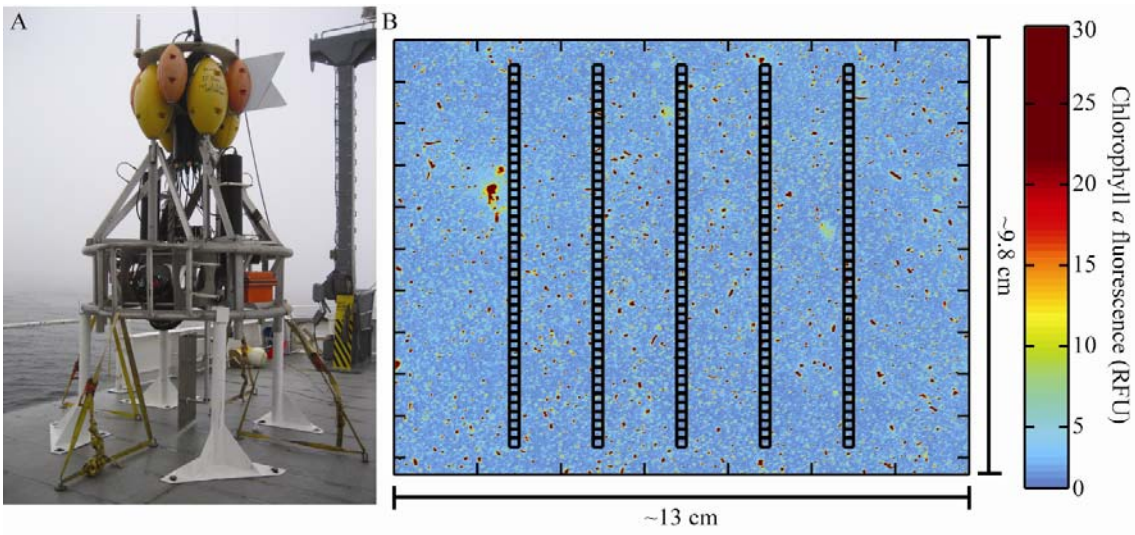

Figure 5.2 (A) The FIDO-Φ on deck of the R/V *Wecoma*. (B) An example of an image from the FIDO-Φ. The color bar represents chlorophyll *a* fluorescence with strongly fluorescent particles appearing in red. The black boxes represent the binning schematic used to create the microscale vertical profiles of chlorophyll *a* fluorescence. Each bin (black box) encompasses a volume of ~32 μL.

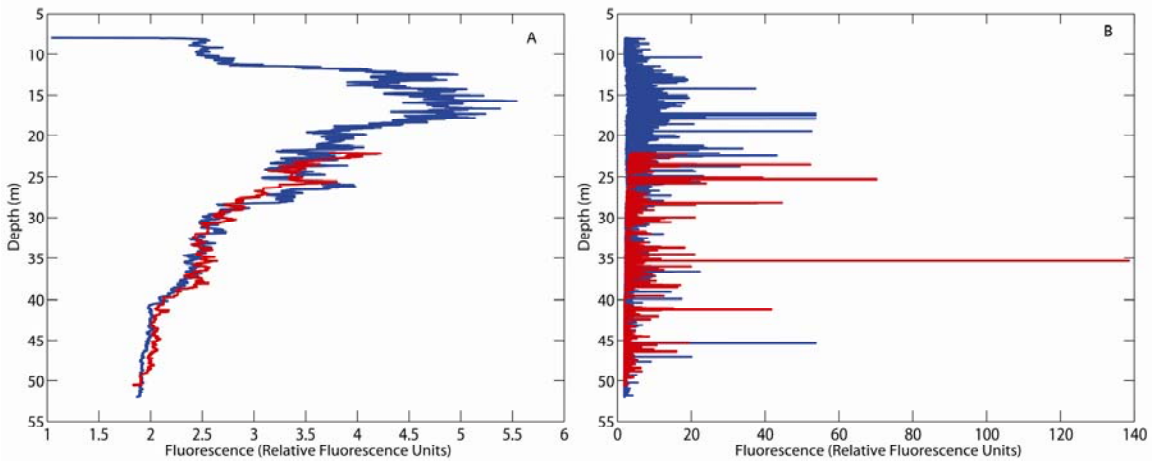

Figure 5.3 Comparison of corresponding profiles of chlorophyll *a* fluorescence from the FIDO-Φ (Drop 7-2) and the TurboMAP-L (Drop 8-2). (A) Profiles of fluorescence from the TurboMAP-L (blue line) and FIDO-Φ (red line) smoothed to 20 cm. (B) Unsmoothed profiles of fluorescence from the TurboMAP-L (blue line) and FIDO-Φ (red line).

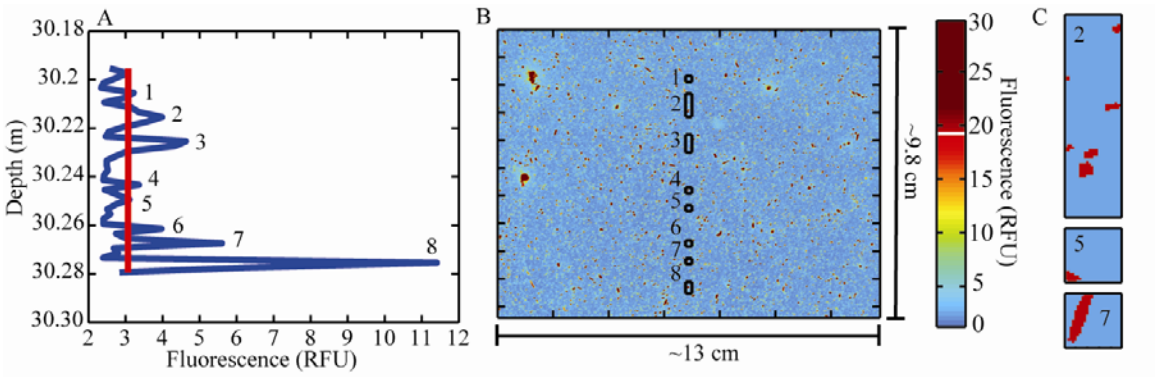

Figure 5.4 (A) An example of a microscale profile of fluorescence from one image of the FIDO-Φ from Drop 7-2. Fluorescence is shown in blue and the baseline is shown in red. Eight microscale peaks in fluorescence (defined as regions where the fluorescence exceeds the baseline) are indicated by numerals. (B) The corresponding image to the microscale fluorescence profile shown in A. The color bar shows relative fluorescence intensities. The white bar indicates the fluorescence threshold for this profile; regions where the fluorescence exceeds this threshold are counted as large fluorescent particles. The areas of the image that correspond to the eight peaks identified in the fluorescence profile in A are boxed in black with corresponding numbers. (C) Insets of the image shown in B corresponding to three of the microscale peaks (2, 5, and 7) showing the composition of a few example peaks ranging in intensity and width. The image insets are shown in binary, such that the large fluorescent particles appear in red and the background is shown in blue.

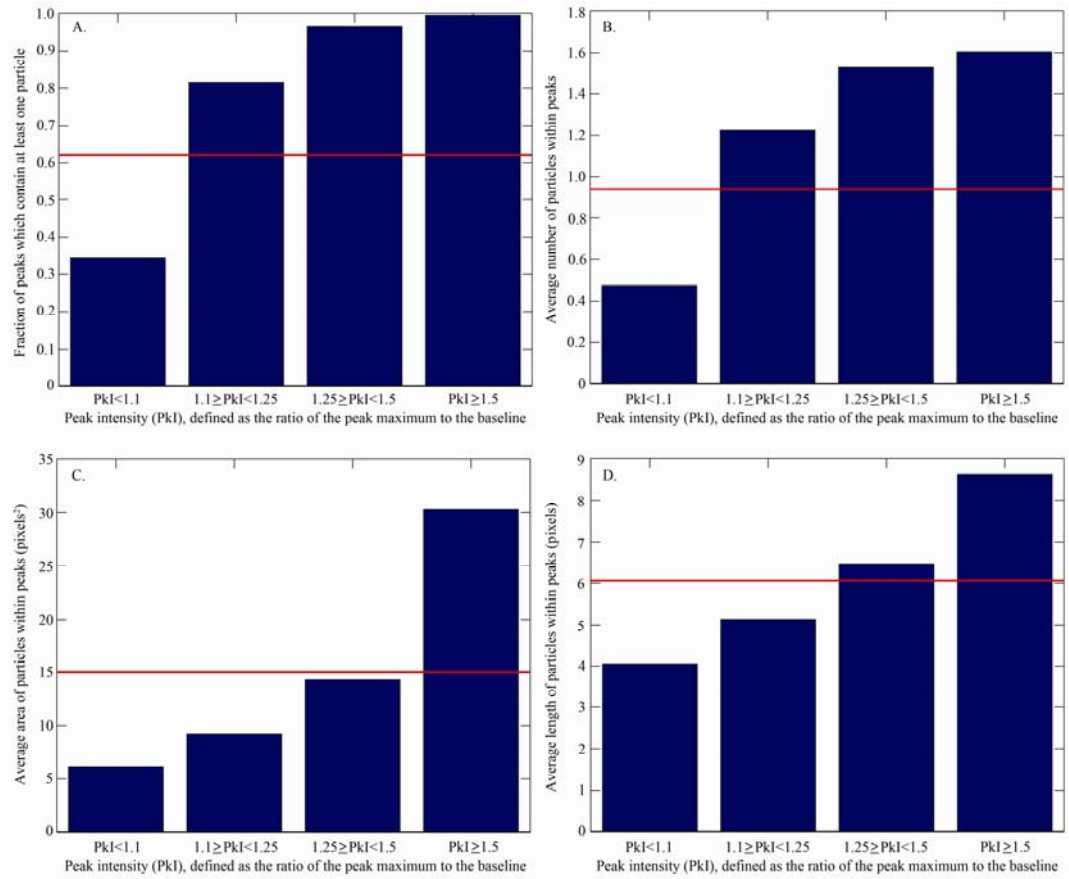

Figure 5.5 (A) The fraction of microscale fluorescence peaks of a given intensity which contain at least one particle for all fluorescence profiles of the FIDO-Φ. Peak intensity (PkI) is defined as the ratio of the peak maximum to the baseline. The red line indicates the fraction of all microscale fluorescence peaks which contain at least one particle. (B) The average number of particles within microscale fluorescence peaks of a given intensity. The red line indicates the average number of particles per peak for all peaks. (C) The average area of particles within microscale fluorescence peaks of a given intensity. The red line indicates the average area of particles for all peaks. (D) The average length of particles within microscale fluorescence peaks of a given intensity. The red line indicates the average length of particles for all peaks.

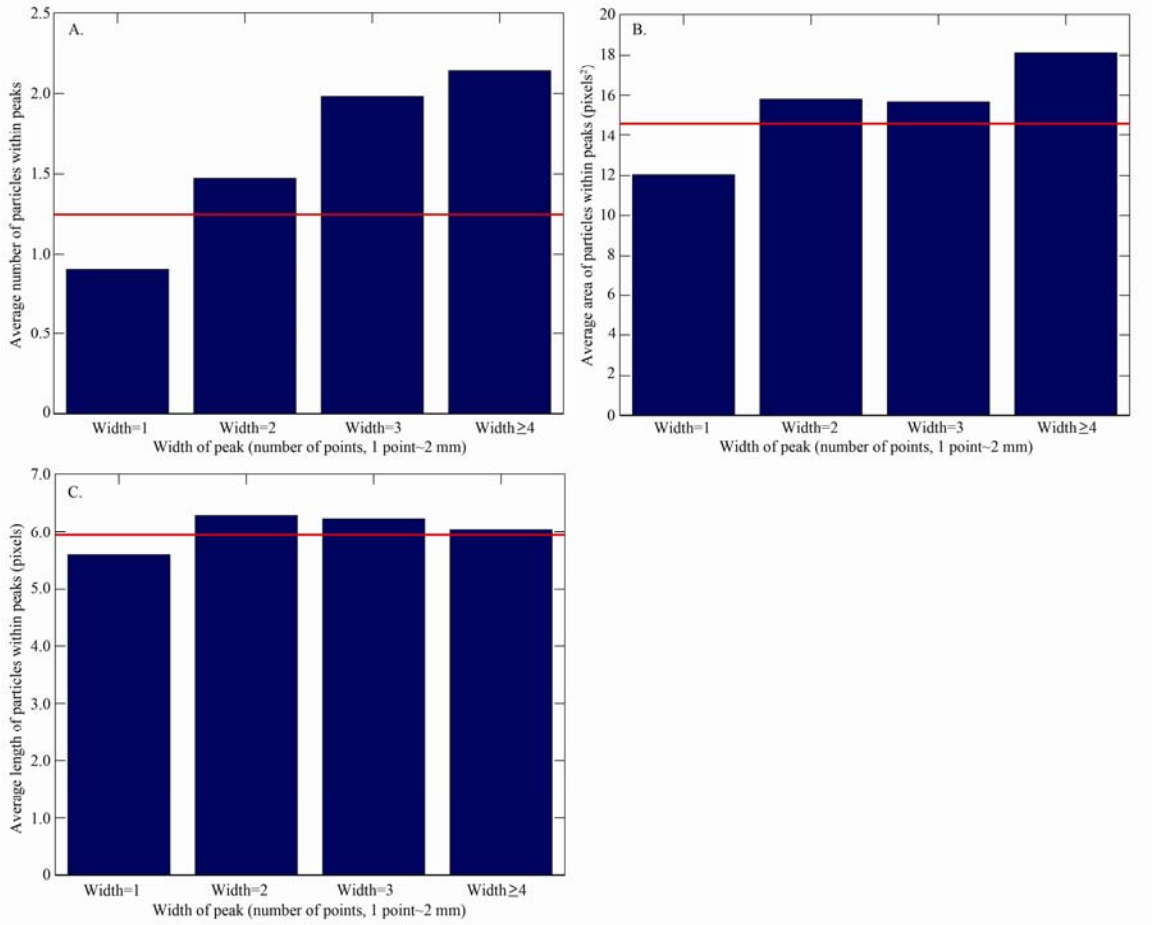

Figure 5.6 (A) The average number of particles within microscale fluorescence peaks of a given width for all fluorescence profiles of the FIDO-Φ. Width is defined as the number of continuous points in the fluorescence profile that the peak exceeds the baseline, where a point in the profile ~2 mm. The red line indicates the average number of particles per peak for peaks of all widths. (B) The average area of particles within microscale fluorescence peaks of a given width. The red line indicates the average area of particles for peaks of all widths. (C) The average length of particles within microscale fluorescence peaks of a given width. The red line indicates the average length of particles for peaks of all widths.

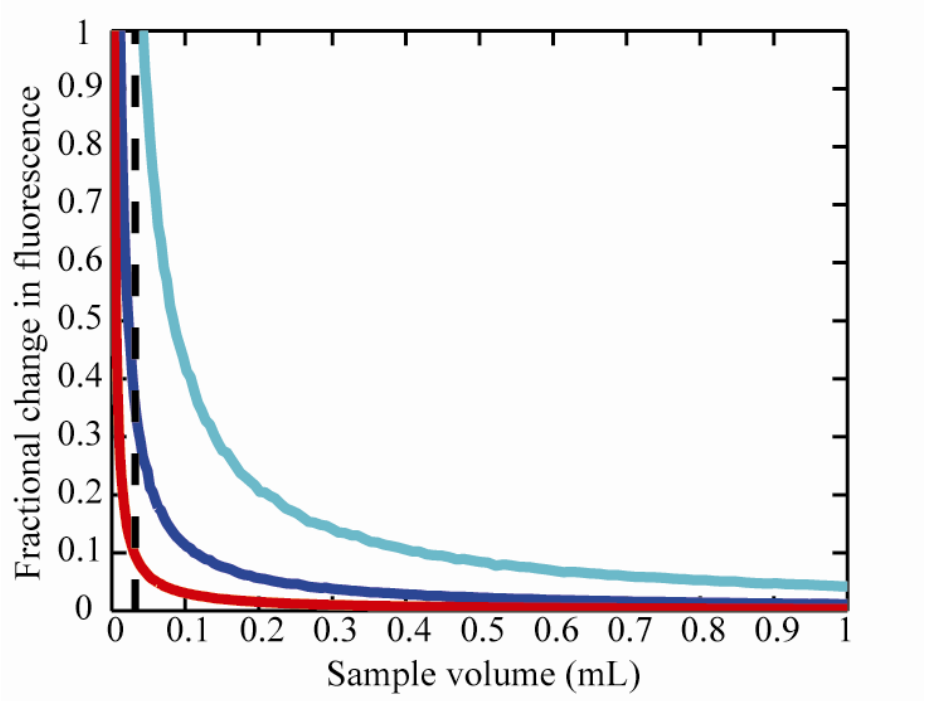

Figure 5.7 Relationship of sample volume size and the fractional change in fluorescence that occurs when one large fluorescent particle is added to that sample volume. Blue line shows the mean fractional change, red line shows the median fractional change, and the cyan line shows the 95th percentile fractional change at each sample volume respectively. Mean, median, and 95th percentile values were calculated by averaging these values from 100 runs of 1000 Monte Carlo simulations each using data from the FIDO-Φ images. In each of the Monte Carlo simulations, the fluorescence of a single large fluorescent particle was added to a background fluorescence value for the given sample volume. The vertical black dashed line indicates the sample volume of the TurboMAP-L (~32 μL), as used to calculate microscale fluorescence profiles in this study.

References

Alldredge, A. L., and M. W. Silver. 1988. Characteristics, dynamics and significance of marine snow. Prog. Oceanogr. **20**: 41-82.

Azam, F., and R. A. Long. 2001. Oceanography-Sea snow microcosms. Nature **414**: 495-498.

Bird, J. L., and C. L. Kitting. 1982. Laboratory studies of a marine copepod (*Temora turbinata* dana) tracking dinoflagellate migrations in a water column. Contributions in Marine Science **25**: 27-44.

Bjornsen, P. K., and T. G. Nielsen. 1991. Decimeter scale heterogeneity in the plankton during a pycnocline bloom of *Gyrodinium aureolum*. Marine Ecology Progress Series **73**: 263-267.

Denman, K. L., and A. E. Gargett. 1995. Biological-physical interactions in the upper ocean: the role of vertical and small scale transport processes. Annu. Rev. Fluid Mech. **27**: 225-255.

Desiderio, R. A., T. J. Cowles, and J. N. Moum. 1993. Microstructure profiles of laser-induced chlorophyll fluorescence spectra: evaluation of backscatter and forward-scatter fiber-optic sensors. J. Atmos. Ocean. Technol. **10**: 209-224.

Doubell, M. J., L. Seuront, J. R. Seymour, N. L Patten, and J. G. Mitchell. 2006. High-resolution fluorometer for mapping microscale phytoplankton distributions. *Appl. Environ. Microbiol.* **72**: 4475-4478.

Doubell, M. J., H. Yamazaki, H. Li, and Y. Kokubu. 2009. An advanced laser-based fluorescence microstructure profiler (TurboMAP-L) for measuring bio-physical coupling in aquatic systems. J. Plankton Res. **31**: 1441-1452.

Dungan, J. L., J. N. Perry, M. R. T. Dale, P. Legendre, S. Citron-Pousty, M.-J. Fortin, A. Jakomulska, M. Miriti, and M. S. Rosenberg. 2002. A balanced view of scale in spatial statistical analysis. Ecography **25**: 626-640.

Franks, P. J. S., and J. S. Jaffe. 2001. Microscale distributions of phytoplankton: initial results from a two-dimensional imaging fluorometer, OSST. Marine Ecology Progress Series **220**: 59-72.

Franks, P. J. S., and J. S. Jaffe. 2008. Microscale variability in the distributions of large fluorescent particles observed *in situ* with a planar laser imaging fluorometer. Journal of Marine Systems **69**: 254-270, doi:10.1016/j.jmarsys.2006.03.027.

Habeeb, R. L., J. Trebilco, S. Wotherspoon, and C. R. Johnson. 2005. Determining natural scales of ecological systems. Ecol. Monogr. **75**: 467-487.

Jackson, G. A. 1990. A model of the formation of marine algal flocs by physical coagulation processes. Deep-Sea Res. **37**: 1197-1211.

Keeling, M. J., I. Mezic, R. J. Hendry, J. McGlade, and D. A. Rand. 1997. Characteristic length scales of spatial models in ecology via fluctuation analysis. Philos. Trans. R. Soc. London Ser. B **352**: 1589-1601.

Kiørboe, T., and G. A. Jackson. 2001. Marine snow, organic solute plumes, and optimal sensory behavior of bacteria. Limnol. Oceanogr. **46**: 1309-1318.

Levin, S. A. 1992. The problem of pattern and scale in ecology. Ecology **73**: 1943-1967.

Lorenzen, C. J. 1966. A method for the continuous measurement of in vivo chlorophyll concentration. Deep-Sea Res. **13**: 223-227.

McDonnell, A. M. P., and K. O. Buesseler. 2010. Variability in the average sinking velocity of marine particles. Limnology and Oceanography **55**: 2085-2096.

Mitchell, J. G., and J. A. Fuhrman. 1989. Centimeter scale vertical heterogeneity in bacteria and chlorophyll *a*. Marine Ecology Progress Series **54**: 141-148.

Mitchell, J. G., A. Okubo, and J. A. Fuhrman. 1985. Microzones surrounding phytoplankton form the basis for a stratified marine microbial ecosystem. Nature **316**: 58-59.

Pascual, M., and S. A. Levin. 1999. From individual to population densities: searching for the intermediate scale of nontrivial determinism. Ecology **80**: 2225-2236.

Prairie, J. C., P. J. S. Franks, and J. S. Jaffe. 2010. Cryptic peaks: invisible vertical structure in fluorescent particles revealed using a planar laser imaging fluorometer. Limnol. Oceanogr. **55**: 1943-1958.

Prairie, J. C., P. J. S. Franks, J. S. Jaffe, M. J. Doubell, and H. Yamazaki. *in press*. Physical and biological controls of vertical gradients in phytoplankton. Limnology and Oceanography: Fluids and Environments.

Rand, D. A., and H. B. Wilson. 1995. Using spatio-temporal chaos and intermediate-scale determinism to quantify spatially extended ecosystems. Proc. R. Soc. London Ser. B **259**: 111-117.

Shanks, A. L., and J. D. Trent. 1980. Marine snow: sinking rates and potential role in vertical flux. Deep-Sea Res. **27A**: 137-143.

Siegel, D. A. 1998. Resource competition in a discrete environment: why are plankton distributions paradoxical? Limnology and Oceanography **46**: 1133-1146.

Stocker, R., R. Seymour, A. Samadani, D. E. Hunt, and M. F. Polz. 2008. Rapid chemotactic response enables marine bacteria to exploit ephemeral microscale nutrient patches. Proc. Natl. Acad. Sci. U.S.A. **105**: 4209-4214.

Tiselius, P. 1992. Behavior of *Acartia tonsa* in patchy food environments. Limnol. Oceanogr. **37:** 1640-1651.

Turner, J. T. 2002. Zooplankton fecal pellets, marine snow and sinking phytoplankton blooms. Aquatic Microbial Ecology **27**: 57-102.

Turner, M. G., R. V. O'Neill, R. H. Gardner, and B. T. Milne. 1989. Effects of changing spatial scale on the analysis of landscape pattern. Landscape Ecology **3**: 153-162.

Waters, R. L., J. G. Mitchell, and J. Seymour. 2003. Geostatistical characterisation of centimetre-scale spatial structure of *in vivo* fluorescence. Marine Ecology Progress Series **251**: 49-58.

Wiens, J. A. 1989. Spatial scaling in ecology. Funct. Ecol. **3**: 385-397.

Wolk, F., H. Yamazaki, L. Seuront, and R. G. Lueck. 2002. A new free-fall profiler for measuring biophysical microstructure. J. Atmos. Ocean. Technol. **19**: 780-793.

Wu, J. 2004. Effects of changing scale on landscape pattern analysis: scaling relations. Landscape Ecology **19**: 125-138.

Yamazaki, H., J. G. Mitchell, L. Seuront, F. Wolk, and H. Li. 2006. Phytoplankton microstructure in fully developed oceanic turbulence. Geophys. Res. Lett. **33**: L01603.

Yamazaki, H., H. Honma, T. Nagai, M. J. Doubell, K. Amakasu, and M. Kumagai. 2009. Multilayer biological structure and mixing in the upper water column of Lake Biwa during summer 2008. Limnology, DOI 10.1007/s10201-009-0288-2

Zawada, D. G. 2002. The Application of a Novel Multispectral Imaging System to the *in vivo* Study of Fluorescent Compounds in Selected Marine Organisms. PhD thesis, University of California, San Diego, CA.

CHAPTER VI.

CONCLUSIONS

Several aspects of small-scale vertical phytoplankton distributions were explored using a combination of field work, image analysis and theory. Insights were made in our understanding of phytoplankton distributions, the mechanisms controlling these distributions, and the implications of phytoplankton distributions to ecological processes. However, by considering these chapters as a whole, the individual conclusions can be placed in a broader context, allowing a deeper understanding of small-scale phytoplankton dynamics.

Data from a free-falling planar laser imaging fluorometer (FIDO-Φ) allowed me to quantify vertical phytoplankton distributions on spatial scales on the order of a meter and less. Although some of the results agreed with findings from previous studies, novel results provided a different interpretation of previously observed patterns. In Chapter 2, the observation of meter-scale peaks in bulk fluorescence is consistent with the recent discovery that phytoplankton thin layers may be common in coastal waters (Cowles et al. 1998; Dekshenieks et al. 2001; McManus et al. 2003). However, our results suggest that not only total phytoplankton biomass but also the size composition of phytoplankton may vary significantly on meter scales, producing peaks of specific groups of phytoplankton that are undetectable using bulk measurements (Chapter 2, Chapter 3). This is supported by studies that have reported phytoplankton structure and layers with phytoplankton compositions different than that of the rest of the water column (Rines et al. 2002; Franks and Jaffe 2008). In Chapter 5, I investigated vertical phytoplankton distributions on

centimeter scales, yielding very different conclusions from other in situ studies at these scales. Although many previous studies have observed centimeter-scale variability in chlorophyll *a* or bulk fluorescence (Mitchell and Fuhrman 1989; Desiderio et al. 1993; Wolk et al. 2002; Waters et al. 2003; Doubell et al. 2006; Yamazaki et al. 2006; Doubell et al. 2009), I have shown that microscale peaks can be caused by the presence of a single large phytoplankter or fluorescent aggregate.

In this dissertation, I have also made progress in elucidating the factors that control heterogeneity in vertical phytoplankton distributions. In Chapter 2, correlations between phytoplankton peaks and physical variables supported previous work showing similar patterns (Dekshenieks et al. 2001; McManus et al. 2003; Ryan et al. 2008; Steinbuck et al. 2009). However, physical parameters alone appeared to explain very little of the vertical changes in phytoplankton abundance. Similarly, results from Chapter 3 demonstrated that certain biological variables when considered alone, particularly particle size spectra and the distribution of other particle types, poorly predicted phytoplankton features. These conclusions suggest that the dynamics controlling small-scale vertical phytoplankton distributions involve a complex interplay of many different variables. In Chapter 4, I developed a model that determined the maximum strength of vertical phytoplankton gradients through a balance of biological and physical factors. This work, coupled with previous models of phytoplankton layer formation, provides a more complete mechanistic understanding of small-scale phytoplankton patchiness (Stacey et al. 2007; Birch et al. 2008; Birch et al. 2009).

Despite the different focus of each of my thesis chapters, all of my conclusions emphasize the importance of measuring the composition of the phytoplankton community

and how it changes with depth. Chapters 2 and 3 document one way that the phytoplankton can vary vertically – by size, and other studies have demonstrated that species composition can also significantly fluctuate (Rines et al. 2002). This vertical structure in the phytoplankton community has important implications for local rates of zooplankton grazing and aggregate formation and sinking, processes which are highly dependent on particle size (Frost 1972; Shanks and Trent 1980; Jackson 1990; McDonnell and Buesseler 2010). Additionally, the results of Chapter 4 show that small-scale changes in the phytoplankton community can strongly influence the strength of phytoplankton gradients that can form, since species composition determines the mechanisms and rates of layer formation. Additionally, knowledge of phytoplankton community composition is essential to understanding the effects of spatial scale on observed microscale phytoplankton patterns. Only with this knowledge can one accurately interpret distributions of phytoplankton at scales of a centimeter and less (Chapter 5).

This thesis provides insight into many aspects of small-scale phytoplankton distributions. However, it has also revealed many issues that are still poorly understood. Although we have now characterized small-scale phytoplankton variability in many cases, a larger effort needs to be made to quantify local changes in the phytoplankton community, both by species and size composition. With advances in both field sampling devices and imaging instruments, in situ measurement of the phytoplankton community on these scales is becoming a reality. Since the work presented here was constrained to analyzing the distributions of only the largest phytoplankton and fluorescent particles, improved technology will also be important to more highly resolve individual

phytoplankton, allowing visualization of even the smallest phytoplankton. In addition, models of phytoplankton layer formation including the one presented here (Chapter 4) suggest that both physical and biological rates interact to control phytoplankton structure. Thus, there is a continued need for multidisciplinary sampling programs to obtain simultaneous high-resolution physical and biological measurements. Improved techniques in measuring phytoplankton growth rates, motility, and zooplankton grazing rates will be important for parameterizing current models and interpreting their predictions. Finally, phytoplankton distributions on centimeter scales are still mostly unknown, largely due to logistical constraints associated with sampling at these smaller scales. This dissertation emphasizes that to quantify microscale phytoplankton distributions, it is necessary to measure the distribution and properties of individuals. With these future steps, we will be able to link small-scale changes in phytoplankton distributions with large-scale processes that drive marine ecosystems.

References

Birch, D. A., W. R. Young, and P. J. S. Franks. 2008. Thin layers of plankton: Formation by shear and death by diffusion. Deep-Sea Research Part I **55**: 277-295.

Birch, D. A., W. R. Young, and P. J. S. Franks. 2009. Plankton layer profiles as determined by shearing, sinking and swimming. Limnology and Oceanography **54:** 397-399.

Cowles, T. J., R. A. Desiderio, and M. Carr. 1998. Small-scale planktonic structure: persistence and trophic consequences. Oceanography **11**:4-9.

Dekshenieks, M. M., P. L. Donaghay, J. M. Sullivan, J. E. B. Rines, T. R. Osborn, and M. S. Twardowski. 2001. Temporal and spatial occurrence of thin phytoplankton layers in relation to physical processes. Marine Ecology Progress Series **223**: 61-71.

Desiderio, R. A., T. J. Cowles, and J. N. Moum. 1993. Microstructure profiles of laser-induced chlorophyll fluorescence spectra: evaluation of backscatter and forward-scatter fiber-optic sensors. Journal of Atmospheric and Oceanic Technology **10**: 209-224.

Doubell, M. J., L. Seuront, J. R. Seymour, N. L Patten, and J. G. Mitchell. 2006. High-resolution fluorometer for mapping microscale phytoplankton distributions. Applied and Environmental Microbiology **72**: 4475-4478.

Doubell, M. J., H. Yamazaki, H. Li, and Y. Kokubu. 2009. An advanced laser-based fluorescence microstructure profiler (TurboMAP-L) for measuring bio-physical coupling in aquatic systems. Journal of Plankton Research, doi: 10.1093/plankt/fbp092

Franks, P. J. S., and J. S. Jaffe. 2008. Microscale variability in the distributions of large fluorescent particles observed *in situ* with a planar laser imaging fluorometer. Journal of Marine Systems **69**: 254-270, doi:10.1016/j.jmarsys.2006.03.027.

Frost, B.W. 1972. Effects of size and concentration of food particles on the feeding behavior of the marine planktonic copepod Calanus pacificus. Limnology and Oceanography. 17 (6): 805-815.

Jackson, G. A. 1990. A model of the formation of marine algal flocs by physical coagulation processes. Deep-Sea Research **37**: 1197-1211.

McManus, M. A., A. L. Alldredge, A. H. Barnard, E. Boss, J. F. Case, T. J. Cowles, P. L. Donaghay, L. B. Eisner, D. J. Gifford, C. F. Greenlaw, C. M. Herren, D. V. Holliday, D. Johnson, S. MacIntyre, D. M. McGehee, T. R. Osborn, M. J. Perry,

R. E. Pieper, J. E. B. Rines, D. C. Smith, J. M. Sullivan, M. K. Talbot, M. S. Twardowski, A. Weidemann, and J. R. Zaneveld. 2003. Characteristics, distribution and persistence of thin layers over a 48 hour period. Marine Ecology Progress Series **261**: 1-19.

McDonnell, A. M. P., and K. O. Buesseler. 2010. Variability in the average sinking velocity of marine particles. Limnology and Oceanography **55**: 2085-2096.

Mitchell, J. G. and J. A. Fuhrman. 1989. Centimeter scale vertical heterogeneity in bacteria and chlorophyll *a*. Marine Ecology Progress Series **54** : 141-148.

Rines, J. E. B., P. L. Donaghay, M. M. Dekshenieks, J. M. Sullivan, and M. S. Twardowski. 2002. Thin layers and camouflage: hidden *Pseudo-nitzschia* spp. (Bacillariophyceae) populations in a fjord in the San Juan Islands, Washington, USA. Marine Ecology Progress Series **225**: 123-137.

Ryan, J. P., M. A. McManus, J. D. Paduan, and F. P. Chavez. 2008. Phytoplankton thin layers caused by shear in frontal zones of a coastal upwelling system. Marine Ecology Progress Series **354**: 21-34.

Shanks, A. L., and J. D. Trent. 1980. Marine snow: sinking rates and potential role in vertical flux. Deep-Sea Research **27A**: 137-143.

Stacey, M. T., M. A. McManus, and J. V. Steinbuck. 2007. Convergences and divergences and thin layer formation and maintenance. Limnology and Oceanography **52**: 1523-1532.

Steinbuck, J. V., M. T. Stacey, M. A. McManus, O. M. Cheriton, and J. P. Ryan. 2009. Observations of turbulent mixing in a phytoplankton thin layer: Implications for formation, maintenance, and breakdown. Limnology and Oceanography **54**: 1353-1368.

Waters, R. L., J. G. Mitchell, and J. Seymour. 2003. Geostatistical characterisation of centimetre-scale spatial structure of *in vivo* fluorescence. Marine Ecology Progress Series **251**: 49-58.

Wolk, F., H. Yamazaki, L. Seuront, and R. G. Lueck. 2002. A new free-fall profiler for measuring biophysical microstructure. Journal of Atmospheric and Oceanic Technology **19**: 780-793.

Yamazaki, H., J. G. Mitchell, L. Seuront, F. Wolk, and H. Li. 2006. Phytoplankton microstructure in fully developed oceanic turbulence. Geophysical Research Letters **33**: L01603, doi:10.1029/2005GL024103.